AN ALFVÉN WAVE APPROACH TO MAGNETOSPHERIC FIELD-ALIGNED CURRENTS

by

DENIS HAYWARD

Thesis submitted for the degree of
Doctor of Philosophy of the University
of London

The Blackett Laboratory
Imperial College of Science and Technology
LONDON SW7 2BZ

July 1981

ABSTRACT

An explanation is put forward in terms of Alfvén waves to account for the observations of magnetic field-aligned currents which are seen to be flowing along field lines which map from the auroral zone, via the boundary of the plasma sheet, to the neutral line in the distant magnetotail.

The assumption is made that there exists a process within the neutral sheet which generates a strong electric field across a thin layer. The effect of this field should propagate earthwards as a shear-mode Alfvén wave, which in the steady state should be stationary relative to the earth.

In this situation field lines, with cold polar wind plasma on them, $\underset{\sim}{E} \wedge \underset{\sim}{B}$ drift through the wave. The problem is therefore amenable to an initial formulation in terms of cold plasma theory, and a further development of linear theory by computation.

Following a discussion of the various wave modes which can exist in a cold plasma, linear theory is used to obtain the dispersion relation and expressions for the growth rate. The growth rate is found to be a critical function of the angle between the wave normal and the magnetic field. This fact is demonstrated in plots of the y-component of the magnetic field, and the non-linear behaviour of these diagrams are explained in terms of constant current.

It was found necessary to derive approximations in order to compute the pure Alfvén mode, and these are discussed fully in Chapter 4 where they are shown to be essential in order to suppress

rapid oscillations which are present.

Finally an exploratory search is made of the high resolution ISEE 1 and 2 magnetometer data for representative plasma sheet crossings which occurred in the first half of 1978. Comparison is made between the results of the computation and these selected plots, and in the final chapter conclusions are drawn and suggestions for further work made.

ACKNOWLEDGEMENTS

I should like to thank principally my supervisor, Professor J.W. Dungey, to whom I owe a debt for his patience and constant accessibility. His willingness to offer advice and encouragement ensured that at no time did the work become a chore.

I should also like to thank Drs Southwood, Cowley and Mier-Jedrzejowicz for many hours of stimulating and useful discussion. A separate thank you must also go to Dr Colette Robertson, also of the Magnetospheric Theory Group, and to Nigel Wootton, both of whom also provided many hours of conversation of a less academic but no less stimulating nature.

Finally, Miss Ainslee Rutledge deserves a special mention for unscrambling my writing and succeeding in typing this thesis, a difficult task when equations are present in large numbers.

I also with to thank the Science Research Council for providing financial support throughout the course of this work.

CONTENTS

CHAPTER 1

FIELD ALIGNED CURRENTS AND THE EARTH'S MAGNETOSPHERE

1.1 Introductory Remarks

Since the late 1950's, spacecraft of varying degrees of sophistication have been launched into Earth orbit in order to study the interplanetary environment and its relationship with the Earth. Spacecraft have been launched with the purpose of studying the solar wind, auroral zone and magnetosphere-ionosphere interactions, as well as the deep space probes such as Voyager; and, during the past two decades, magnetospheric physics has undergone a successful period of discovery and exploration. A morphological description of the magnetic field and its time variations has been obtained as well as a knowledge of the particle populations imbedded within. Many of the physical processes at work have been identified and a fairly good quantitative understanding of the radiation belts has been obtained. However, there is still much to understand about the precise roles played by various turbulent processes and their relationship to such phenomena as anomalous resistivity and parallel electric fields; and also about the large, and small scale, field aligned currents which flow into and out of the auroral zone, as these are crucial in the coupling of the magnetosphere and ionosphere. Progress in understanding the physical processes at work is therefore

achieved at the expense of added complexity, as each spacecraft poses many more questions than it provide's answers for. A magnetosphere arises from the interaction of a continuously streaming, hot, collisionless plasma with a magnetised body, in this interaction a cavity is formed in the flow by the magnetic field of the central body; and it is this, the magnetospheric cavity, which was first discussed by Chapman and Ferraro (1931).

This magnetic field also physically ties the points of the magnetosphere together, guiding charged particles, plasma waves and electric currents; trapping thermal plasma and energetic particles; and transmitting hydromagnetic stresses between the exterior flow and the central body.

In the Chapman-Ferraro theory the solar plasma was assumed to be diamagnetic, thus the Earth's field was thought to be confined completely within the cavity. The assumption of a diamagnetic solar wind was first criticised by Alfvén (1939, 1950), however it was Dungey (1961) who first put forward the concept of the "open model", whereby geomagnetic field lines from the polar regions are merged with the interplanetary magnetic field (IMF); and the merged field lines are then referred to as open. In the situation where the IMF field vector is directed southward, a magnetic neutral line is formed which surrounds the magnetosphere, a plane consisting of field lines which cross the neutral line can therefore be imagined, and the intersection of this plane with the ionosphere coincides with the location of the auroral oval, as discovered by Feldstein (1963). This oval is then the projection along the geomagnetic field lines of the neutral line, and it is within this region where the various coupling processes which link the ionosphere and magnetosphere (such as field-aligned currents) show themselves in the form of auroral

displays. An important aspect of the open model is that it allows the solar wind to blow across open field lines, thereby providing the electromotive force, and power for a wide range of magnetospheric phenomena; it is this magnetohydrodynamic (MHD) dynamo which is responsible for converting the kinetic energy of the solar wind into electrical energy (Akasofu and Chapman, 1972); and auroral displays are often described in terms of electrical discharge phenomena which is powered by the solar wind - magnetospheric dynamo.

In support of this it was Zmuda and Armstrong (1974) who first showed that there is an inflow of electric current to the poleward half of the auroral oval in the morning sector, and an outflow from the poleward half during the evening sector. The presence of field aligned currents is vital for the formation of the auroral forms seen in the poleward section of the auroral oval, and the aurora can be divided into essentially two categories :

a) The diffuse aurora - which is largely due to pitch angle diffusion, and

b) The discrete auroral arcs - which are associated with different particle populations than the diffuse aurora, and are also associated with intense field-aligned currents.

Spectrograms obtained from rockets which have been flown through auroral forms identify two principal types of particle precipitation :

c) The high latitude region - this corresponds to the location of the discrete arcs - and has field lines which map to the boundary of the plasma sheet (BPS) : and it is this region which is of special importance in this work. And

d) An area which lies equatorward of the BPS region, and consists of an almost uniform area of precipitation. Field lines here map to the central plasma sheet (CPS); and for the aurora, the difference between BPS and CPS corresponds really to electrons of different energies and pitch angle distributions; pitch angles peaking near 0^{o} for the BPS particles and 90^{o} for the CPS populations.

In concluding this introductory section, which has tried to stress those parts of the magnetosphere which are especially relevant to this work it is perhaps best to summarise by giving a diagram which displays most of the points discussed above, and Fig. 1.1 shows a section through the noon-midnight meridian, which may serve as a reference.

1.2 Field-Aligned Currents

In fairly recent times it has become generally accepted that magnetospheric field-aligned currents provide a mechanism by which the aurora can be produced, however there is still confusion over the precise roles played by phenomena such as anomalous resistivity, double layers and electrostatic shocks (Swift, 1976; Hudson and Mozer, 1978A; Hudson and Mozer, 1978B; Kindel and Kennel, 1971).

The evidence which has brought about this recognition has been largely due to particle and field observations acquired during the last decade from a variety of rocket and satellite experiments. These have not only confirmed the presence of large scale field aligned currents, but have also shown them to be an important and permanent feature of the system coupling the magnetosphere and ionosphere (Arnoldy, 1974; Anderson and Vondrak, 1975; Potemra and Saflekos, 1978; Fairfield, 1973; Frank et al, 1980). The direction in which

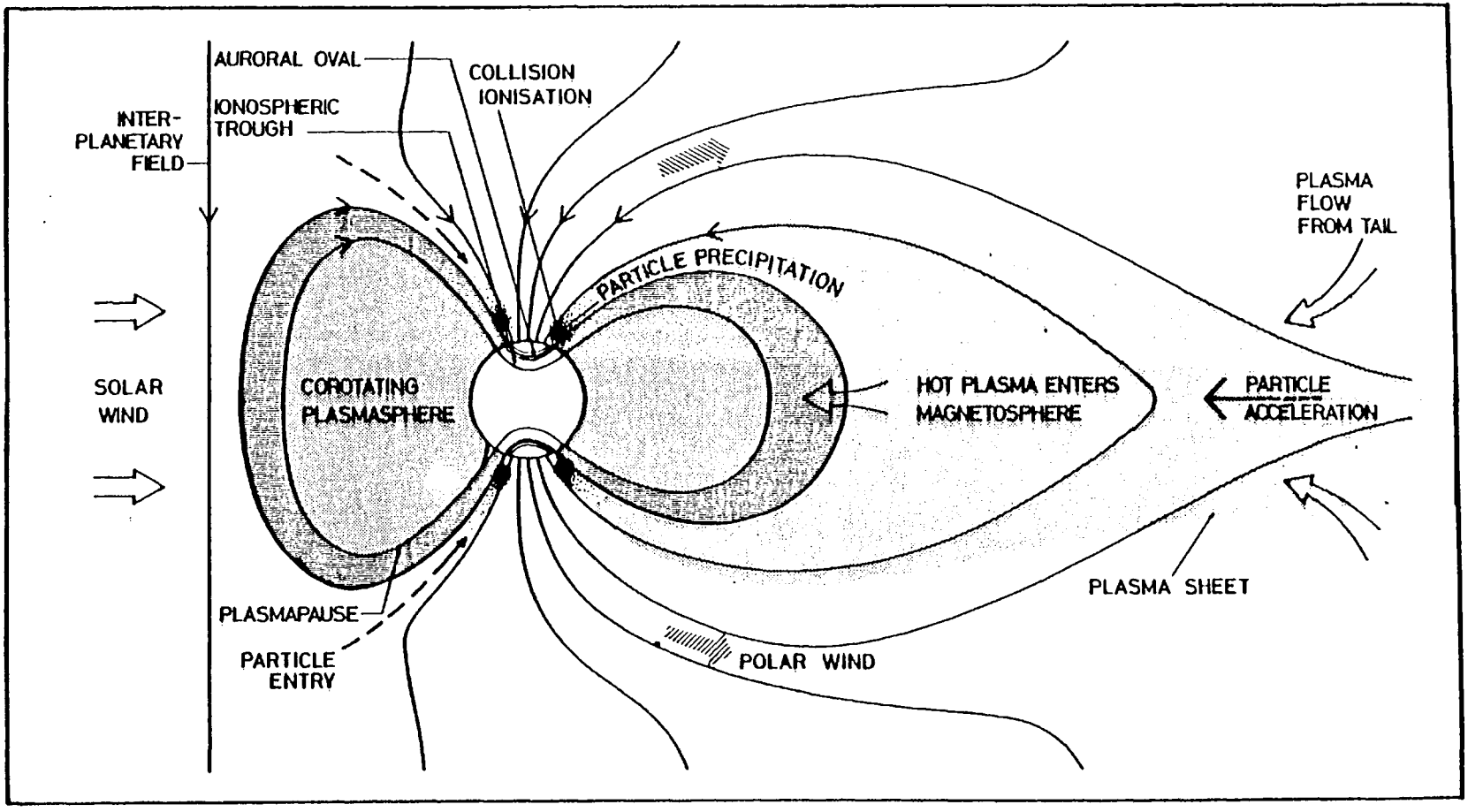

Figure 1.1 Noon-midnight section of the Earth's Magnetosphere

the large scale field-aligned currents (FAC) flow is summarised in Fig. 1.2. These diagrams were constructed from (a) data obtained from 439 passes of the TRIAD spacecraft during weekly disturbed conditions ($|AL| < 100\gamma$) and (b) data obtained from 366 triad passes during active periods ($|AL| \geq 100\gamma$), and show the "Region 1" (poleward side) and "Region 2" (equatorward side), current systems, (Zmuda and Armstrong, 1974; Iijima and Potemra, 1976a,b).

In addition to the macroscopic currents represented by Fig. 1.2 the first report of thin current layers in the aurora was made by Cloutier et al (1970), who were the first to associate the currents in thin sheets with individual auroral arcs, and in 1975 the first reports of similar layers on the plasma sheet boundary were made by Thomas and Hedgecock (1975). It seemed clear therefore, that an understanding of plasma sheet boundary dynamics and current flow in thin layers would be essential for an understanding of individual arc-forming processes.

In order to estimate the size of these field-aligned currents it is necessary to work from the observed magnetic perturbations and the magnitude and direction of the equivalent FAC's can be calculated from the observed transverse magnetic perturbations ($\Delta\underset{\sim}{B}$) by an application of Maxwell's equations, viz.

$$\underset{\sim}{j} = \frac{1}{\mu_o} (\nabla \Lambda (\Delta\underset{\sim}{B})) \qquad 1.1$$

(Zmuda and Armstrong, 1974).

Magnetic disturbances observed with polar orbiting spacecraft are often seen to occur in the geomagnetic east-west direction, and in this case the current density is given by :

$$j_{\shortparallel} = \frac{1}{\mu_o} \frac{\partial}{\partial x} (\Delta B_y) \qquad 1.2$$

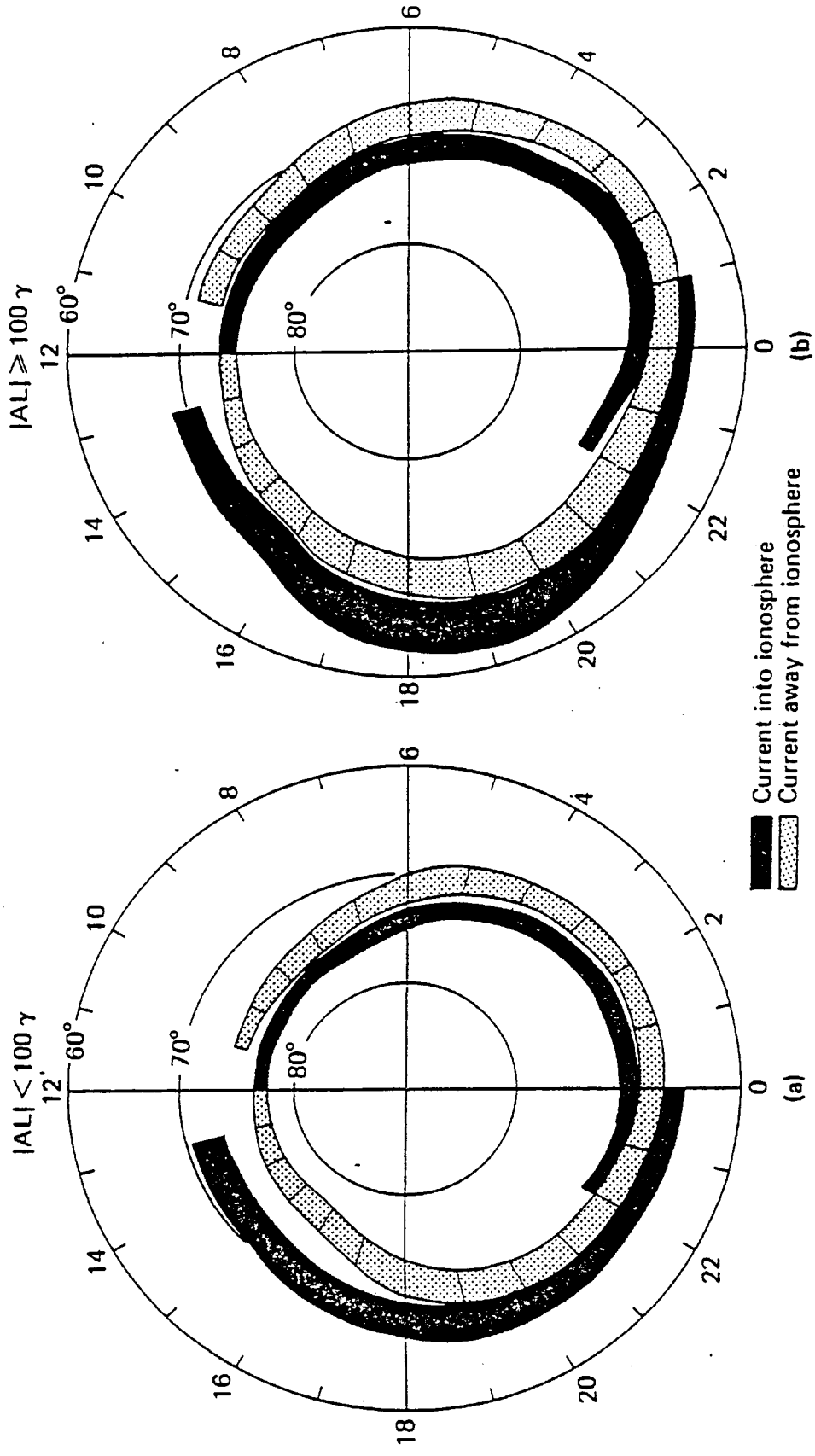

Figure 1.2 Macroscopic Field-aligned current systems (after Potemra, 1976a,b)

where "$_{\shortparallel}$" refers to the field-aligned flow. In equation 1.2 x is positive in the northward direction, $j_{\shortparallel}$ downwards and ΔB_y in the eastward direction. Under these circumstances the magnitude of the current density, $\int j_{\shortparallel}\, dx$, is given directly by the amplitude of the magnetic perturbation, i.e.

$$\int j_{\shortparallel}\, dx = \left(\frac{1}{\mu_o}\right) \Delta B_y \qquad 1.3$$

Thus for example, a 100γ perturbation would correspond to a current intensity of about 0.087 Am^{-1}.

Field-aligned current determined for example from TRIAD magnetometer data have been positively correlated with observations of visual aurora acquired with ground based all-sky cameras (Kamide and Akasofu, 1976), with the DMSP satellite (Kamide and Rostocker, 1977), and with the ISIS 2 satellite (Kamide et al, 1978). It has been shown that in the evening sector, the discrete auroral arcs are in general confined within the region of upward flowing FAC; and it is in this region where intense electron precipitation is seen along with the "inverted V" events, and associated ion-cyclotron turbulence (Mozer et al, 1980); it is also this region which has magnetic field lines which map, via the boundary of the plasma sheet, to the neutral line in the distant magnetotail and upon which extensive noise has been reported at both low altitude and in the distant tail (Gurnett and Frank, 1977; Gurnett, Frank and Lepping, 1976).

Conversely, the diffuse aurora occupies the region which is equatorward of the discrete, and it is contained within the "Region 2" current system of downward flowing FAC's; and it has already been mentioned that the essential difference as far as the auroral particle populations are concerned is that those causing the discrete

aurora are believed to originate from the BPS region, and those causing the diffuse from the CPS (see section 1.1).

For the purposes of this work we are primarily concerned with the region which maps to the boundary of the plasma sheet, i.e. the region containing the discrete auroral arcs; this part of the magnetosphere-ionosphere system is crucial in the understanding of phenomena such as substorm dynamics, turbulence levels and the causal relationships between turbulence and electrostatic shocks, double layers and anomalous resistivity (see Mozer et al, 1980; Southwood, 1978; Hudson and Mozer, 1978a,b) and it is important to realise that field-aligned currents are the common denominator between discrete arcs and the plasma sheet boundary. For present purposes it is useful to have a definition of the plasma sheet, other than the qualitative one inferred from Fig. 1.1, and the one given by Dungey (1975) is suitable, in that the plasma sheet may be defined "by a population of electrons and protons whose pressure is comparable to the magnetic pressure, and whose characteristic energy is of the same order as that of auroral primaries, viz. a few keV".

It is also necessary to say, briefly at this stage, something about the spatial scales which are involved in that the scales of the region 1 current systems are very much larger than those associated with the discrete arcs which are imbedded in them; arcs themselves are associated with spatial scales which are measured in tens of km, rather than the hundreds associated with the region 1 macroscopic current system. The arcs may therefore be thought of as fine structure within the large scale region 1 system, existing as they do on field lines which map to the plasma sheet boundary : it is this latter system that is of particular interest here.

Finally, in concluding this section, mention should be made of

the importance of boundaries within the magnetosphere, for example the magnetopause, the importance of which has been realised for about 20 years, particularly in connection with the generation, via the Kelvin-Helmholtz instability, of certain types of geomagnetic pulsation (Southwood, 1974; Chen and Hasegawa, 1974).

However, the plasma sheet boundary, first reported by Bame et al (1967), has only been seen to be of importance, particularly in connection with the auroral sybstorm, for about 10 years (Meng and Anderson, 1971; Akasofu et al, 1971; Möbius et al, 1980). The boundary, which has a sharp density gradient across it, is typically about 1 R_e thick (Andrews et al, 1980), and marks the transition from magnetotail lobe plasma in which the plasma $\beta << 1$, and particle densities are of the order 10^{-1} cm^{-3}, and the plasma sheet itself in which $\beta \approx 1$, and the number density at least an order of magnitude greater.

It is in the outer layer of this boundary in which this work is based, as it is field lines in this region which would support current-carrying shear mode Alfvén waves as they propagate Earthwards from the tail neutral line.

1.3 Preliminaries and Initial Formulation

The purpose of this work is therefore to offer an Alfvén wave explanation which will be able to account for the observations of field-aligned currents which flow along field lines mapping from the tail neutral line to the auroral ionosphere. However, before the problem can be formulated the assumed existence of these waves in this region of the magnetosphere should be justified.

For the purposes of this model it is assumed that within the neutral sheet there exists some process which generates a strong electric field across a thin layer, and it turns out that justifying the existence of the shear-mode wave is equivalent to justifying the

existence of the above electric field. Alfvén (1968), following on from work done by Speiser (1965) on the orbits of particles in neutral sheets, was the first to discuss a model which, like the magnetotail, is finite in the y-direction; and while this model has the virtue of giving a value for the cross tail potential it is based on an approximation which neglects all current due to particles from the magnetosheath, at the flanks of the tail, entering the neutral sheet. Using this model Alfvén predicted that all the protons would drift to the dusk side, and all the electrons to the dawn, and that far enough away from the neutral sheet the fields given by B_x and E_y are uniform therefore all particles drift towards the neutral sheet with a speed given by $\frac{E_y}{B_x}$. However, Cowley (1971) pointed out that although protons and electrons drift towards the neutral sheet at the same speed, once in the sheet the protons, because of their greater mass, are accelerated more slowly than the electrons and therefore spend longer in the neutral sheet. This would then result in a space charge being set up, and Alfvén's assumption of uniform electric fields would not therefore be self-consistent.

Cowley therefore generalised the model by allowing for any electrostatic field and solved for the self-consistent potential, showing that all the equipotentials go almost to the dusk edge of the sheet (as shown in Fig. 1.3), and on either side of the sheet all charged particles drift approximately along the equipotentials. He found also that the region where the potential varies rapidly close to the dusk edge of the sheet was of the order of the proton wavelength, which may be taken as $\lambda_p = \frac{227.7}{(n)^{\frac{1}{2}}}$ and if the number density n, is in units of "cm^{-3}" then λ_p is in kilometres.

In this model electrons approach very close to the dusk edge of the sheet before encountering the centre plane at z = 0, after which

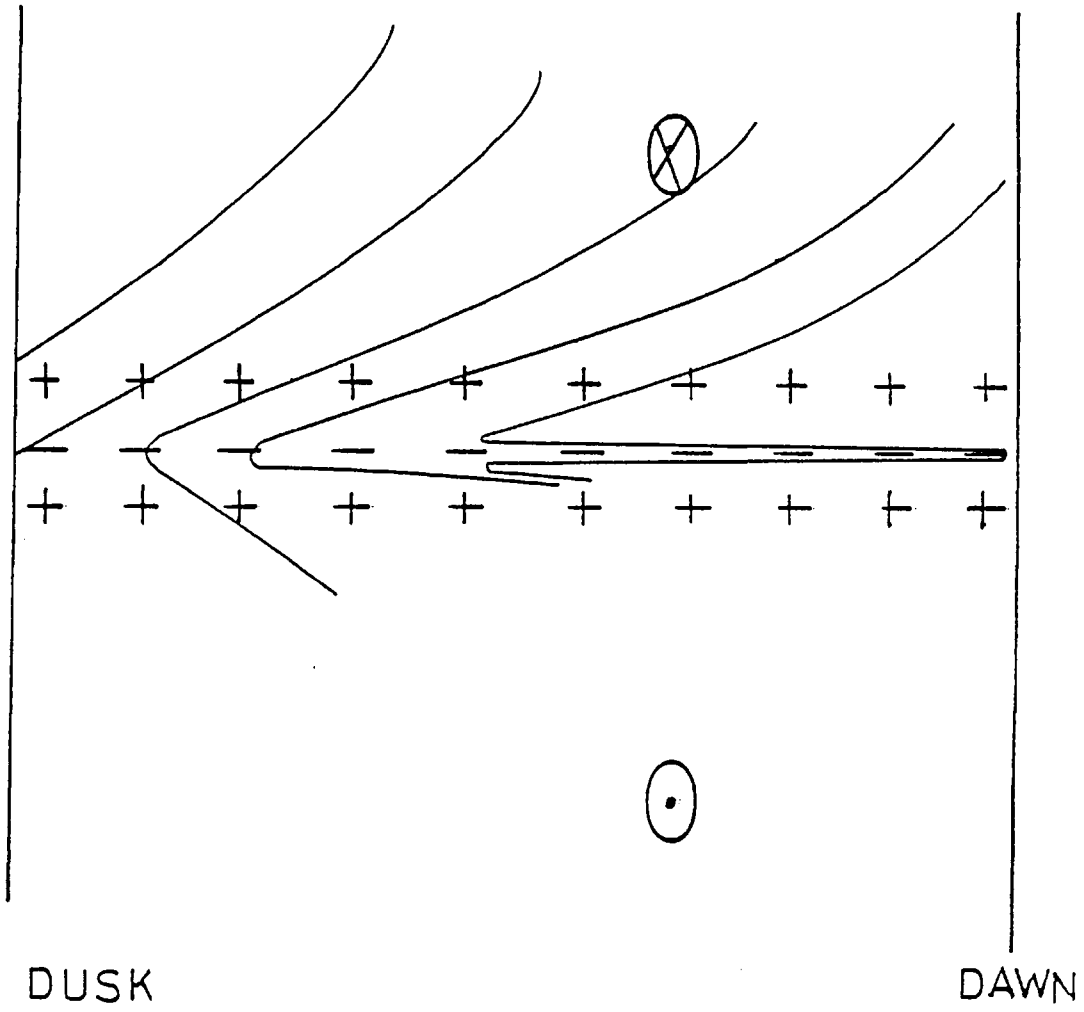

Figure 1.3 The Alfvén-Dungey-Cowley model, showing electron layer at centre plane

they move towards dawn in a layer which is much thinner than the layer of positive charge. This electron layer is therefore a thin layer of negative charge and the potential in the centreplane at z = 0 should be between the dawn and dusk side values.

It can therefore be seen from Fig. 1.3 that a large positive space charge exists which has the effect of setting up a local polarization electric field which is at right-angles to the current sheet. With this in mind the following scenario for generation of the shear mode waves can be put forward.

Following the consequences which result from the merging of terrestrial field lines with the IMF, the open field lines are then blown over the polar cap by the solar wind and it is these field lines, which contain cold polar wind plasma, that proceed to $\underset{\sim}{E} \Lambda \underset{\sim}{B}$ drift towards the centre plane of the magnetotail at speeds of 10-15 km s^{-1}. As these field lines approach the region of polarisation field close to z = 0, they follow the equipotentials, or flow streamlines in this case, and it is evident from Fig. 1.3 that near the point of field line reconnection they undergo a two and fro motion. However, the presence within the sheet of the dawnward flowing electron beam ensures that a potential difference exists between the middle and the outside of the sheet, and it is the effect of this electric field which should propagate Earthward as a shear mode Alfvén wave; the voltage due to the perpendicular field $\underset{\sim}{E}_z$ is then fed along the field lines to a thin layer in the auroral ionosphere thereby driving currents, the magnitude of which is determined by the amount of resistance in the circuit, in this case the ionosphere is the main load plus any anomalous resistance which might be present on the field lines.

In the steady state this wave should be stationary relative to the earth, and the flux tubes which are then $\underset{\sim}{E} \Lambda \underset{\sim}{B}$ drifting equatorwards

through the wavefront ensure that the reflected wave returns to a point which is Earthward, by several tens of Earth radii, from its point of origin. This is summarised schematically by Fig. 3.1, in which the source region is represented by a battery, and the wave is shown to be returned at a substantial Earthward distance from its source.

It is useful at this point to estimate orders of magnitude for some of the plasma parameters which are of importance to the model, for example the Alfvén Mach number M_A, and the Alfvén speed V_A, and while the magnitude of V_A, which is the characteristic speed for the propagation of low frequency waves, is given strictly by :

$$V_A = \frac{B}{[4\pi n(m_p+m_e)]}$$

numerically we may use the following equation :

$$V_A \approx 22 \times \frac{B}{(n)^{\frac{1}{2}}}$$

where $\underset{\sim}{B}$ is in nT(γ) and n in cm^{-3}, then V_A will be in km s^{-1}.

For the purposes of this work we are interested in distances down tail of perhaps 20 R_e, and for a position just outside the plasma sheet, i.e. in the lobe plasma, we may take $\underset{\sim}{B} \approx 15\gamma$ and $n \approx 0.1$ cm^{-3} hence, $V_A \approx 10^3$ km s^{-1}. Now the wave frame is such that the wave normal, and therefore the x-axis, is pointing almost into the $\underset{\sim}{E} \wedge \underset{\sim}{B}$ flow (see Chapter 3, section 3.2, Fig. 3.2). Thus for an Alfvén mach number defined with respect to the wave normal, and an $\underset{\sim}{E} \wedge \underset{\sim}{B}$ drift speed of about 10 km s^{-1} the value of M_A is given by

$$M_A = \frac{10}{10^3} = 10^{-2}$$

Now in Chapter 3, equation 3.46 , an expression is given for the growth rate which has the following form :

$$\frac{\sigma^2}{\Omega_p^2} = \frac{M_A^2 - \cos^2\theta}{2\cos^2\theta + 1/1800}$$

we therefore see the result, well known from cold plasma theory, that $\cos\theta < M_A$: where θ here is the angle between the wave normal and the magnetic field line.

The wave therefore, has a large field-aligned component of current and with its wavefront nearly parallel to the local magnetic field it is able to stand in the very low Mach number flow.

1.4 Some Wave Characteristics

Plasma waves which are propagating at an oblique angle to the magnetic field are inherently more difficult to analyse than either the parallel or perpendicular case primarily because of the greater variety of linear modes which can exist and also because the modes are coupled. Figure 1.4 is a schematic plot of ω v k for oblique waves in a plasma : lines with slopes equal to the Alfvén and sound speeds are shown as dotted, and intersection of a dispersion curve with a line of slope equal to the shock speed V_1, determines the frequency and wavelength (ω and k) of the possible solutions. It can be seen that for high Mach number shocks there are no points of intersection, and therefore no oscillatory solutions, whereas for lower Mach numbers there are at least two solutions possible.

In Chapter 3 the dispersion relation for waves propagating at an angle θ to the magnetic field is derived and this has the following familiar form :

$$\left(\frac{w}{V_A}\right)^2 = 1 - \tfrac{1}{2}\sin^2\theta \pm \left\{\tfrac{1}{4}\sin^4\theta + \left(\frac{\omega}{\Omega_p}\right)^2\cos^2\theta\right\}^{\frac{1}{2}} - \frac{\omega^2}{\Omega_e\Omega_p}$$

where $w = \omega/k$ = phase velocity, and the other symbols are defined in Chapter 3 and in the symbol's table. However, it can be seen that

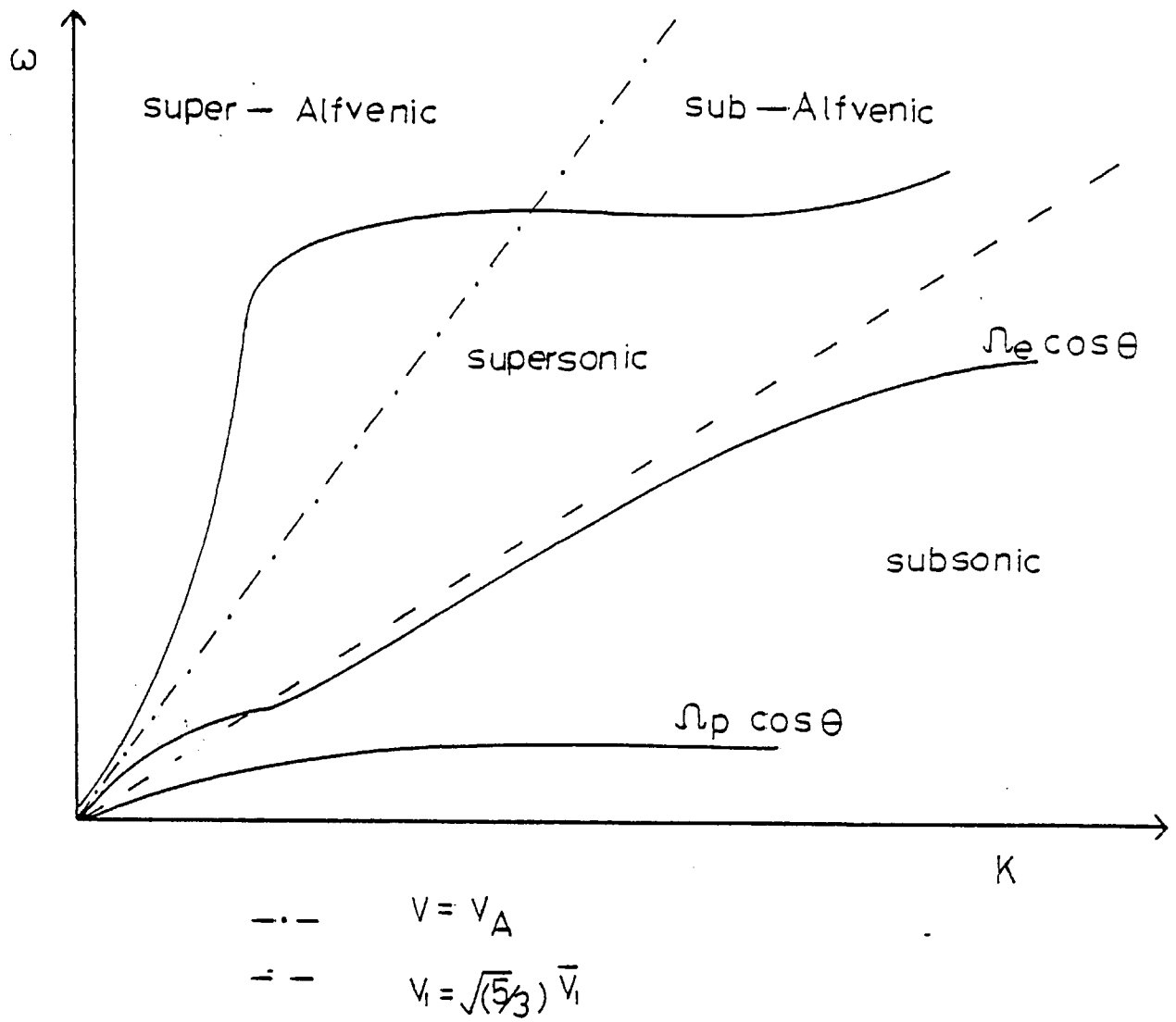

Figure 1.4 Schematic plot of ω against k for oblique waves in a plasma.

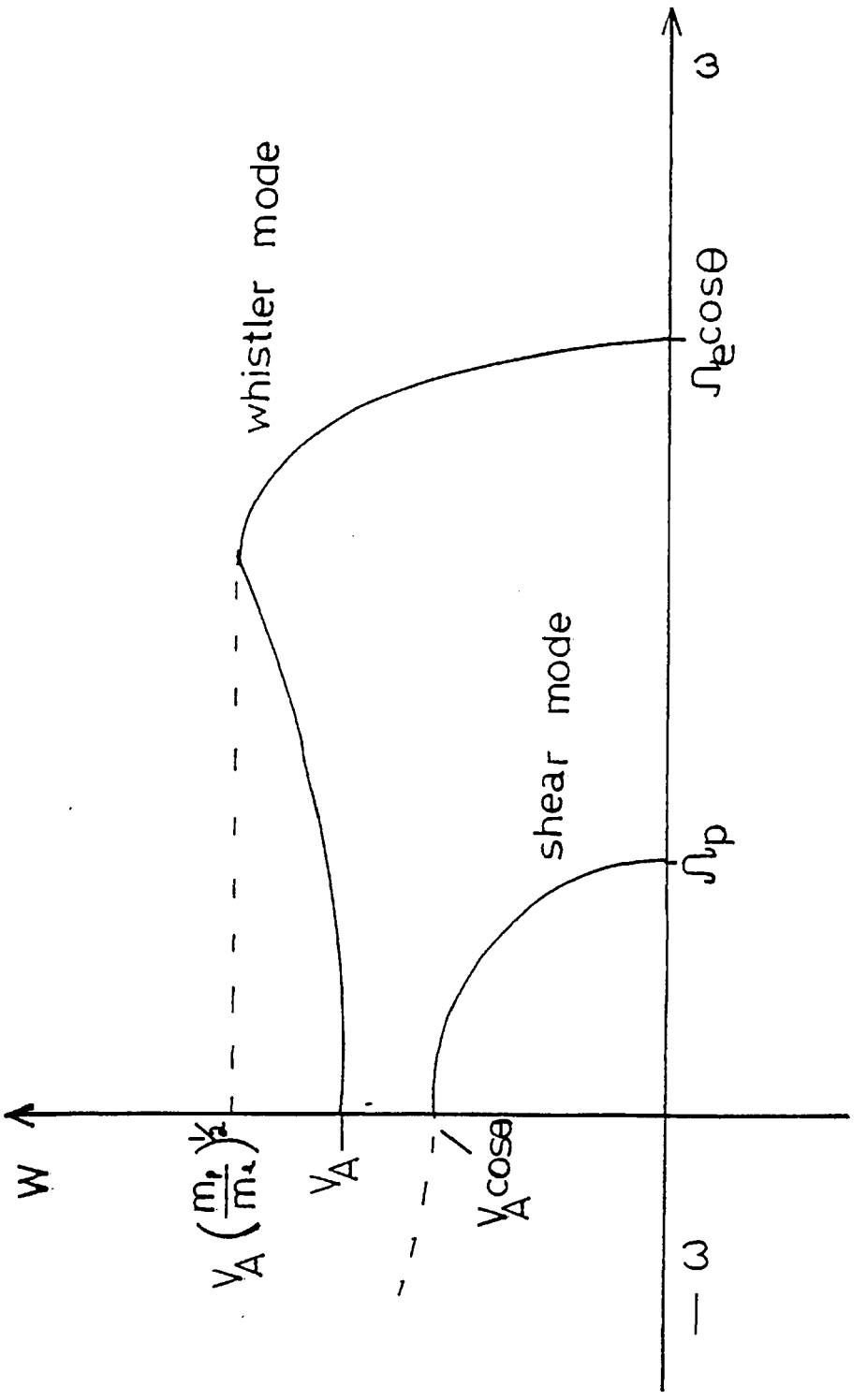

Figure 1.5 Dispersion plot for real ω, to show the modes for each sign.

there are two possible solutions depending on whether the positive or negative sign is being considered, and physically this corresponds to choosing either the whistler or shear mode respectively. This separation is shown more clearly by plotting w against ω - and this is done in Fig. 1.5 where the difference between the two modes is apparent.

The shear mode wave is therefore characterised by an angular frequency ω which is less than the proton gyrofrequency Ω_p, and in fact a mode transition occurs for $\omega = \Omega_p$.

1.5 Summary

The four sections of this chapter have tried to put into perspective the environment within the magnetosphere in which most of this work is based. The first section charts the progress made in magnetospheric physics since the beginning of the space era. The second section attempts to show the relationship between the auroral phenomena and processes at work in the plasma sheet by discussing the field-aligned currents which are common to both regions. In the final two sections the problem is formulated in a qualitative way and the assumptions of a polarisation field perpendicular to the sheet is justified; and finally concludes with a brief discussion of the dispersion relation. The final sections indicate that the procedure to be followed is to investigate numerically the cold plasma equations for shock-like solutions in this particular wave mode and for this low value of the Alfvén Mach number.

In Chapter 2 it is shown how the various modes arise which can exist in a cold collisionless plasma, and this serves to define properties and terms which recur throughout. In Chapter 3 the problem is formulated in a quantitative fashion and a linear analysis of

the equations is done along with the derivation of the dispersion relation.

The fourth chapter deals with the process of computing the equations, starting by showing quantitatively that shock solutions exist for $M_A < 1$, and discusses the approximations which are required in order to compute the Alfvén mode. In Chapter 5 results of the computations are given and discussed in the light of magnetometer data from the ISEE 1 and 2 spacecraft, and a short discussion on what each should see upon traversing the plasma sheet is made.

The final chapter draws conclusions on the previous five, summarises, and makes suggestions for further work.

CHAPTER 2

A FORMULATION OF HYDROMAGNETICS

2.1 Introduction

Under certain conditions, oscillatory processes in a quiescent plasma can be suitably described by making use of an equation which involves a self-consistent field without a collision term, coupled with the Maxwell equations which describe the electromagnetic field.

For this description to be valid it is necessary that the quantity $\omega\tau >> 1$, where ω is the frequency of the oscillation and τ the relaxation time.

However, when $\omega\tau << 1$ higher order correlation effects must be considered beginning with the collision integral. In principle therefore, progress can be made by using the kinetic equation with a self-consistent field and a collision integral together with Maxwell's equations; but, this method can rapidly become very complicated and is in fact unnecessary because for $\omega\tau << 1$ the more compact hydromagnetic description is valid.

The full equations of hydromagnetics (HM) can be written in the following form :

$$\frac{\partial \rho}{\partial t} + \nabla.(\rho u) = 0 \qquad 2.1.$$

$$\rho \frac{d\underset{\sim}{u}}{dt} = -\nabla P + \nabla\Lambda(\underset{\sim}{B}\Lambda\underset{\sim}{B}) \qquad 2.2.$$

$$\nabla \Lambda \underset{\sim}{E} = - \frac{\partial \underset{\sim}{B}}{\partial t} \qquad 2.3.$$

$$\nabla \Lambda \underset{\sim}{B} = \mu_o j \qquad 2.4.$$

$$\nabla . \underset{\sim}{B} = 0 \qquad 2.5.$$

$$\frac{ds}{dt} = 0 \qquad 2.6.$$

In equations 2.1 through 2.6 $\underset{\sim}{B}$ is the magnetic field, $\underset{\sim}{E}$ is the electric field, ρ the density, u the macroscopic velocity and s the entropy.

Equation 2.6 is necessary in order to be able to apply the HM description, as it expresses the assumption that macroscopic processes proceed slowly, and also that dissipation is absent : in other words it expresses the adiabaticity of the process.

2.2 Determination of the Hydromagnetic modes

The process of determining which wave modes and oscillations can be excited, and which can propagate through the plasma will just involve equations 2.1 through 2.6, assuming no energy dissipation.

In the case of one dimensional waves propagating along the z-axis, with all HM quantities functions only of z and t, the equations take the form :

$$\frac{\partial \rho}{\partial t} + u_z \frac{\partial \rho}{\partial z} + \rho \frac{\partial u_z}{\partial z} = 0$$

$$\frac{\partial s}{\partial t} + u_z \frac{\partial s}{\partial z} = 0$$

$$\frac{\partial u_x}{\partial t} + u_z \frac{\partial u_x}{\partial z} - \frac{B_z}{\rho} \frac{\partial B_x}{\partial z} = 0$$

$$\frac{\partial u_y}{\partial t} + u_z \frac{\partial u_y}{\partial z} - \frac{B_z}{\rho} \frac{\partial B_y}{\partial z} = 0$$

$$\frac{\partial u_z}{\partial t} + \frac{P}{\rho}\frac{\partial \rho}{\partial z} + \frac{P}{\rho}\frac{\partial s}{\partial z} + u_z \frac{\partial u_z}{\partial z} + \frac{B_x}{\rho}\frac{\partial B_x}{\partial z} + \frac{B_y}{\rho}\frac{\partial B_y}{\partial z} = 0$$

$$\frac{\partial B_x}{\partial t} - B_z \frac{\partial u_x}{\partial z} + B_x \frac{\partial u_z}{\partial z} + u_z \frac{\partial B_x}{\partial z} = 0$$

$$\frac{\partial B_y}{\partial t} - B_z \frac{\partial u_y}{\partial z} + B_y \frac{\partial u_z}{\partial z} + u_z \frac{\partial B_y}{\partial z} = 0$$

$$\frac{\partial B_z}{\partial t} = \frac{\partial B_z}{\partial z} = 0$$

Where from the last equation, B_z = constant.

Following Bohachevsky (1962), the above set can be written in a more compact form :

$$\frac{\partial a_i}{\partial t} + \sum_{j=1}^{7} Z_{ij}(a) \frac{\partial a_j}{\partial z} = 0 \qquad 2.7.$$

where a_i is the HM state vector and is given by :

$$a_i = \begin{vmatrix} \rho \\ s \\ u_x \\ u_y \\ u_z \\ B_x \\ B_y \end{vmatrix}$$

and the index takes on the values $1 \rightarrow 7$.

So for a 1-D wave there are seven HM variables.

In equation 2.7 Z_{ij} is the matrix given by :

$$Z_{ij} = \begin{vmatrix} u_z & 0 & 0 & 0 & \rho & 0 & 0 \\ 0 & u_z & 0 & 0 & 0 & 0 & 0 \\ 0 & 0 & u_z & 0 & 0 & -B_z/\rho & 0 \\ 0 & 0 & 0 & u_z & 0 & 0 & -B_z/\rho \\ p/\rho & p/\rho & 0 & 0 & u_z & B_x/\rho & B_y/\rho \\ 0 & 0 & -B_z & 0 & B_x & u_z & 0 \\ 0 & 0 & 0 & -B_z & B_y & 0 & u_z \end{vmatrix}$$

Equation 2.7 thus represents the entire HM set of equations in a compact fashion.

To examine each of the seven modes it is useful to assume small amplitude perturbations and then linearize the set represented by equation 2.7.

Therefore, assuming $a_i = a^o_i + a'_i$ where a^o_i is the unperturbed state of the plasma, the linearized form of 2.7 is just

$$\frac{\partial a'_i}{\partial t} + \sum_{i=1}^{7} Z_{ij} (a^o_i) \frac{\partial a'_j}{\partial z} = 0 \qquad 2.8.$$

A technique can now be employed to reduce Z_{ij} to a simpler form.

If a frame is chosen so that it moves with the plasma velocity, then $\underset{\sim}{u}^o = 0$, and by rotating the frame about the z-axis, $B^o_y = 0$. In this case Z_{ij} is now given by :

$$Z_{ij} = \begin{vmatrix} 0 & 0 & 0 & 0 & \rho & 0 & 0 \\ 0 & 0 & 0 & 0 & 0 & 0 & 0 \\ 0 & 0 & 0 & 0 & 0 & -B_z/\rho & 0 \\ 0 & 0 & 0 & 0 & 0 & 0 & -B_z/\rho \\ p/\rho & p/\rho & 0 & 0 & 0 & B_x/\rho & 0 \\ 0 & 0 & -B_z & 0 & B_x & 0 & 0 \\ 0 & 0 & 0 & -B_z & 0 & 0 & 0 \end{vmatrix}$$

With this simplification plane wave solutions to eqn 2.8 can be sought.

Assume $a'_i = A_i \exp i\,(kz - \omega t)$ differentiating and substituting into 2.8 gives

$$\sum_{j=1}^{7} Z_{ij}\, A_j = V\, A_i \qquad 2.9.$$

where $V = \omega/k$ and is just the phase velocity.

Equation 2.9 suggests that the amplitudes of the different HM quantities which occur in the plane wave are components of an eigenvector r_{ij} of the matrix Z_{ij}, and the phase velocity of the wave is then an eigenvalue of that matrix,

$$\text{therefore : } \sum_{j=1}^{7} Z_{ij}\, r_j = V\, r_i$$

The phase velocities of the various modes are then the roots of the seventh degree equation given by :

$$\text{DET } |Z_{ij} - V\,\delta_{ij}| = 0 \qquad 2.10.$$

It is therefore clear that seven kinds of plane waves can exist in a plasma.

The phase velocities can be found from eqn 2.10, and the simplified matrix for Z_{ij} (Herlofson, 1950) - and are :

$$V_{1,2} = \varepsilon\, V_A \cos\theta$$
$$V_{3,4} = \varepsilon\, V_+$$
$$V_{5,6} = \varepsilon\, V_-$$
$$V_7 = 0$$

Where V_A is the Alfvén speed and θ the angle between the wave normal and the constant magnetic field, the parameter $\varepsilon = +1$ for a wave propagating in the positive z direction, and -1 for the negative.

The value $V_7 = 0$ is the phase velocity of the entropy wave and will not be discussed further, while the other values represent essentially two magneto sound waves, or magneto acoustic waves, and two Alfvén waves. $V_{1,2}$ are then the phase velocities of the two Alfvén waves propagating at an angle θ to the magnetic field, $V_{3,4} = \varepsilon V_+$ are the two fast mode waves and $V_{5,6} = \varepsilon V_-$ are the two slow mode. Where for completeness

$$V_\pm = \{ \tfrac{1}{2}[V_A^2 + C_s^2 \pm [(V_A^2 + C_s^2)^2 - 4V_A^2 C_s^2 \cos^2\theta]^{\frac{1}{2}}]\}^{\frac{1}{2}}$$

and $C_s = (\rho)^{\frac{1}{2}}$ = sound speed.

All these quantities refer to the plasma frame but can easily be transformed to a frame which moves with say velocity u^o, i.e. :

$$V_{1,2} = u_z^o + V_A \cos$$
$$V_{3,4} = u_z^o + V_+$$
$$V_{5,6} = u_z^o + V_-$$
$$V_z = u_z^o$$

Where in this frame the entropy wave now has a positive velocity.

In the case of the Alfvén waves (Alfvén 1950) which are described by the vectors r_i and r_2 there are no perturbations of either the density or the entropy, or of those components of the velocity and magnetic field which lie in the plane through the unperturbed magnetic field $\underset{\sim}{B}^o$ and the direction of propagation, i.e.

$$\rho' = u_x' = u_z' = B_x' = s' = 0$$

and $u_y' \neq 0, \quad B_y' \neq 0$

In the case of the magneto-acoustic modes described by r_3 and r_4 (fast waves), and by r_5 and r_6 (slow waves) there are no perturbations for the entropy or components of velocity and magnetic field which are

at right angles to both $\underset{\sim}{B}^{o}$ and the direction of propagation, i.e.

$$u_y' = B_y' = s' = 0$$

and $\rho' \neq 0,\ u_x' \neq 0,\ u_z' \neq 0,\ B_x' \neq 0$

thus the magneto acoustic waves are plane polarized.

It is easy to see therefore how the HM modes arise in a plasma, and also how the phase velocities of the Alfvén and magneto-acoustic waves depend on the angle of propagation, however as mention will later be made of shocks, something should be said on the evolution and structure of shock's in plasmas.

2.3 Hydromagnetic Shocks and Discontinuities

Landau and Lifshitz (1959) showed that in a simple wave, points with larger density move faster than points with lower density thus the compressional magneto-acoustic mode can steepen to form a shock, whereas the Alfvén mode being purely transverse does not, and therefore propagates without distortion of its profile.

A simple wave is thus distorted when it propagates, parts with $\partial\rho/\partial z > 0$ being stretched and parts with $\partial\rho/\partial z < 0$ being compressed, and the situation is illustrated simply in Fig.2.1 which shows qualitatively the evolution of a typical shock wave.

The situation depicted in Fig.2.1c is unrealisable in practice since the density is a multi-valued function of the coordinate. In addition to the "simple" shock wave depicted below other discontinuities can also form and it is important now to classify these.

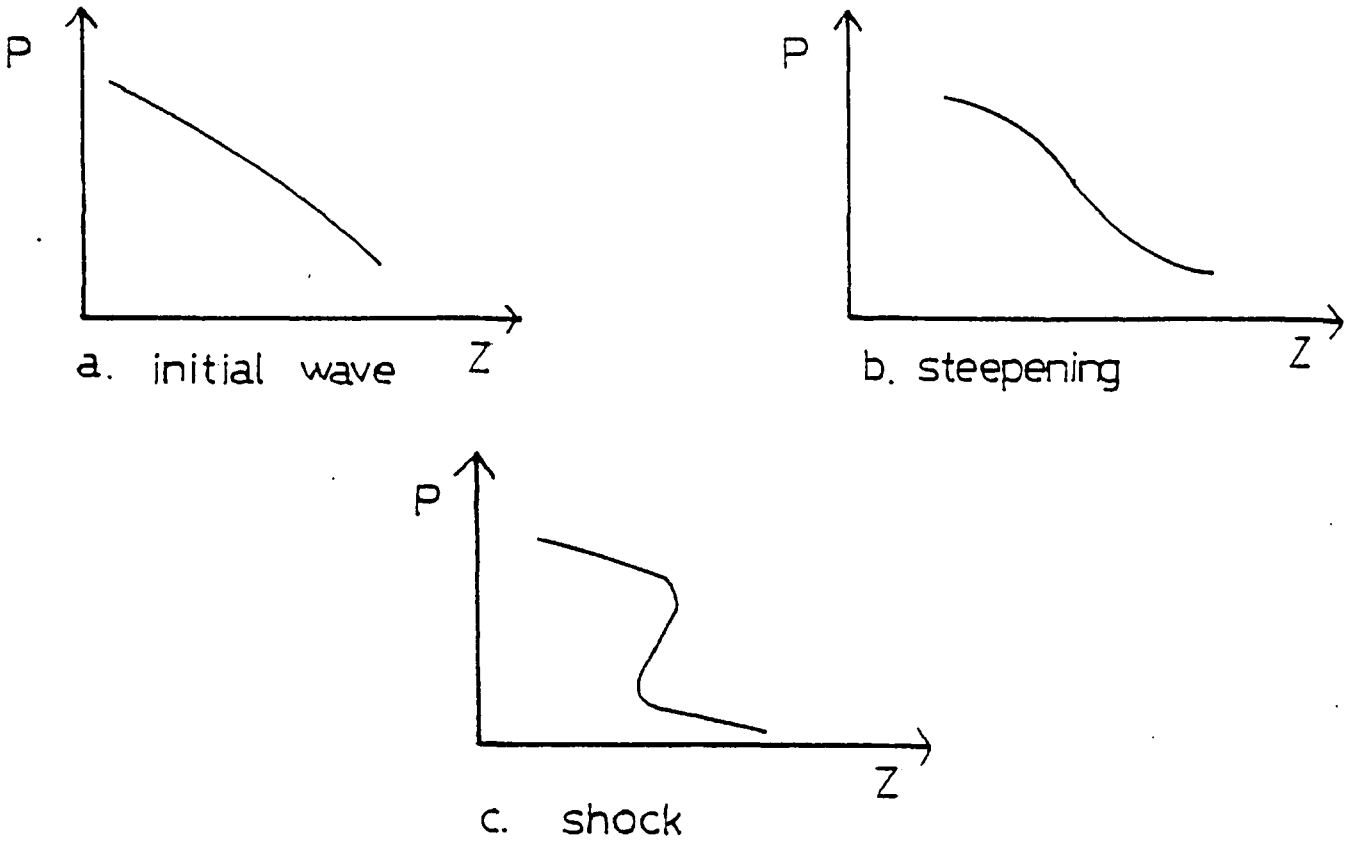

Figure 2.1 Evolution of a typical shock wave.

HM Discontinuities

Discontinuities in the macroscopic quantities are only possible when the differential equations which describe the state of the medium have characteristics – i.e. lines which separate different kinds of solution. Along the line of the discontinuity the differential equations represented by eqn 2.7 lose their meaning as they do not determine the resultant jumps in the HM quantities, and in this case it is necessary to specify as many boundary conditions as there are HM variables.

There are essentially three kinds of discontinuity :

1. Alfvén or Rotational Discontinuities

In these the velocity and magnetic field are discontinuous, while the density, pressure, and entropy are continuous, i.e.

$$\Delta \underset{\sim}{u} \neq 0, \quad \Delta B_t \neq 0 \quad \text{and}$$

$$\Delta \rho = \Delta p = \Delta s = 0$$

Here B_t = transverse field, and Δ represents the change in the parameter.

2. Contact Discontinuities

In this case pressure, velocity, and magnetic field are continuous; and density and entropy are discontinuous :

$$\Delta \rho \neq 0, \quad \Delta s \neq 0 \quad \text{and}$$

$$\Delta p = \Delta \underset{\sim}{u} = \Delta B_t = 0.$$

3. Tangential Discontinuities

Only the tangential component of velocity is discontinuous, i.e. $\Delta u_t \neq 0$, and

$$\Delta p = \Delta \rho = \Delta s = \Delta u_n = 0$$

The Alfvén discontinuity has assumed some importance in space plasma, for example in relation to the properties of the neutral sheet, which exhibits a 180° rotation of the magnetic field (Coroniti et al, 1980).

The width of these discontinuities increases with time according to the following empirical relationship,

$$L \approx \{ (\nu + \nu_m)t \}^{\frac{1}{2}}$$

where ν and ν_m are the HM and magnetic viscosities respectively, both of which are small in space and therefore permit the discontinuity to exist for an extended period and allow observation by spacecraft. For Alfvén discontinuities, the magnitude of the transverse components of the field and velocity do not change, and the vectors $\underset{\sim}{u}$ and $\underset{\sim}{B}$ only rotate through an angle on the discontinuity surface, therefore if the state in front is given, the state behind is determined by the single parameter ΔB_t. If the field rotates through 180° they can be said to be plane-polarized -

although observation shows that this is rarely the case.

In addition to shock waves, only the Alfvén discontinuities are moving with respect to the medium, for which $j \neq 0$ (j = current density). In this case the following condition must hold :

$$\frac{1}{\rho_1} = \frac{1}{\rho_2} = \frac{B^2_n}{4\pi j^2}$$

Thus it follows that the velocity of propagation of the Alfvén discontinuity is (appropriately) the Alfvén speed, i.e.

$$u_n = V_A = \frac{B_n}{(4\pi\rho)^{\frac{1}{2}}}$$

2.4 Structure of Discontinuities

In any calculation of structure, computational problems arise almost at once, even for collision-dominated shocks a quantitative calculation involves solution of the appropriate transport equations inside the shock, using either upstream or downstream states as a set of boundary conditions.

In the case of a collisionless regime, non-linear dissipation mechanisms must be taken into account. More will be said on this problem in a later section, but some insight can be gained by considering the simplest case, that of two groups of particles moving with different velocities, and with a small thermal spread in their velocities.

In this case the relevant equations are :

$$\frac{\partial n}{\partial t} + \nabla.(n\underset{\sim}{u}) = 0 \qquad 2.11.$$

$$mn \frac{\partial \underset{\sim}{u}}{\partial t} + mn(\underset{\sim}{u}.\nabla)\underset{\sim}{u} = en(\underset{\sim}{E} + \underset{\sim}{u}\Lambda\underset{\sim}{B}) \qquad 2.12.$$

and a similar set for the other species.

$\underset{\sim}{E}$ and $\underset{\sim}{B}$ must also satisfy the Maxwell equations, i.e.

$$\nabla \Lambda \underset{\sim}{B} = \mu_o \underset{\sim}{j} + \frac{\partial \underset{\sim}{E}}{\partial t} ,$$

$$\nabla . \underset{\sim}{B} = 0 \qquad 2.13.$$

Equations 2.11 - 2.13 can be used to consider a shock propagating with velocity u_1 in the direction of negative z : in this case, the plasma ahead of the wave, i.e. at $z = -\infty$, is characterised by the following parameters :

$$\underset{\sim}{E} = 0, \ \underset{\sim}{B}_y = \underset{\sim}{B}_z = 0, \ \underset{\sim}{B}_x = \underset{\sim}{B}_{x_1}$$

$$\underset{\sim}{u}_e = \underset{\sim}{u}_i = 0, \quad \text{and } n_e = n_i = n$$

Therefore over the whole range, i.e. $-\infty < z < +\infty$, we have from equations 2.11 through 2.13

$$E_x = E_z = B_y = B_z = U_{ex} = u_{ix} = 0$$

In order to consider the state of the plasma inside the discontinuity it is useful to change to a frame which is moving at the wave speed u_1, this has the particular advantage that all quantities are time independent and functions only of x and y.

Therefore, in this frame we have

$$E_y \equiv E = -u_1 B_1 , \quad \text{and} \quad E_x = E_z = 0$$

the only other assumption being the plasma approximation, or quasi-neutrality,

$$n_e = n_i \equiv n$$

Under these conditions we have

$$u_{ez} = u_{iz} \equiv u_z$$

It therefore follows from Maxwell's equation (2.13) that :

$$j_y = \frac{1}{\mu_o} \frac{dB_x}{dz}$$

and as $j_y = -neu_{ey}$

$$u_{ey} = - \frac{1}{\mu_o ne} \frac{dB_x}{dz} \qquad 2.14.$$

Combining components of equation 2.12 for both species gives

$$m_i \, n \, u_z \frac{du_z}{dz} = - \frac{d}{dz} B_x^2 \qquad 2.15.$$

which can be written as :

$$u_z = \frac{B_1^2 - B_x^2}{m_i \, n \, u_1} + u_1 \qquad 2.16.$$

and for the y-component

$$m_e \, n \, u_z \frac{du_{ey}}{dz} = - ne \, E_y - ne \, u_z \, B_x - m_e \, n \, u_{ey} \, \nu \qquad 2.17.$$

where the term with ν represents a dissipative mechanism.

If the expression for $E_y = - u_1 \, B_1$ is used along with equations 2.14 and 2.15 an expression for B can be obtained :

$$\frac{d^2B}{d\tau^2} + \frac{\nu dB}{d\tau} + \phi(B) = 0 \qquad 2.18.$$

where $d\tau = dz/u_z$ (Sagdeev 1962)

and

$$\phi(B) = \omega_{Be} \, u_1^2 \, \{ \frac{B(B^2 - B_1^2)}{m_i n \, u_1^2} - (B - B_1) \}$$

ω_{Be} = electron Langmuir frequency. Equation 2.18 determines the magnetic field inside the shock. As for the field at $\tau = +\infty$, i.e. behind the shock, in this region $\frac{dB}{d\tau} = \frac{d^2B}{d\tau^2} = 0$ so in this region $\phi(B) = 0$, which has three solutions viz :

$$B^1 = B_1 \quad \text{and}$$

$$B^{2,3} = -\tfrac{1}{2} B_1 \pm [\tfrac{1}{4} B_1^2 + m_i n\, u_1^2]^{\frac{1}{2}} \qquad 2.19.$$

where superscripts refer to the number of the solution.

The solution $B^1 = B_1$ is particularly interesting as it corresponds to a shock wave in which the upstream and downstream conditions are identical, it therefore describes a soliton - hence for the soliton solution

$$B\Big|_{z=-\infty} = B\Big|_{z=+\infty}$$

Of the other two solutions, B^2 and B^3, if the positive sign is taken in 2.19 to give

$$B^2 = -\tfrac{1}{2} B_1 + [\tfrac{1}{4} B_1^2 + m_i n\, u_1^2]^{\frac{1}{2}}$$

this then corresponds to a true shock as the final state is different from the initial. However if the negative sign is taken the result implies that the transverse magnetic field changes sign - which it cannot do, thus the solution B^3 does not correspond to a shock solution, and the positive sign must be taken.

For the corresponding situation ahead of the shock, i.e. at $\tau = -\infty$ the magnetic field should approach B_1 monotonically.

Returning now to equation 2.18 - i.e.

$$\frac{d^2B}{d\tau^2} + \frac{dB}{d\tau} + \phi(B) = 0$$

this equation has the form of a 1-D anharmonic oscillator, whose potential energy is given by :

$$V(B) = \int_{B_1}^{B} \phi(\xi)\, d\xi = \tfrac{1}{2} (B-B_1)^2 \left[\frac{(B+B_1)^2}{m_i n\, u_1^2} - 1\right]$$

which can be represented diagrammatically in Figure 2.2.

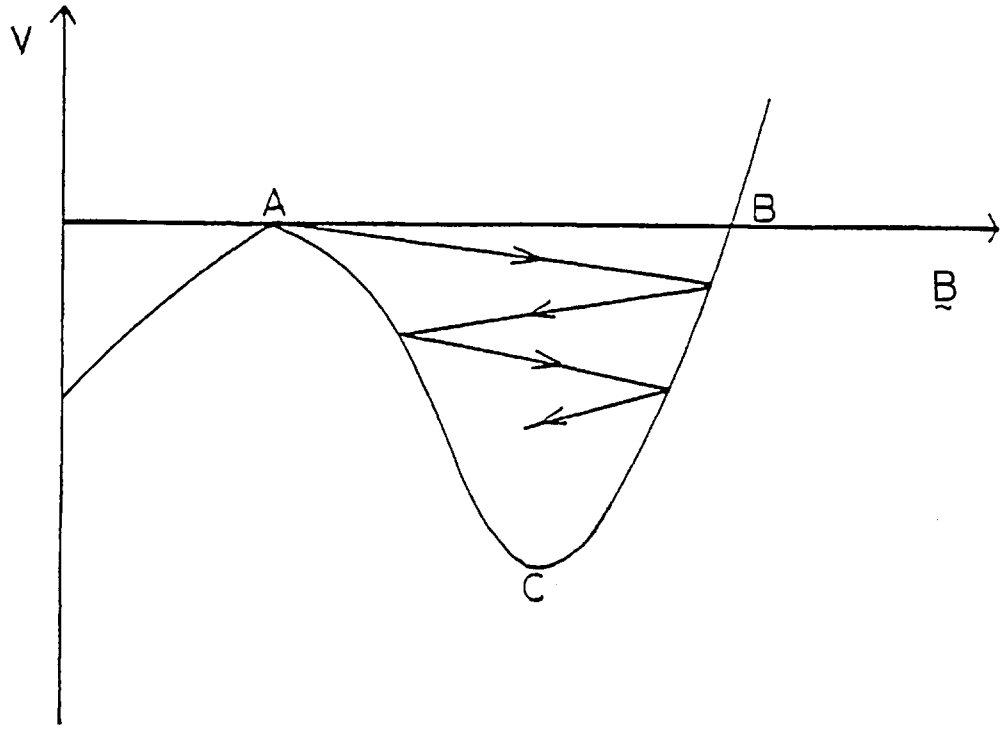

Figure 2.2 Plot of potential "V" against the field $\underset{\sim}{B}$.

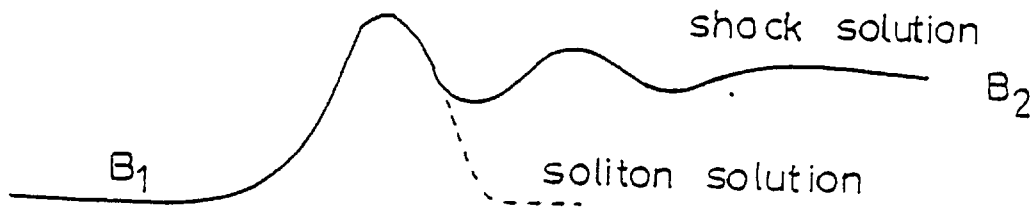

Figure 2.3 Cross section through a collisionless shock.

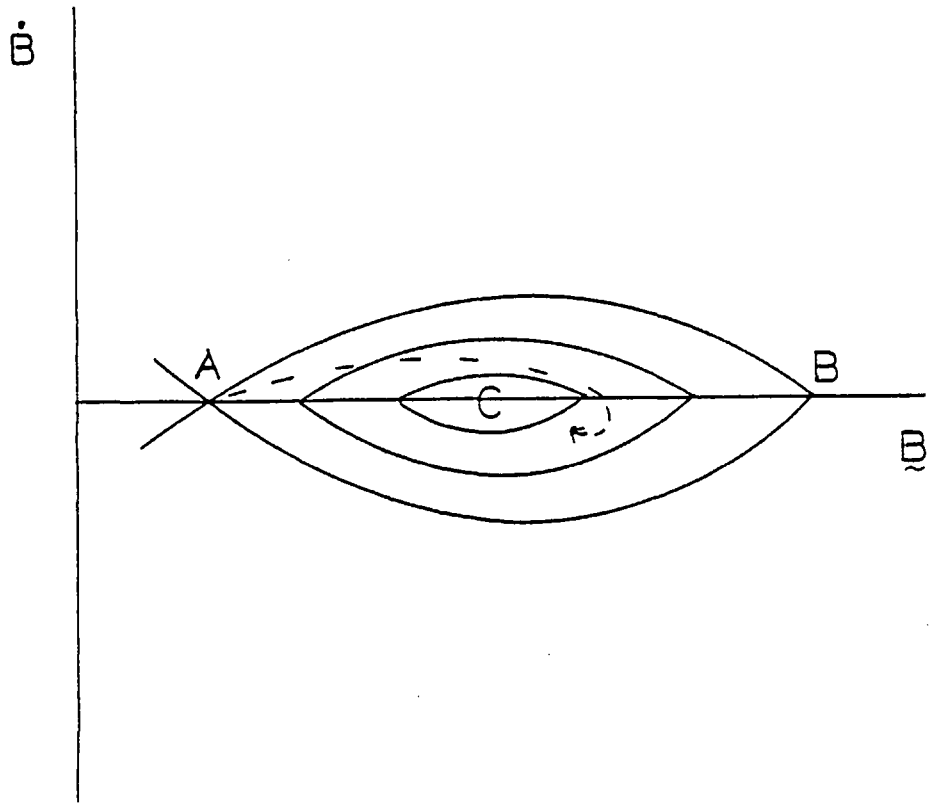

Figure 2.4 Phase space trajectories corresponding to Figure 2.2.

The point A corresponds to the initial state for which $\frac{dB}{d\tau} = \frac{d^2B}{d\tau^2} = 0$, and $B = B_1$; however, due to non-linear damping effects, the state shows a zig-zag approach to the final equilibrium point C; this point therefore corresponds to the final state for which the following are true :

$$\frac{dB}{d\tau} = \frac{d^2B}{d\tau^2} = 0$$

and

$$B = B_2$$

This is made clearer if the shock profile is drawn (Fig. 2.3), and is representative of a collisionless shock.

It can therefore be seen that without dissipative terms the solution is just a soliton, hence dissipation of some kind is necessary to convert a soliton into a shock solution (Tidman and Krall, 1971; Akhiezer et al, 1975). This may be seen from Fig. 2.2. The corresponding phase-space trajectories are shown in Fig.2.4, and represent the variation of the magnetic field in a shock wave; the letters A, B and C having the same meaning as in Fig. 2.2.

2.5 Summary

The sections of this chapter have attempted to show, albeit from a mathematical standpoint, how the various hydromagnetic modes - especially the Alfvén mode - can arise. Later sections described the various kinds of shocks and discontinuities which can arise and are of relevance to this work; it concluded with a brief excursion into the methods of calculating the parameters which are of importance in the context of the discontinuities.

CHAPTER 3

DEDUCTIONS FROM LINEAR THEORY

3.1 Introduction

If the magnetosphere is free from perturbing influences it will tend toward a configuration in which the electrical equipotential surfaces are parallel to the magnetic field.

In response to a localised perturbation, which may exist for example in the magnetotail, a readjustment of potential occurs throughout the flux tube linking the region of disturbance. The time required for this readjustment to take place depends on the speed at which electric fields and their associated currents propagate along the field lines - i.e. the Alfvén Speed.

In cases where there is a convective motion of the magnetospheric plasma relative to the perturbation region, dynamic equilibrium can be reached whereby currents generated by the disturbance flow continuously away from the region along the convecting flux tubes. These currents can suffer reflection at the ionospheric interface but do not return to the source region because of plasma convection. The assumption is therefore made that a discontinuity exists in the electric field at a point in the distant magnetotail; such a discontinuity being necessary to account for the "Inverted V events". Regardless of the mechanism for generating this field it will propagate towards the ionosphere along a flux tube as a shear-mode Alfvén wave (cf. Chapter 1).

The presence of convection in the model is important as it

essentially controls the orientation of the wave, as well as carrying away energy which may be deposited in the form of heat, thereby ensuring that the cold plasma approximation remains valid.

The picture is therefore of a shear-mode Alfvén wave propagating along flux tubes which pass through the cold polar wind plasma existing in the lobe-regions of the magnetosphere. This may be summarised by Fig. 3.1 and by reference to the Introduction in Chapter 1.

3.2 Mathematical Formulation

The equations which describe the above situation are just those of classical electrodynamics, i.e. the Lorentz equation and Maxwell's equations, viz. :

$$\frac{\partial \underset{\sim}{v}}{\partial t} + (\underset{\sim}{v}.\nabla)\ \underset{\sim}{v} = \frac{e}{m}(\underset{\sim}{E} + \underset{\sim}{v} \Lambda \underset{\sim}{B}) \qquad 3.1.$$

and the equation of continuity :

$$\frac{\partial n}{\partial t} + \nabla.(n\ v) = 0 \qquad 3.2.$$

These equations are true for both electrons and ions where $\underset{\sim}{v} = (v_x, v_y, v_z)$ and $\underset{\sim}{B} = (B_x, B_y, B_z)$ and $\underset{\sim}{E} = (E_x, E_y, E_z)$.

$$\nabla \Lambda B = \mu_o \underset{\sim}{j} + \frac{\partial \underset{\sim}{D}}{\partial t}, \qquad \nabla.\underset{\sim}{B} = 0 \qquad 3.3,\ 3.4.$$

when $\underset{\sim}{j}$ = current density and $\underset{\sim}{D}$ = displacement current.

The analysis can proceed in almost any frame of reference - but the two most useful are the plasma, and wave frame's, where equations linking the parameters in the different frames are well known. It is useful, initially, to formulate the problem in the wave frame, which has the advantages that the problem is time-independent (i.e. all $\partial/\partial t = 0$), and all variables are functions only of x.

The geometry of the frame is shown in Fig. 3.2 and is such

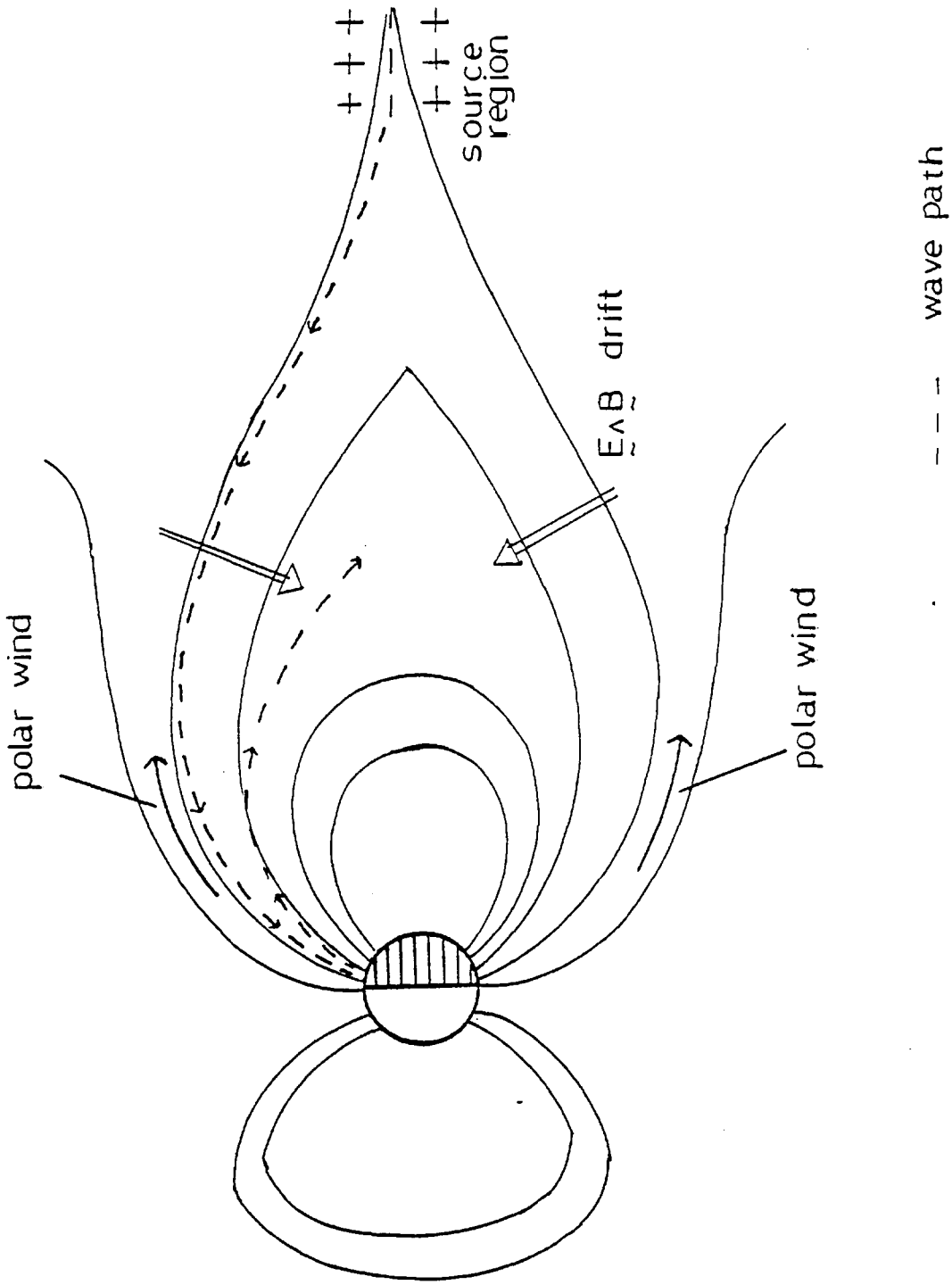

Figure 3.1 Schematic of an Alfvén wave and cold polar wind plasma in the vicinity of the plasma sheet boundary (refer to text).

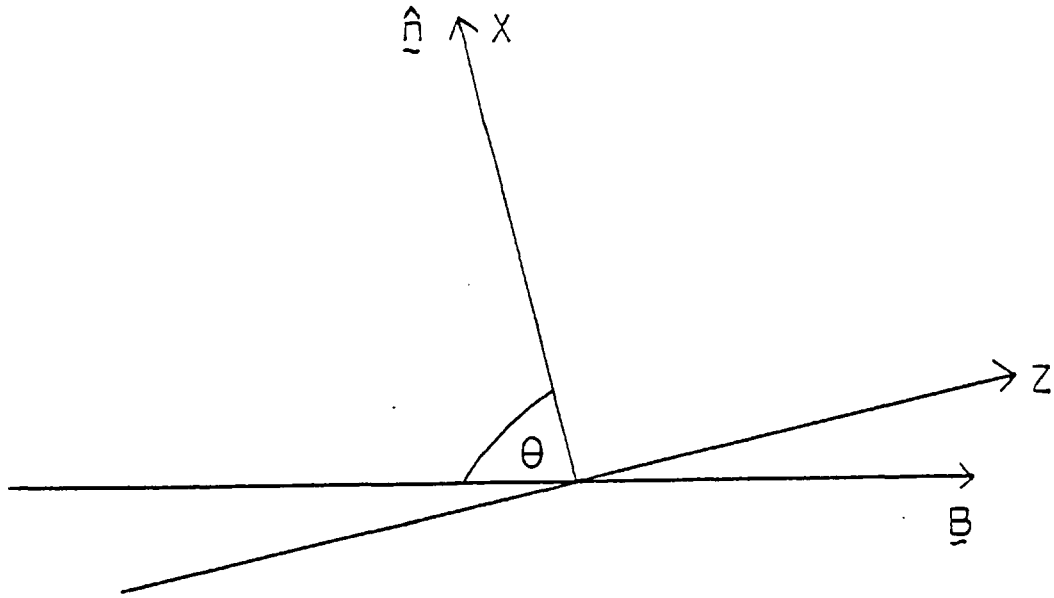

Figure 3.2 Geometry of the wave frame.

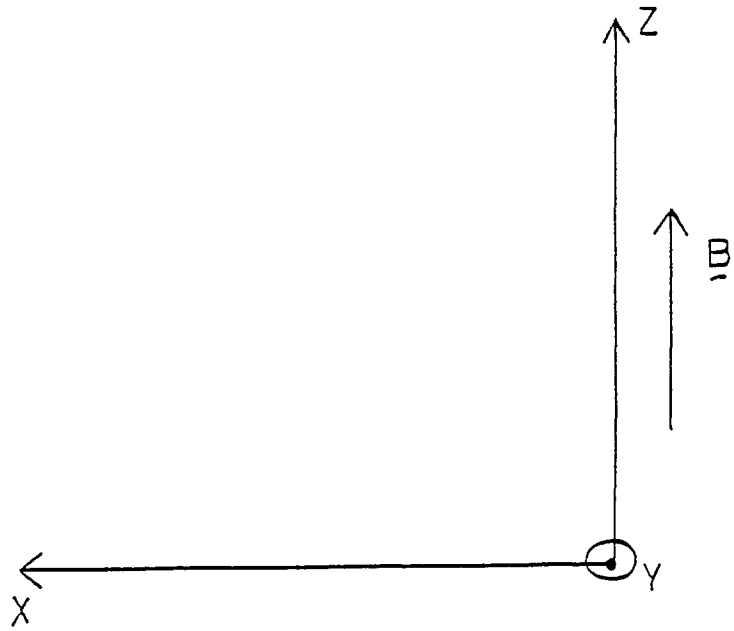

Figure 3.3 Geometry of the plasma frame.

that the x-axis is coincident with the wave normal, which makes an angle θ with the magnetic field direction. The situation here is one of limiting flow normal to the wave, with plasma streaming into the wavefront, and far ahead of the wave is taken to be at $x = -\infty$.

Equations 3.1 - 3.4 now become :

$$\underset{\sim}{V}.\nabla\underset{\sim}{V} = \frac{e}{m}(\underset{\sim}{E} + \underset{\sim}{V} \Lambda \underset{\sim}{B}) \qquad 3.5.$$

$$\nabla.(n\,\underset{\sim}{V}) = 0 \qquad 3.6.$$

$$\nabla.\underset{\sim}{B} = 0 \qquad 3.7.$$

$$\nabla\Lambda\underset{\sim}{B} = \mu_o\, e\, (n_i\, \underset{\sim}{V}_i - n_e\, \underset{\sim}{V}_e) \qquad 3.8.$$

n_i and n_e are the number densities of ions and electrons respectively, and by the plasma approximation we can write,

$$n_i = n_e = n$$

then 3.8 becomes

$$\nabla\Lambda\underset{\sim}{B} = \mu_o\, n_e\, (\underset{\sim}{V}_i - \underset{\sim}{V}_e)$$

On this assumption and equation 3.7, we also have

$$\underset{\sim}{B}_x = \underset{\sim}{B}_{xo} = \text{constant} \qquad 3.9.$$

The set of equations consists therefore of the components of 3.5 for electrons and protons, and equation 3.9, which are just,

$$m_e U \frac{du}{dx} = -e (E_x + V_e \tilde{B}_z - W_e \tilde{B}_y) \qquad 3.10.$$

$$m_e U \frac{dV_e}{dx} = -e (E_y + W_e \tilde{B}_x - U \tilde{B}_z) \qquad 3.11. \quad \text{Electrons}$$

$$m_e U \frac{dW_e}{dx} = -e (U \tilde{B}_y - V_e \tilde{B}_x) \qquad 3.12.$$

$$m_p U \frac{du}{dx} = e (E_x + V_p \tilde{B}_z - W_p \tilde{B}_y) \qquad 3.13.$$

$$m_p U \frac{dV_p}{dx} = e (E_y + W_p \tilde{B}_x - U \tilde{B}_z) \qquad 3.14. \quad \text{Protons}$$

$$m_p U \frac{dW_p}{dx} = e (U \tilde{B}_y - V_p \tilde{B}_x) \qquad 3.15.$$

and

$$\frac{d\tilde{B}_y}{dx} = \mu_o n e (W_p - W_e) \qquad 3.16.$$

$$\frac{d\tilde{B}_z}{dx} = -\mu_o n e (V_p - V_e) \qquad 3.17. \quad \text{Maxwell}$$

where subscripts e and p refer to electrons and protons respectively, the notation $\underset{\sim}{V} = (U, V, W)$ has been used, $\tilde{E}_y = \text{const} = U_x B_{xo}$, and $\tilde{E}_z = 0$. Ahead of the wave, at $x = -\infty$ B_x and B_z are constants, and $n \to N$

$\therefore$ from continuity (eqn 3.2)

$$n U_x = N U_{xo} \qquad 3.18.$$

hence the number density n can be eliminated.

The above set of equations (3.10-3.17) can be used to obtain several constants of the motion, from which it is possible to eliminate either the protons, or the electrons.

A first step is to obtain expressions for the electric field,

$\therefore$ multiplying 3.10 by m_p and 3.13 by m_e and subtracting $\to$

$$0 = E_x\,(m_e+m_p) + m_e(V_p\,\tilde{B}_z - W_p\,\tilde{B}_y) + m_p(V_e\,\tilde{B}_z - W_e\,\tilde{B}_y)$$

$$\therefore \qquad \tilde{E}_x = \frac{1}{(m_e+m_p)}\left\{\tilde{B}_y(m_e\,W_p + m_p\,W_e) - \tilde{B}_z(m_e\,V_p + m_p\,V_e)\right\}$$

The procedure now is to take linear combinations of the component equations and derive the appropriate constants of the motion :

Adding eqn 3.10 and eqn 3.13 gives an expression which can be interpreted in terms of the stress :

$$U\frac{du}{dx}(m_p + m_e) = e\left\{\tilde{B}_z(V_p - V_e) + \tilde{B}_y(W_e - W_p)\right\} \qquad 3.19.$$

this equation can therefore replace 3.10 and 3.13. The full set is then equations 3.11, 3.12, 3.14, 3.15, 3.16, 3.17 and 3.19.

Combining 3.11 and 3.14 gives

$$m_e\,u\frac{dV_e}{dx} + m_p\,U\frac{dV_p}{dx} = e\,(E_y + W_p\,\tilde{B}_x - U\,\tilde{B}_z) - e\,(E_y + W_e\,\tilde{B}_x - U\,\tilde{B}_z)$$

$$= e\,\tilde{B}_x\,(W_p - W_e)$$

but from Maxwell's equation (3.16)

$$(W_p - W_e) = \frac{1}{\mu_o\,n\,e}\,\frac{d\tilde{B}_y}{dx}$$

$$\therefore \qquad m_p\,U\frac{dV_p}{dx} + m_e\,U\frac{dV_e}{dx} = \frac{\tilde{B}_x}{\mu_o\,n}\,\frac{d\tilde{B}_y}{dx}$$

If n is now eliminated by using 3.18 (i.e. $n\,u = N\,U_{xo}$)

$$m_e\frac{dV_e}{dx} + m_p\frac{dV_p}{dx} = \left(\frac{\tilde{B}_x}{\mu_o\,N\,U_{xo}}\right)\frac{d\tilde{B}_y}{dx}$$

and this can be written in "integral" form as

$$m_e\,V_e + m_p\,V_p - \left(\frac{\tilde{B}_{xo}}{\mu_o\,N\,U_{xo}}\right)\tilde{B}_y = 0 \qquad 3.20.$$

this equation can then be used to eliminate V_p.

Similarly 3.12 and 3.15 can be added to give

$$m_p U \frac{dW_p}{dx} + m_e U \frac{dW_e}{dx} = e (U \tilde{B}_y - V_p \tilde{B}_x) - e (U \tilde{B}_y - V_e \tilde{B}_x)$$

$$= -e \tilde{B}_x (V_p - V_e)$$

and using $-(V_p - V_e) = \frac{1}{\mu_o n e} \frac{d\tilde{B}_z}{dx}$

$$m_p \frac{dW_p}{dx} + m_e \frac{dW_e}{dx} = \frac{\tilde{B}_x}{\mu_o n u} \frac{d\tilde{B}_z}{dx} = \left(\frac{\tilde{B}_x}{\mu_o N U_{xo}}\right) \frac{d\tilde{B}_z}{dx}$$

where $n u = N U_{xo}$

Again, in integrable form :

$$m_p W_p + m_e W_e - \left(\frac{\tilde{B}_{xo}}{\mu_o N U_{xo}}\right) \tilde{B}_z = -\left(\frac{\tilde{B}_{xo}}{\mu_o N U_{xo}}\right) \tilde{B}_{zo} \qquad 3.21.$$

and 3.21 can be used to eliminate W_p.

Finally, combining 3.10 and 3.13, and using Maxwell's equations gives :

$$\mu_o n u \frac{du}{dx} (m_p + m_e) = -\tfrac{1}{2} \frac{d}{dx} (\tilde{B}_z^2 + \tilde{B}_y^2)$$

again, using $n u = N U_{xo}$, they integrate to give :

$$\mu_o N U_{xo} (m_p + m_e) U + \tfrac{1}{2} (\tilde{B}_z^2 + \tilde{B}_y^2) = N (m_p + m_e) U_{xo}^2 + \tfrac{1}{2} \tilde{B}_z^2$$

i.e.

$$2\mu_o N U_{xo} (m_p + m_e) U_x + \tilde{B}_z^2 + \tilde{B}_y^2 = \mu_o 2 N (m_p + m_e) U_{xo}^2 + \tilde{B}_{zo}^2 \qquad 3.22$$

Equations 3.20, 3.21 and 3.22 state constants of the motion, the remaining equations constitute a set of four coupled differential equations for calculating B_y, B_z, V and W.

Before these equations could be computed, they would need to be de-dimensionalized, but before doing this it is necessary to examine the other frame, i.e. the plasma frame - and to do linear theory in order to relate the space and time scales.

3.3 The Plasma Frame and Linear Theory

In the plasma frame $\partial/\partial t \neq 0$, and the orientation can be chosen such that the magnetic field $\underset{\sim}{B}$, is along the z-axis (Fig. 3.3). The Lorentz equation for electrons is now :

$$m_e \frac{Dv}{Dt} = -e\,(\underset{\sim}{E} + \underset{\sim}{V} \wedge \underset{\sim}{B})$$

where $\frac{D}{Dt} \equiv \partial/\partial t + V.\nabla$

In component form this is just

$$m_e \frac{du}{dt} = -e\,E_x - e\,V_e\,\underset{\sim}{B}_o \qquad 3.23.$$

$$m_e \frac{dV_e}{dt} = -e\,E_y + e\,U\,\underset{\sim}{B}_o \qquad 3.24.$$

$$m_e \frac{dW_e}{dt} = -e\,E_z \qquad 3.25.$$

From these equations U, V and W can be determined. Equations 3.23 → 3.25 can be linearized on the assumption that all variables are equal to their equilibrium values plus a small perturbation which is proportional to $\exp[\sigma t + K(x \sin\theta + z \cos\theta]$. Here, σ is the temporal growth rate, K the spatial, and are related through $V = \sigma/K$. Under this assumption the linearized form of equations 3.23 → 3.25 are :

$$\sigma\, m_e\, U = -e\,E_x - e\,V\,\underset{\sim}{B}_o \qquad 3.26.$$

$$\sigma\, m_e\, V = -e\,E_y + e\,U\,\underset{\sim}{B}_o \qquad 3.27.$$

$$\sigma\, m_e\, W = -e\,E_z \qquad 3.28.$$

Rearranging the second of these equations for V, and substituting into the first gives, upon using $\Omega = e\,B_o/m_e$

$$U = \frac{e}{\sigma m_e} \frac{1}{(1 + \frac{\Omega_e^2}{\sigma^2})} \{ E_x + \frac{\Omega_e}{\sigma} E_y \}$$

as the current density $\underset{\sim}{j} = n\ e\ (\underset{\sim}{V}_p - \underset{\sim}{V}_e)$ we therefore have

$$\underset{\sim}{j}_x = \alpha E_x + \beta E_y \qquad 3.29.$$

where α and β are constants defined by

$$\alpha = n e^2 \sigma \{ [m_p (\sigma^2 + \Omega_p^2)]^{-1} + [m_e (\sigma^2 + \Omega_e^2)]^{-1} \}$$

and

$$\beta = \frac{n e^2 \Omega_e}{m_e} (\sigma^2 + \Omega_e^2)^{-1}$$

Similarly for $\underset{\sim}{j}_y$

$$\underset{\sim}{j}_y = \alpha E_y - \beta E_x \qquad 3.30.$$

and for j_z, as we have

$$\sigma m_e W = e E_z$$

$$\therefore \quad j_z = \frac{n e^2 E_z}{m_e \sigma}$$

therefore

$$\underset{\sim}{j}_z = \frac{\omega_p^2 E_z}{\sigma} \qquad 3.31.$$

where ω_p is the plasma frequency.

The current densities can also be related to the orientation of the wave by the following procedure :

From Faraday's law

$$\nabla \Lambda \underset{\sim}{E} = - \frac{\partial B}{\partial t}$$

taking the curl of both sides, gives

$$\nabla \Lambda (\nabla \Lambda \underset{\sim}{E}) = - \nabla \Lambda \frac{\partial B}{\partial t}$$

and as perturbed quantities vary as

$$\exp \{ \sigma t + K(x \sin \theta + z \cos \theta) \}$$

we have

$$\nabla \Lambda (\nabla \Lambda \underset{\sim}{E}) = - \sigma \mu_o \underset{\sim}{j}$$

which upon using $\nabla \Lambda (\nabla \Lambda \underset{\sim}{E}) = \nabla (\nabla.E) - \nabla^2 E$ becomes

$$\sigma \mu_o \underset{\sim}{j} = K^2 E - K (K.E)$$

but as $K_x = K \sin \theta$, $K_y = 0$ and $K_z = K \cos \theta$ we have finally

$$K^2 (\cos^2 \theta E_x - \sin \theta \cos \theta E_z) = \sigma \mu_o j_x \qquad 3.32.$$

$$K^2 E_y = \sigma \mu_o j_y \qquad 3.33.$$

$$K^2 (\sin^2 \theta E_z - \sin \theta \cos \theta E_x) = \sigma \mu_o j_z = \mu_o \omega_p^2 E_z \qquad 3.34.$$

Equations 3.32 - 3.34 are the expressions which relate the component current densities to the orientation of the wave.

The equations 3.29 through 3.34 enable expressions for the ratios of the electric fields to be derived, this may be seen by combining equations 3.30 and 3.33 :

$$\frac{K^2 E_y}{\mu_o \sigma} = \alpha E_y - \beta E_x$$

$$E_y (\alpha - \frac{K^2}{\mu_o \sigma}) = \beta E_x$$

$$\therefore \quad \frac{E_y}{E_x} = \frac{\beta}{(\alpha - \frac{K^2}{\mu_o \sigma})} \qquad 3.35.$$

which has the advantage of being independent of θ.

Similarly from 3.31, i.e. $j_z = \frac{\omega_p^2 E_z}{\sigma}$ and equation 3.34 we have

$$\sigma \mu_o \frac{\omega_p^2 E_z}{\sigma} = K^2 \sin^2 \theta E_z - K^2 \sin \theta \cos \theta E_x$$

$$E_z (K^2 \sin^2 \theta - \mu_o \omega_p^2) = K^2 \sin \theta \cos \theta E_x$$

$$\therefore \quad \frac{E_z}{E_x} = \frac{\sin \theta \cos \theta}{\sin^2\theta - \frac{\omega_p^2 \mu_o}{K^2}} \qquad 3.36.$$

which is independent of Ω. Rearranging equation 3.36 for E_z and substituting in equation 3.32 gives

$$E_x K^2 \cos^2 \theta \left(1 - \frac{\sin^2\theta K^2}{K^2\sin^2\theta - \omega_p^2 \mu_o}\right) = \sigma \mu_o j_x$$

which reduces to

$$j_x = \frac{- E_x K^2 \omega_p^2 \cos^2 \theta}{\sigma (K^2\sin^2\theta - \omega_p^2 \mu_o)} \qquad 3.37.$$

which is also independent of Ω.

Equation 3.37 is for the general angle, however it simplifies considerably for the limit in which $\cos \theta \to 1$ and $\sin \theta \to 0$ to give

$$j_x = \left(\frac{K^2}{\sigma \mu_o}\right) \underset{\sim}{E}_x \qquad 3.38.$$

and from 3.33

$$j_y = \left(\frac{K^2}{\sigma \mu_o}\right) \underset{\sim}{E}_y \qquad 3.39.$$

If use is made of equations 3.29 and 3.30 these become

$$j_x = \alpha E_x + \beta E_y = \left(\frac{K^2}{\sigma \mu_o}\right) \underset{\sim}{E}_x$$

and $$j_y = \alpha E_y - \beta E_x = \left(\frac{K^2}{\sigma \mu_o}\right) \underset{\sim}{E}_y$$

which upon using 3.35 for E_y become

$$j_x = \underset{\sim}{E}_x \left\{ \alpha + \frac{\beta^2}{\left(\alpha - \frac{K^2}{\sigma \mu_o}\right)} \right\} \qquad 3.40.$$

and

$$j_y = -\left(\frac{K^2}{\sigma \mu_o}\right) \underset{\sim}{E}_y \qquad 3.41.$$

Equation 3.37, for the general angle can be rearranged to give

$$(K^2 \sin^2 \theta - \omega_p^2)\, \mu_o \sigma\, j_x = -\omega_p^2 K^2 \cos^2 \theta\, \underset{\sim}{E}_x \qquad 3.42.$$

and it is from a combination of equation 3.40 with 3.42 that the dispersion relation can be derived. However, before proceeding in this direction it is useful to ask what form the equations take which relate the wave and plasma frame quantities.

3.4 General Relationships between the Frames

The velocity perturbations occurring in the wave frame can be simply related to the parallel, perpendicular and z components of the electric field in the plasma frame. In this case expressions can be obtained by an appropriate frame transformation, which involves rotation and translation (Fig. 3.4). In Fig. 3.4, $\parallel$ and $\perp$ refer to directions parallel and perpendicular to the magnetic field. From the figure, the velocity of the frame in the parallel direction is just W sec θ, and the component velocities are given by :

$$V_x = V_\parallel \cos \theta + V_\perp \sin \theta$$

and

$$V_z = -V_\parallel \sin \theta + V_\perp \cos \theta$$

and wave vector components are

$$K_\parallel = K \cos \theta, \qquad K_\perp = K \sin \theta, \qquad K_z = 0$$

Letting primes denote quantities in the wave frame, expressions can

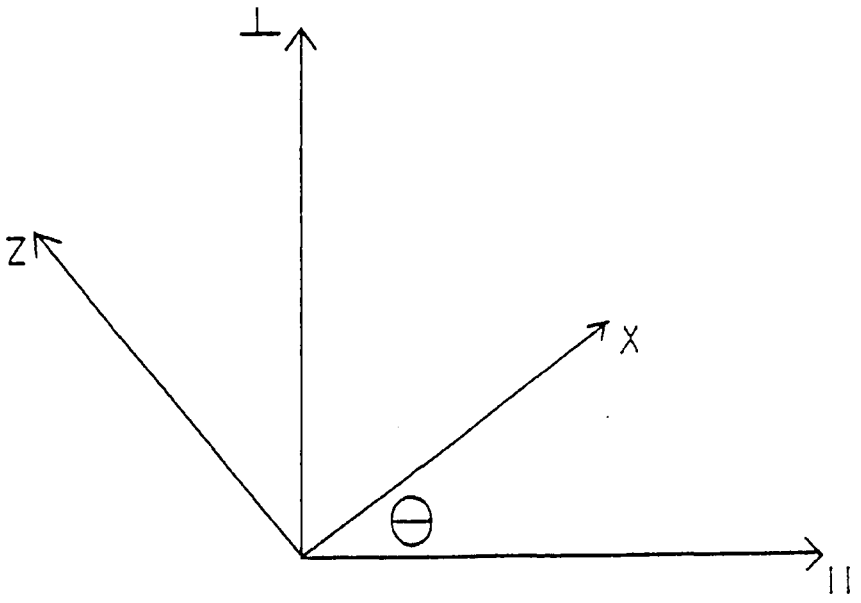

Figure 3.4 Relationship between the frames.

be written down which relate the parameters between the two frames. Hence :

$$E'_{\parallel} = E_{\parallel}$$

$$E'_{\perp} = E_{\perp} - W \sec\theta \, b_z$$

$$E'_z = E_z + W \sec\theta \, b_{\perp} = 0$$

where b_z is the perturbation in the z-direction and is given by

$$b_z = (E_{\perp} \cos\theta - E_{\parallel} \sin\theta)/W$$

where W is the phase velocity, and can be obtained from the dispersion relation (see Section 3.5).

For the other components of the magnetic field perturbation we have

$$b_{\parallel} = -b_{\perp} \operatorname{Tan}\theta$$

$$b_x = b_{\parallel} \cos\theta + b_{\perp} \sin\theta = 0$$

and $$b_y = b_{\perp} \sec\theta = -E_z/W$$

The above equations therefore constitute a set of expressions for which the perturbed wave frame quantities are expressed as functions of plasma frame parameters.

3.5 Derivation of the Dispersion Relation

Equations 3.40 and 3.42 state

$$j_x = \underset{\sim}{E} \left\{ \alpha + \frac{\beta^2}{(\alpha - \frac{K^2}{\sigma \mu_o})} \right\} \qquad 3.40.$$

$$(K^2 \sin^2\theta - \omega_p^2) \, \mu_o \, \sigma \, j_x = -\omega_p^2 K^2 \cos^2\theta \, \underset{\sim}{E}_x \qquad 3.42.$$

which may be combined to give

$$(K^2 \sin^2\theta - \omega_p^2)\left\{(\alpha^2 - \frac{\alpha K^2}{\mu_o \sigma}) + \beta^2\right\} = -\omega_p^2 (\alpha - \frac{K^2}{\mu_o \sigma})$$

$$\frac{K^2}{\mu_o \sigma}\cos^2\theta \qquad 3.43.$$

Proceeding as

$$\alpha + i\beta = \frac{\omega_p^2}{\Omega_e}\left\{\frac{1}{(\frac{\sigma}{\Omega_i} + i)} + \frac{1}{(\frac{\sigma}{\Omega_e} - i)}\right\}$$

$$\simeq \frac{\sigma\,\omega_p^2/\Omega_i\,\Omega_e}{1 + \frac{\sigma^2}{\Omega_i\,\Omega_e} - i\frac{\sigma}{\Omega_i}}$$

Writing $M^2 = \frac{\sigma^2\omega_p^2}{K^2\,\Omega_e\,\Omega_i}$, then

$$\frac{K^2(\alpha - i\beta)}{\sigma(\alpha^2 + \beta^2)} = \frac{1}{M^2}\{1 + \frac{\sigma^2}{\Omega_e\,\Omega_i} - i\frac{\sigma}{\Omega_i}\}$$

working on the real part, and using the equations

$$\frac{K^2\,\alpha}{(\alpha^2 + \beta^2)\sigma} = \frac{1}{M^2}(1 + \frac{\sigma^2}{\Omega_e\Omega_i}) \text{ and}$$

$$\frac{K^4}{(\alpha^2 + \beta^2)\sigma^2} = \frac{1}{M^4}([1 + \frac{\sigma^2}{\Omega_e\,\Omega_i}]^2 + \frac{\sigma^2}{\Omega_i^2})$$

Substituting in equation 3.40 gives

$$(K^2\sin^2\theta - \omega_p^2)\,(1 - \frac{1}{M^2}(1 + \frac{\sigma}{\Omega_e\,\Omega_i})) = -\omega_p^2\cos^2\theta$$

$$[\frac{1}{M^2}(1 + \frac{\sigma^2}{\Omega_e\,\Omega_i}) - \frac{1}{M^4}\{(1 + \frac{\sigma^2}{\Omega_e\,\Omega_i})^2 + \frac{\sigma^2}{\Omega_i^2}\}]$$

If we now put $\xi = M^2 - 1 - \sigma^2/\Omega_e\,\Omega_i$ and multiply by M^4/ω_p^2 to simplify, the above equation goes to :

$$\{ \frac{\sigma^2}{\Omega_e \Omega_i} \sin^2\theta - \xi - 1 - \frac{\sigma^2}{\Omega_e \Omega_i} \} \xi = - \cos^2\theta \{ \xi(1 + \frac{\sigma^2}{\Omega_e \Omega_i}) - \frac{\sigma^2}{\Omega_i^2} \}$$

which simplifies to :

$$\xi^2 + \xi \sin^2\theta + (\frac{\sigma^2}{\Omega_i^2}) \cos^2\theta = 0 \qquad 3.44.$$

Equation 3.44 is the required dispersion relation and is best seen by re-substituting for ξ as

$$\xi = M_A^2 - 1 - \sigma^2/\Omega_e \Omega_i$$

to give

$$\frac{u^2}{V_A^2} = 1 - \tfrac{1}{2} \sin^2\theta \pm \{ \tfrac{1}{4} \sin^4\theta + (\frac{\sigma}{\Omega_p})^2 \cos^2\theta \}^{\frac{1}{2}} - \frac{\sigma^2}{\Omega_e \Omega_p} \qquad 3.45.$$

where $M_A = \frac{u}{V_A}$ has been used in equation 3.45 and u is the phase velocity. The dispersion relation represented by equation 3.45 is shown plotted in Fig. 1.5, Chapter 1.

In equation 3.45 the positive sign corresponds to the Whistler mode and the negative sign to the shear mode.

In view of the comments made in the introduction in section 3.1 it is the shear mode wave which is of principal importance in this work. The growth rate, a quantity which can be estimated from the linear theory, can be found by writing equation 3.45 in the form :

$$\frac{u^2}{V_A^2} \approx \cos^2\theta + \tfrac{1}{2} \sin^2\theta \, (\frac{\sigma}{\Omega_p})^2 \frac{4 \cos^4\theta}{\sin^4 \theta} + \frac{\sigma^2}{\Omega_e \Omega_p}$$

and because $\theta \sim 90^\circ$, $\sin \theta \rightarrow 1$ $\therefore$

$$\frac{u^2}{V_A^2} \approx \cos^2\theta + 2\left(\frac{\sigma}{\Omega_p}\right)^2 \cos^2\theta + \frac{\sigma^2}{\Omega_e\,\Omega_p}$$

$$\approx \cos^2\theta + \left(2\cos^2\theta + \frac{\Omega_p}{\Omega_e}\right)\frac{\sigma^2}{\Omega_p^2}$$

Solving for σ^2/Ω_p^2 gives

$$\frac{\sigma^2}{\Omega_p^2} = \frac{u^2/V_A^2 - \cos^2\theta}{2\cos^2\theta + 1/1800} \qquad 3.46.$$

Hence σ can be found.

Equation 3.46 implies that there is imaginary σ unless the inequality $\cos\theta < M_A$ is satisfied. It also shows that for a wave propagating at an angle θ to the magnetic field, then, providing u can be estimated and the position in the magnetotail is known, at least approximately, then :

$$\Omega_p = 0.01525\ B(\gamma)\ \text{Hz}$$

and

$$V_A = 21.808\ \frac{B(\gamma)}{(n\ (\text{cm}^{-3}))^{\frac{1}{2}}}\ \text{km s}^{-1}$$

Then for $n \sim 0.1\ \text{cm}^{-3}$ and $B \sim 14\gamma$

$$\Omega_p = 0.214\ \text{Hz} \approx 0.2\ \text{Hz and } V_A = 965\ \text{km s}^{-1} \approx 10^3\ \text{km s}^{-1}$$

hence

$$\sigma = \left(\frac{u^2}{V_A^2} - \cos^2\theta\right)^{\frac{1}{2}} \approx \left(M_A^2 - \cos^2\theta\right)^{\frac{1}{2}} \qquad 3.47.$$

and 3.47 may be used to determine the growth rate.

3.6 Summary

This chapter has been concerned with formulating the problem in the most appropriate frames of reference, and with examining the

linearised equations in order to determine expressions which enable straightforward determination of parameters such as current density, and growth rate. Section 3.5 showed how the dispersion relation for the general case of oblique propagation may be derived (eqn 3.45), an expression which shows the relationship between the Alfvén Mach number ($M_A = u/V_A$) and the angle of propagation.

The formulation of the problem in the correct frame is necessary to enable the computation to proceed in a straightforward way, and this is given in sections 3.2 and 3.3.

The next chapter is concerned with a discussion of shock solutions and the process of computation.

CHAPTER 4

COMPUTATION

4.1 Introduction

The equations which goven the behaviour of a cold, collisionless plasma consisting of electrons and one species of ion may be obtained by considering velocity moments of the collisionless Boltzmann, or Vlasov equation in the absence of any effects due to turbulence or temperature, together with the Maxwell equations : Clemmow and Dougherty (1969). The Vlasov equation has the following well known form :

$$L[f] \equiv \left\{ \frac{\partial}{\partial t} + \underset{\sim}{V}.\frac{\partial}{\partial \underset{\sim}{r}} + \frac{\underset{\sim}{F}}{m}.\frac{\partial}{\partial \underset{\sim}{V}} \right\} f = 0$$

where L is the "Liouville operator", f the particle distribution function and $\underset{\sim}{F}$ is the force acting upon a particle and is taken to be the Lorentz force which is given by the following equation :

$$\underset{\sim}{F} = e_{\varepsilon} (\underset{\sim}{E} + \underset{\sim}{V} \Lambda \underset{\sim}{B})$$

where $\varepsilon = \pm$ depending on the particle species, and $\underset{\sim}{E}$, $\underset{\sim}{V}$ and $\underset{\sim}{B}$ are the electric, velocity and magnetic fields respectively.

In what follows we are primarily interested in the zeroth and first order moment equations, as these are just the conventional continuity and momentum equations, and may be obtained by multiplying the Vlasov equation by 1 and mv respectively, and integrating over velocity space : the equations to be solved therefore have the

following form :

$$\int L\,[f]\; d^3v \;=\; 0$$

and

$$\int mv\; L\,[f]\; d^3v \;=\; 0$$

For the first of these integrals we therefore have :

$$\frac{\partial}{\partial t}\int f\; d^3\underset{\sim}{v} + \left(\frac{\partial}{\partial \underset{\sim}{r}} \cdot \int \frac{\partial f}{\partial \underset{\sim}{V}}\; d^3\underset{\sim}{v}\right) + \int \left(\frac{\underset{\sim}{F}}{m} \cdot \frac{\partial f}{\partial \underset{\sim}{V}}\right) d^3\underset{\sim}{v} \;=\; 0$$

Writing the last term in the following way :

$$\int \left(\frac{\underset{\sim}{F}}{m} \cdot \frac{\partial f}{\partial \underset{\sim}{V}}\right) d^3\underset{\sim}{v} \;=\; \frac{e}{m}\left(E. \int \frac{\partial f}{\partial \underset{\sim}{V}}\; d^3v\right) + \frac{e}{m}\sum \int (\underset{\sim}{V} \wedge \underset{\sim}{B})\, \frac{\partial f}{\partial \underset{\sim}{V}}\; d^3\underset{\sim}{v}$$

where the Lorentz force has been substituted for $\underset{\sim}{F}$, and the summation is over all species present, however, if Gauss's theorem is applied to the first term, and the second is integrated by parts we obtain :

$$\int \left(\frac{\underset{\sim}{F}}{m} \cdot \frac{\partial f}{\partial \underset{\sim}{V}}\right) d^3v = \frac{e}{m}\left(E. \int \hat{\underset{\sim}{n}}\; f\; d^2\underset{\sim}{s}\right) - \frac{e}{m}\sum \int f\, \frac{\partial}{\partial \underset{\sim}{V}}\, (\underset{\sim}{V} \wedge \underset{\sim}{B})\; d^3\underset{\sim}{v}$$

where $\hat{\underset{\sim}{n}}$ is the unit vector normal to the surface, $\underset{\sim}{s}$, of integration.

The advantage of the above equation lies in the fact that the second term is identically equal to zero, while the first one vanishes due to f decreasing exponentially as $|\underset{\sim}{v}| \to \infty$; we therefore have :

$$\frac{\partial}{\partial t}\int f\; d^3v + \left(\frac{\partial}{\partial \underset{\sim}{r}} \cdot \int \underset{\sim}{V}\; f\; d^3\underset{\sim}{v}\right) \;=\; 0$$

or, as

$$n \equiv n(\underset{\sim}{r},t) = \int f \, d^3v \qquad \text{- particle density}$$

and

$$\underset{\sim}{u} \equiv \underset{\sim}{u}(\underset{\sim}{r},t) = \frac{\int \underset{\sim}{V} f \, d^3v}{\int f \, d^3v} \qquad \text{- hydrodynamic velocity}$$

We have finally :

$$\frac{\partial n}{\partial t} + \nabla.(n \, \underset{\sim}{u}) = 0$$

and this is just the continuity equation. If this process is followed through for the second integral, i.e.

$$\int m \, V \, L \, [f] \, d^3v = 0$$

(see Clemmow and Dougherty, p.347), the following well known set of equations are obtained :

$$m_\varepsilon \left(\frac{\partial \underset{\sim}{V}}{\partial t} + \underset{\sim}{V}_E . \nabla \underset{\sim}{V}_E\right) = e_\varepsilon \, (\underset{\sim}{E} + \underset{\sim}{V}_E \wedge \underset{\sim}{B}) \qquad 4.1$$

$$\frac{\partial n_\varepsilon}{\partial t} + \nabla . \, (n_\varepsilon \, \underset{\sim}{V}_E) = 0 \qquad 4.2$$

which are to be taken together with Maxwell's equations :

$$\nabla \wedge \underset{\sim}{E} = -\frac{\partial \underset{\sim}{B}}{\partial t} \qquad 4.3$$

$$\nabla \wedge \underset{\sim}{B} = \mu_o \, \underset{\sim}{j} + \frac{\partial \underset{\sim}{E}}{\partial t} \qquad 4.4$$

and

$$\nabla . \, \underset{\sim}{B} = 0 \qquad 4.5$$

where again ε takes the value $\pm$, depending on whether we are considering electrons or protons, and n_E and m_E are the number density and the mass respectively, and the velocity and magnetic field components are taken to be :

$$\underset{\sim}{V} = (u,v,w) \quad \text{and} \quad \underset{\sim}{B} = (B_x, B_y, B_z)$$

In the above equations, 4.1 through 4.5, we are interested in examining one-dimensional wave motion, consideration must therefore be given as to which is a suitable frame of reference in which to base the formulation. Despite the number of frames available, it is of advantage to work in the wave frame, as all quantities are then independent of time and functions only of x; in such a frame the components of equation 4.1 become :

$$m_\varepsilon u_\varepsilon \frac{du_\varepsilon}{dx} = e_\varepsilon (\underset{\sim}{E}_x + v_\varepsilon \underset{\sim}{B}_z - w_\varepsilon \underset{\sim}{B}_y) \qquad 4.6$$

$$m_\varepsilon u_\varepsilon \frac{dv_\varepsilon}{dx} = e_\varepsilon (w_\varepsilon \underset{\sim}{B}_o - u_\varepsilon \underset{\sim}{B}_z) \qquad 4.7$$

and

$$m_\varepsilon u_\varepsilon \frac{dw_\varepsilon}{dx} = e_\varepsilon (u_\varepsilon \underset{\sim}{B}_y - v_\varepsilon \underset{\sim}{B}_o) \qquad 4.8$$

In equation 4.4 the displacement current can be neglected, and if use is made of the equation for the current density j, i.e.

$$j = \sum_{(\text{species})} n\, e\, v$$

and furthermore, if the plasma approximation is assumed to be valid, i.e. if $n_p = n_e = n$, the components of 4.4 become :

$$\frac{d\underset{\sim}{B}_y}{dx} = \mu_o\, n\, e\, (w_p - w_e) \qquad 4.9$$

and

$$\frac{d\underset{\sim}{B}_z}{dx} = -\mu_o\, n\, e\, (v_p - v_e) \qquad 4.10$$

where subscriptios refer to protons and electrons. Finally, from 4.5 we have $B_x = B_{xo}$ = constant.

4.2 Structure and Properties of Equations 4.6 through 4.10

In considering the structure of the set of equations 4.6 through 4.10 it is an advantage to write the equations in their dimensionless form, and while this process is done fully later in the chapter it is necessary at this stage just to state the results : Saffman (1961) Hence

$$\frac{M_A\, u}{\gamma}\ \frac{dv_p}{dx} = \underset{\sim}{E} + \underset{\sim}{v}_p \wedge \underset{\sim}{B} \qquad 4.11$$

$$M_A \gamma u \frac{d\underset{\sim}{v}_e}{dx} = -\underset{\sim}{E} - \underset{\sim}{v}_e \wedge B \qquad 4.12$$

and

$$u\ \nabla \wedge \underset{\sim}{B} = \frac{M_A}{\gamma + \gamma^{-1}} (\underset{\sim}{v}_p - \underset{\sim}{v}_e) \qquad 4.13$$

where $\gamma^2 = m_p/m_E$ and M_A is the Alfvén Mach number, defined in terms of the Alfvén speed as $M_A = u/v_A$, and is based on the velocity of the plasma normal to the wave.

The frame of reference appropriate to equations 4.11 - 4.13 is shown in Figure 4.1.

In seeking solutions to the above set, an essential condition which must be maintained if the solutions are to remain valid is that the x-component of the plasma velocity does not change sign; this corresponds physically to the restriction that the particle trajectories do not loop back upon themselves. With this in mind, solutions are sought for which $u \to 1$, $b_y \to \sin\theta$ and $b_z \to 0$ at $x = -\infty$. By defining a dimensionless time as

$$u(x) = \frac{dx}{dt}$$

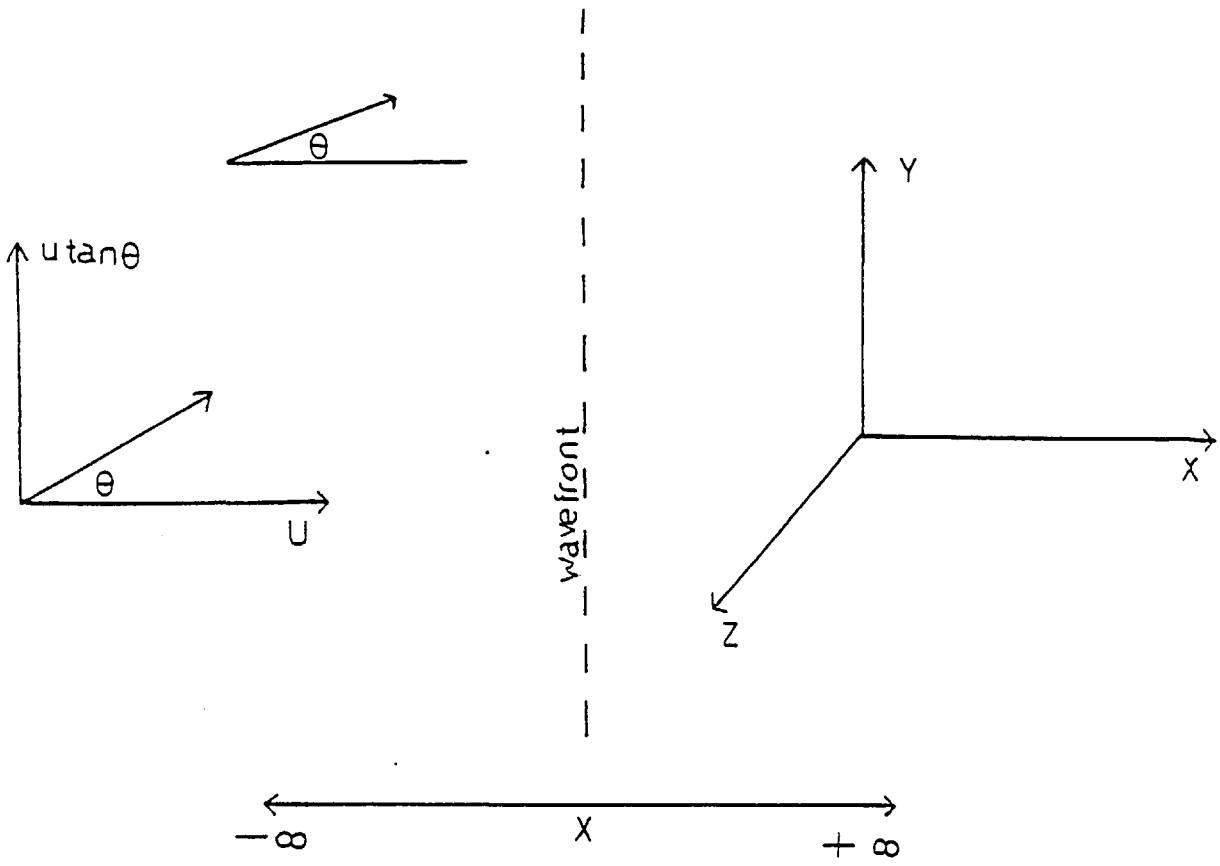

Figure 4.1 Frame of reference for equations 4.11 - 4.13.

and using t as the independent variable - Montgomery (1959); then upon adding the components of 4.11 and 4.12 and using 4.13, Saffman (1961) showed that the resulting equations possessed three first integrals, viz :

$$u + \tfrac{1}{2} M_A^{-2} (B_y^2 + B_z^2) = 1 + \tfrac{1}{2} M_A^{-2} \sin^2 \theta \qquad 4.14$$

$$\gamma^{-1} v_p + \gamma v_e - (\gamma+\gamma^{-1}) M_A^{-2} B_y \cos\theta = (\gamma+\gamma^{-1}) \operatorname{Tan} \theta \, (1-M_A^{-2} \cos^2\theta) \qquad 4.15$$

$$\gamma^{-1} w_p + \gamma w_e - (\gamma+\gamma^{-1}) M_A^{-2} B_z \cos \theta = 0 \qquad 4.16$$

To obtain the transverse velocity components v and w, equations 4.15 and 4.16 can be combined with equation 4.13 to obtain the velocities in terms of the magnetic field and its derivatives, i.e.

$$v_p = B_y M_a^{-2} \cos \theta - \gamma \frac{dB_z}{dt} M_A^{-1} + \operatorname{Tan} \theta \, (1 - M_A^{-2} \cos^2 \theta)$$

$$v_e = B_y M_A^{-2} \cos \theta + \gamma^{-1} \frac{dB_z}{dt} M_A^{-1} + \operatorname{Tan} \theta \, (1 - M_A^{-2} \cos^2 \theta)$$

$$w_p = B_z M_A^{-2} \cos \theta + \gamma \frac{dB_y}{dt} M_A^{-1}$$

$$w_e = B_z M_A^{-2} \cos \theta - \gamma^{-1} \frac{dB_y}{dt} M_A^{-1}$$

Substitution in equations 4.11 and 4.12 produces two second order differential equations for B_y and B_z, viz :

$$\frac{d^2B_y}{dt^2} + (\gamma^{-1}-\gamma) M_A^{-1} \frac{dB_z}{dt} \cos \theta - B_y (u-M_A^{-2} \cos^2\theta) = -\sin\theta(1-M_A^{-2} \cos^2\theta)$$

and

$$\frac{d^2B_z}{dt^2} + (\gamma^{-1}-\gamma) M_A^{-1} \frac{dB_y}{dt} \cos \theta - B_z (u - M_A^{-2} \cos^2 \theta) = 0$$

where u is given by euqation 4.14.

Thus, if the above two coupled equations can be solved for B_y and B_z, the transverse velocities v and w will follow.

Saffman (1961) showed that analytic rather than computational progress can be made if the above two equations are linearised in $B_y - \sin\theta = \phi_1$ and $B_z = \phi_2$ at a point near t, or $x = -\infty$. The equations obtained have the following form :

$$\frac{d^2\phi_1}{dt^2} + \lambda \frac{d\phi_2}{dt} - \mu \phi_1 = 0 \qquad 4.17$$

$$\frac{d^2\phi_2}{dt^2} - \lambda \frac{d\phi_1}{dt} - \upsilon \phi_2 = 0 \qquad 4.18$$

where $\lambda = (\gamma^{-1}-\gamma) M_A^{-1} \cos\theta$, $\mu = 1 - M_A^{-2}$ and $\upsilon = 1 - M_A^{-2}\cos^2\theta$. If solutions to 4.17 and 4.18 are sought for which ϕ_1 and ϕ_2 are proportional to e^{Pt} then 4.17 and 4.18 can be written as a quadratic in P^2,

$$P^2 + \mu\upsilon P^{-2} = \mu + \upsilon - \lambda^2 \qquad 4.19$$

equation 4.19 yields different solution depending upon the relative magnitudes of μ, υ and λ. These are summarised in Table 4.1.

In summary, the above equations represent infinitesimal, linear exponential waves which are propagating at an angle θ to the magnetic field in a cold collisionless plasma. From these, the conditions for solutions to exist which initially grow exponentially from a uniform state may be obtained. Essential conditions for the above solutions to be physically meaningful is that the solutions be bounded for all t, and that $u > 0$.

In view of the observational and theoretical evidence presented in Chapter 1 it seems clear that Mach numbers of interest correspond

TABLE 4.1 Solutions to Equation 4.19

Case	Parameter Magnitudes	Alfven Mach No.	Roots and Comments
1	$\upsilon > o > \mu$	$\cos\theta < M_A < 1$	2 real roots, one of each sign. Negative root violates boundary conditions at $t \to -\infty$, $\therefore$ one unique solution only (see later)
2	$\upsilon > \mu > o$	$M_A > 1$	2 positive roots if : $\mu + \upsilon - \lambda^2 > 2\sqrt{(\mu\upsilon)}$ and 2 complex if : $2\sqrt{(\mu\upsilon)} > \mu + \upsilon - \lambda^2 > 2\sqrt{\mu\upsilon}$ as 2 values of P still present, implies infinite number of solutions
3	$\mu = \upsilon > o$ ($\theta = o$)	$M_A > 1$	Complex roots with non-zero real part if $\mu > \lambda^2$ i.e. $M_A > \frac{1}{2}(\gamma^{-1}+\gamma)$ - otherwise imaginary
4	$\mu = o$	$M_A = 1$	One root = 0, the other is positive unique solution
5	$o > \upsilon > \mu$	$M_A < \cos\theta$	2 negative roots, $\therefore$ solution corresponds to all variables constant

to Case 1 i.e. $\cos\theta < M_A < 1$. Whether the solution is a soliton or a quasi shock it is physically significant providing the Alfvén Mach number lies within this range. It therefore seems feasible that the particular values of γ, M_A and θ determine whether a soliton or a quasi-shock is obtained, and it is unlikely that the solution will always be a solitary wave as successive perturbations are unlikely to return the particle to its original position - thus a quasi shock should be a common solution for this range of M_A.

From Chapter 3 the dispersion relation for oblique HM waves - as derived from linear theory - is :

$$\frac{W^2}{V_A^2} = M_A^2 = 1 - \tfrac{1}{2}\sin^2\theta \pm \{\tfrac{1}{4}\sin^4\theta + (\frac{\omega}{\Omega_p})^2\cos^2\theta\}^{\frac{1}{2}} - \frac{\omega^2}{\Omega_e\Omega_p} \qquad 4.20$$

where $W = \omega/k \equiv$ phase velocity.

In view of the theoretical arguments and the observational evidence presented in Chapter 1, we consider only the negative sign in equation 4.20, which corresponds to the shear mode wave and is just given by :

$$\frac{W^2}{V_A^2} = 1 - \tfrac{1}{2}\sin^2\theta - \{\tfrac{1}{4}\sin^4\theta + (\frac{\omega}{\Omega_p})^2\cos^2\theta\}^{\frac{1}{2}} - \frac{\omega^2}{\Omega_e\Omega_p}$$

or equivalently,

$$\omega^2 = K^2 V_A^2 [1 - \tfrac{1}{2}\sin^2\theta - \{\tfrac{1}{4}\sin^4\theta + (\frac{\omega}{\Omega_p})^2\cos^2\theta\}^{\frac{1}{2}} - \frac{\omega^2}{\Omega_e\Omega_p}]$$

As in the previous sub-section, to understand in a quantitative way how the solutions behave, it is desirable to use the equations in their dimensionless form, and the next section will give the details of this process.

4.3 The De-Dimensionalising Process

From the formulation in Chapter 3 the appropriate equations to be written in a dimensionless form are :

$$m_e\, u \frac{dv_e}{dx} = -e\,(E_y + w_e\, B_x - u\, B_z) \qquad 4.21$$

$$m_e\, u \frac{dw_e}{dx} = -e\,(u\, B_y - v_e\, B_x) \qquad 4.22$$

$$\frac{dB_y}{dx} = \mu_o\, n\, e\,(w_p - w_e) \qquad 4.23$$

$$\frac{dB_z}{dx} = -\mu_o\, n\, e\,(v_p - v_e) \qquad 4.24$$

Equations 4.21 through 4.24 are the four coupled differential equations from which v_e, w_e, B_y and B_z can be determined and may be used for either electrons or protons, one species being eliminated by use of the constants of the motion, viz. equations 3.20, 3.21 and 3.22.

The process to de-dimensionalise the equations is carried out with respect to a characteristic velocity, in this case the Alfvén velocity, and a characteristic length taken as c/ω_{pe} where ω_{pe} is the electron plasma frequency.

The normalised magnetic field B_o is defined by equation 4.25 as :

$$B_o = (B_{xo}^2 + B_{zo}^2)^{\frac{1}{2}} \qquad 4.25$$

and each field component is then given by : $b_x = B_x/B_o$, $b_y = B_y/B_o$, and $b_z = B_z/B_o$. Similarly, the dimensionsless velocities are given by $u = V_x/V_A$, $v = V_y/V_A$ and $w = V_z/V_A$ where V_A is the Alfvén speed in km s^{-1}.

An expression for u_x can be obtained by using equation 3.22, i.e. :

$$2\,\mu_o\,N\,u_{xo}\,(m_p + m_e)\,u_x + B_y^2 + B_z^2 = \mu_o\,2\,N\,(m_p + m_e)\,u_{xo}^2 + B_{zo}^2$$

where the parameters are as defined in Chapter 3. Then,

$$2\,\mu_o\,N\,u_{xo}\,(m_p + m_e)\,\{u_x - u_{xo}\} = B_{zo}^2 - B_y^2 - B_z^2$$

and using $b_y = B_y/B_o$ etc. we obtain

$$2\,\mu_o\,N\,u_{xo}\,(m_p + m_e)\,\{u_x - u_{xo}\} = B_o^2\,(b_{zo}^2 - b_z^2 - b_y^2)$$

As $u_x = u\,V_A$, and $V_A = \dfrac{B_o}{[\mu_o\,N\,(m_p + m_e)]^{\frac{1}{2}}}$ we then have

$$2\,u_{xo}\,(u_x - u_{xo}) = b_{zo}^2 - b_z^2 - b_y^2$$

$$\therefore\ u_x = u_{xo} + \frac{1}{2\,u_{xo}}\,(b_{zo}^2 - b_z^2 - b_y^2)$$

and noting that $u_{xo} \to M_A$ we obtain finally,

$$u_x = M_A + \frac{1}{2\,M_A}\,(b_{zo}^2 - b_z^2 - b_y^2) \qquad 4.26$$

However, for the equations involving differentials such as

$$\frac{d\,b_y}{dx} = \mu_o\,n\,e\,(w_p - w_e) \qquad 4.27$$

it is convenient to write

$$\frac{d}{d\tau} = u\frac{d}{dx}$$

and all differentials are then taken to be with respect to τ (Montgomery,

1959, Saffman 1961, and Kellogg, 1964). In this case, w_p can be eliminated. From equation 4.27 and equation 3.21 we obtain :

$$m_e w_e - m_p w_p = \frac{B_{xo}}{\mu_o N u_{xo}} (B_z - B_{zo})$$

and using $b_z = B_z/B_o$ etc. gives

$$m_e w_e - m_p w_p = \frac{B_o b_{xo} (b_z - b_{zo})}{\mu_o N u_{xo}}$$

Substituting for B_o from $V_A = \frac{B_o}{[\mu_o N (m_p + m_e)]^{\frac{1}{2}}}$ on the RHS and using $w' = \frac{w}{V_A}$ on the LHS gives, on dropping the primes :

$$m_e w_e - m_p w_p = \frac{[\mu_o N(m_p + m_e)]^{\frac{1}{2}} b_{xo} (b_z - b_{zo})}{\mu_o N u_{xo}}$$

hence w_p can be eliminated.

Applying the boundary condition $u_{xo} \to M_A$ and putting $\frac{dB_y}{dx} = B_o \frac{db_y}{d\tau}$ the dimensionless form for b_y becomes

$$\frac{db_y}{d\tau} = \gamma^{-\frac{1}{2}} \{ M_A w_e + b_{xo} (b_z - b_{zo}) \} \qquad 4.28$$

where $\gamma^2 = m_p/m_e$. And in what follows v and w are in their dimensionless form, and refer to the electron component.

An identical process applied to equation 4.24, but this time making use of equation 3.20, gives

$$\frac{db_z}{d\tau} = \gamma^{-\frac{1}{2}} (M_A v_e - b_{xo} b_y) \qquad 4.29$$

and for equations 4.21 and 4.22 we obtain

$$\frac{dv}{d\tau} = \gamma^{\frac{1}{2}} \left(-M_A\, b_{zo} + u_x\, b_z - w\, b_{xo}\right) \qquad 4.30$$

$$\frac{dw}{d\tau} = \gamma^{\frac{1}{2}} \left(-u_x\, b_y + v\, b_{xo}\right) \qquad 4.31$$

The above set of equations along with equation 4.26 form the de-dimensionalised coupled equations which describe the behaviour of the various parameters which are of interest, and they are solved on the assumption that all the parameters approach their equilibrium values at a point far ahead of the wave, i.e. as $x \to -\infty$.

4.4 Characteristics of the Modes

In order to proceed with a numerical integration it is first necessary to obtain starting values for the various parameters; with these values as input and an appropriate time step, the equations can then be solved on a step by step basis. While these starting values could be found by trial and error the method used in this case was to make use of the results of the linear theory done in Chapter 3. However, information on the characteristics of the modes which can be obtained may be found by perturbing equation 4.28 through 4.31. To achieve this the assumption is made that the parameters consist of their equilibrium value, plus a small perturbation which behaves as $e^{\sigma\tau}$, and σ should have a positive non-zero real part. On this assumption equations 4.28 through 4.31 become :

$$\sigma\, v = \gamma^{\frac{1}{2}} \left\{\left(M_A - \frac{b_{zo}^2}{M_A}\right) \left(b_z - b_{zo}\right) - w\, b_{xo}\right\} \qquad 4.32$$

$$\sigma\, w = \gamma^{\frac{1}{2}} \left\{-M_A\, b_y + v\, b_{xo}\right\} \qquad 4.33$$

$$\sigma\, b_y = \gamma^{-\frac{1}{2}} \left\{M_a w + b_{xo} \left(b_z - b_{zo}\right)\right\} \qquad 4.34$$

$$\sigma\, b_z = \gamma^{-\frac{1}{2}} \{M_A\, v - b_y\, b_{xo}\}$$

and for non-zero solutions, the determinant of the above set must equal zero i.e. :

$$\sigma^4 + \sigma^2 [b_{xo}^2 (\gamma+\gamma^{-1}) + b_{zo}^2 - 2M_A^2] + (M_A^2-1)(M_a^2-b_{xo}^2) = 0 \qquad 4.36$$

Letting $A = [b_{xo}^2 (\gamma+\gamma^{-1}) + b_{zo}^2 - 2M_A^2]$

and $B = (M_A^2 - 1)(M_A^2 - b_{xo}^2)$

this condition becomes :

$$\sigma^4 + A\,\sigma^2 + B = 0$$

$$\therefore \quad \sigma^2 = \tfrac{1}{2}\{-A \pm (A^2 - 4B)^{\frac{1}{2}}\} \qquad 4.37$$

Thus there is a whole spectrum from which to choose σ.

The domains for roots of different types are similar to those enumerated by Kellogg (1964) and Tidman and Krall (1971) for the zero-temperature soliton problem. In this context it is useful to generalise slightly Kellogg's notation in describing the characteristics of the various roots, and the following table can be constructed for the solutions to equation 4.35 (Table 4.2).

			Roots with $R_e(\sigma) > 0$	Designation in Fig.2
$B < 0$			$\sigma_R, \pm i\sigma_i$	1R
$B > 0$	$A^2 - 4B < 0$		$\sigma_R, \pm i\sigma_i$	2C
$B > 0$	$A^2 - 4B > 0$	$A < 0$	σ_{1R}, σ_{2R}	2R
$B > 0$	$A^2 - 4B > 0$	$A > 0$	$\pm i\sigma_{1i}, \pm i\sigma_{2i}$	4I

TABLE 4.2 Solutions to Eqn 4.35

In Table 4.2 the following notation applies :

1R ≡ 1 real root

2C ≡ 2 complex roots

2R ≡ 2 real roots

4I ≡ 4 imaginary roots

It is an advantage to display the tabulated data in a figure of b_{z_1} against b_x, where :

$$b_{z_1} \equiv \sin\theta/M_A, \text{ and } b_x \equiv \frac{\cos\theta}{M_A}$$

but first the boundaries of the various regions must be found.

a) The boundaries of region 1R occur when B changes sign, i.e. when B = 0, where from equation 4.25, i.e. $B_o^2 = (B_{xo}^2 + B_{zo})^{\frac{1}{2}}$ we have upon using $b_{xo}^2 = B_{xo}^2/B_o^2$ etc.

$$b_{xo}^2 + b_{zo}^2 = 1 \qquad 4.37$$

hence, when $b_{zo}^2 \to 0$, $b_{xo}^2 \to 1$ and vice-versa.

b) The boundary of 2C is given by equating $A - 4B = 0$, i.e.

$$b_{xo}^4 (\gamma+\gamma^{-1}) + b_{zo}^4 + 2b_{xo}^2 (b_{zo}^2-2)\{\gamma^{\frac{1}{2}}-\gamma^{-\frac{1}{2}}\}^2 = 0$$

when $b_{zo} = 0$, we have

$$b_{xo} = \frac{4\gamma}{(1+\gamma)^2} \text{ or } b_{xo} = 0.$$

c) The boundaries of regions 2C and iR have one point in common when B = 0 and A = 0, i.e.

$$b_x^2 = \frac{\gamma}{\gamma^2-\gamma+1}, \quad b_{zo}^2 = \frac{(\gamma-1)^2}{\gamma^2-\gamma+1}$$

Since A goes through zero at this point it is also a boundary between regions 2R and 4I.

A plot of the various solutions can now be made and is shown in Figure 4.2. In this diagram it is taken that fields depart from their upstream values at the leading edge of the "shock" as $e^{\sigma\tau}$, where $\tau = x\ \omega_{pe}/c$

From Figure 4.2 it can be seen that the character of the waves depends on whether the parameters upstream from the shock lie in region 1R, 2R, 2C or 4I, in which σ can have one real, two real, two complex or all four roots imaginary. However, a clear distinction is that in region 2 all velocities are greater than the Alfvén speed, V_A, while in region 1 they are less.

Thus from the evidence of Chapter 1, in which it was shown that the Alfvén Mach number $M_A << 1$, (or $u << V_A$), it is region 1 which is of particular interest in this work.

In regions 4I and 1R there exist pure imaginary roots to equation 4.35. These correspond to waves which do not grow in amplitude from one oscillation to the next since σ does not have a real part. Many authors in the past have adopted the process of excluding the imaginary roots and while this is of small consequence in region 1R - as there is still one real root present which can produce non-linear waves, in region 4I <u>all</u> the roots are imaginary and to exclude this region is to exclude many oblique waves of interest.

In considering this region it is necessary to modify slightly the assumptions of the plasma state at $x = -\infty$, i.e. the upstream conditions must be modified to include small amplitude linear oscillations about their zero order values. In addition to this, means must be found to enable the waves to grow non-linearly. A way of achieving this is to allow for a small amount of dissipation at $x = -\infty$; if the linearised equations are then modified to include a term which has its origin in the microturbulence inside the wave, it is found

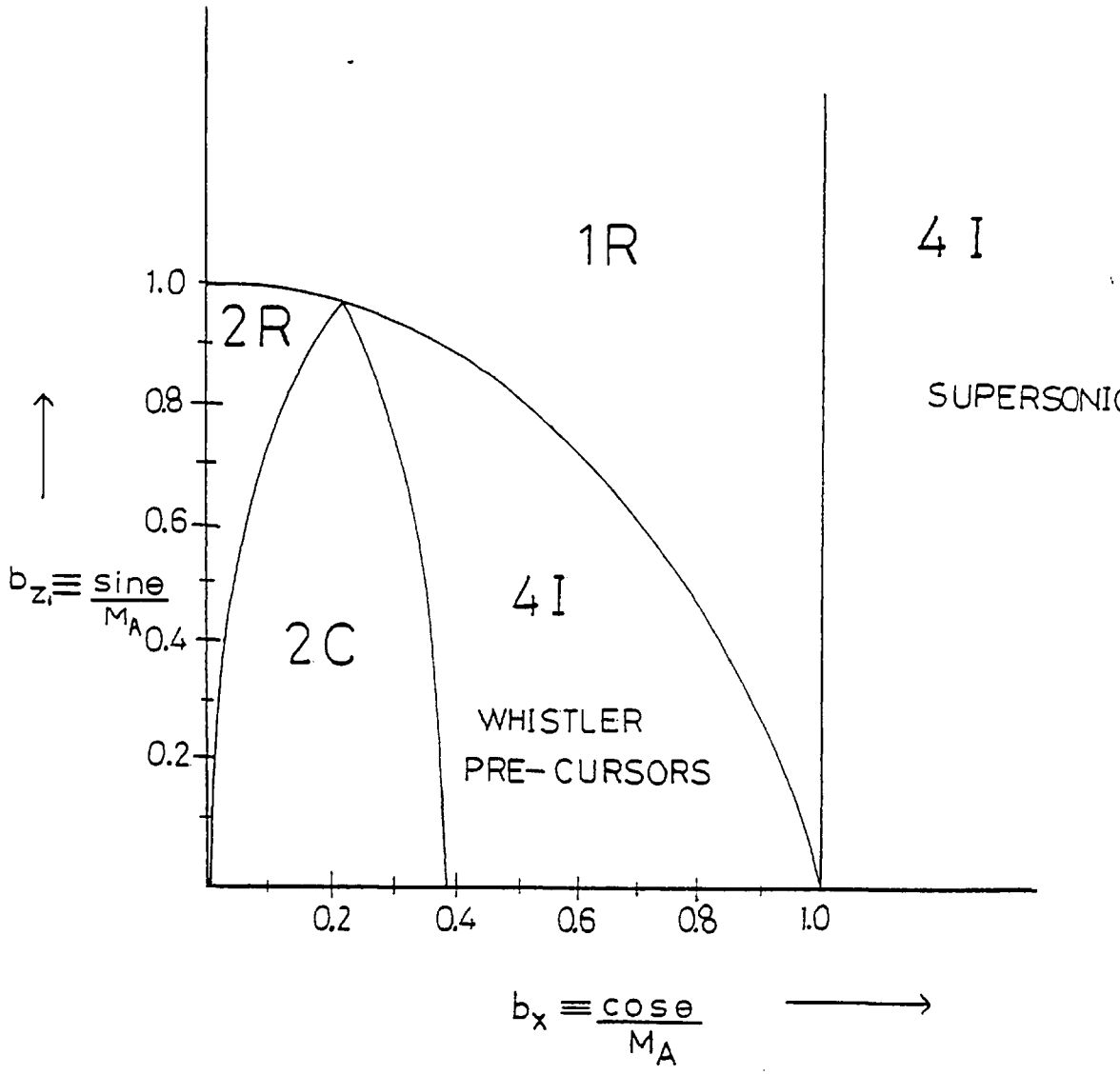

Figure 4.2 Plot of the regions represented by the Table 2 data.

that the large wavenumber root in region 4I will damp out as τ increases positively.

However, at high enough Mach numbers the small wavenumber root also grows, and in this case only the lower of the two wavenumbers would be of physical interest. These solutions correspond in fact to precursor wave effects, and the shock solutions which occur in region 4I afford an explanation of the whistler precursors.

To conclude this section, it should be mentioned briefly that an analogy can be drawn between the equations which govern the motion of particles in the above analysis, and those which control the motion of particles moving in a potential field of force which has a uniform magnetic field perpendicular to the plane of motion. This analogy has been discussed by several authors in the past, and no further mention will be made here (Saffman, 1961; Cordey and Saffman, 1966; Dixon and Woods, 1975). However the nature of this problem enables further progress to be made analytically, and further simplifications can be made which also help to illuminate the problem. From the first chapter we know that the range of values for the Alfvén Mach number are less than one, (i.e. $M_A << 1$), or equivalently, the speed u, is very much less than the Alfvén speed, (i.e. $u << V_A$). The next sub-section gives the form of the equations under the above conditions.

4.5 The Case for $u << V_A$

Equation 4.36, viz.

$$\sigma^4 + \sigma^2 \left[b_{xo}^2 (\gamma+\gamma^{-1}) + b_{zo}^2 - 2M_A^2\right] + (M_A^2-1)(M_A^2-b_{xo}^2) = 0$$

implies that for the case $u << V_A$, or equivalently $M_A << 1$; then under these circumstances the roots are well separated and can be approximated too by the following pair of equations :

$$\sigma^2 = -b_{xo}^2\,\gamma + b_{zo}^2, \quad \text{and} \quad \sigma^2 = \frac{(1-M_A^2)(M_A^2-b_{xo}^2)}{\gamma b_{xo}^2 + b_{zo}^2}$$

where $b_{zo} = \sin\theta \approx 1$.

There are therefore two kinds of solution, one oscillatory with short wavelength and the other, real exponential and slowly changing. The presence of the rapid oscillation makes a computation for the Alfvén mode difficult, Kellogg (1964), as for a realistic value of γ the integration step size must be chosen so as to be small compared to the oscillation otherwise the accuracy of the computation will suffer, while the actual distance over which the equations must be integrated is determined by the slowly changing real exponential; however despite this complication and approximation to the Alfvén mode can be found which enables computational progress to be made, and this will form the subject of the next sub-section : but it can be seen that the second of the two solutions is always positive, providing $(M_A^2-1)(M_A^2-b_{xo}^2) > 0$ that is there is always one real root, and it is this solution which gives the behaviour at large, negative τ.

4.6 Approximation to the Alfvén Mode

Considering equations 4.28 through 4.31, it can be seen that they are of fourth order overall, and to approximate to the Alfvén mode it is necessary to reduce this order by two; that is we require to drop two of the differentials to ensure that

$$\left(\frac{d}{d\tau}\right)^4 \qquad \left(\frac{d}{d\tau}\right)^2$$

and the choice of which pair to ignore depends strictly on the mode which we require to model - in this case the shear mode, which in turn is characterised by the polarisation. A good contender for the

Alfvén mode is the equation involving $\frac{db_z}{d\tau}$, i.e. equation 4.35, we therefore start by ignoring the left hand side of 4.35 and examine the consequences : on doing this we obtain

$$v = \frac{b_{xo}\, b_y}{M_A}$$

and upon substitution in equation 4.33 we have,

$$\sigma w = \gamma^{\frac{1}{2}} \left(b_{xo} - \frac{M_A^2}{b_{xo}}\right) v \qquad 4.47$$

However in sub-section 4.5 it was shown that for the case $u << V_A$ a real exponential root was obtained which has the form :

$$\sigma^2 = \frac{(1 - M_A^2)\ (M_A^2 - b_{xo}^2)}{\gamma b_{xo}^2 + b_{zo}^2}$$

which for $M_A << 1$ is approximately

$$\sigma^2 \approx \frac{(M_A^2 - b_{xo}^2)}{\gamma b_{xo}^2}$$

or $$\frac{\sigma^2}{\gamma} \approx \frac{(M_A^2 - b_{xo}^2)}{\gamma^2\, b_{xo}^2} \qquad 4.48$$

However, from 4.47 we have :

$$\frac{\sigma^2}{\gamma} = \frac{\sigma v}{\gamma^{\frac{1}{2}} w b_{xo}} \{b_{xo}^2 - M_A^2\} \qquad 4.49$$

hence from equation 4.48 and 4.49 we find

$$\frac{\sigma v}{\gamma^{\frac{1}{2}} w b_{xo}} = -(\gamma b_{xo})^{-2} \qquad 4.50$$

This equation shows that providing $(\gamma b_{xo})^2 >> 1$, then σv (equation 4.32), and hence $\frac{dv}{d\tau}$ (equation 4.30) can be dropped. It therefore seems that the Alfvén mode can be approximated to by dropping the differentials $\frac{db_z}{d\tau}$ and $\frac{dv}{d\tau}$ in equations 4.29 and 4.30 respectively, however, the criteria for neglecting $db_z/d\tau$ may be seen from equation 4.32 as neglecting the σV term on the left hand side enables the equation to be written in the following form :

$$(b_{zo}^2 - M_A^2)\ (b_z - b_{zo}) \ = \ -M_A\ wb_{xo}$$

and because $M_A << 1$, and $b_{zo} \approx 1$ the term in $(b_{zo}^2 - M_A^2) \approx 1$, therefore we can write

$$b_z - b_{zo} \ \approx \ - M_A\ wb_{xo}$$

and upon using equation 4.50 for w we obtain finally :

$$b_z - b_{zo} \ = \ M_A\ b_{xo}^2\ \gamma^{3/2}\ \sigma\ v$$

If this is now used in equation 4.35 we find that in order to justify the dropping of the differential $db_z/d\tau$ we require that the following inequality be satisfied :

$$\sigma << \frac{1}{(\gamma\ b_{xo})} \qquad 4.51$$

Equation 4.51 shows that the approximation will only be valid providing σ is restricted to values very much less than unity which will clearly be the case as reference to the real, exponential σ root, viz.

$$\sigma^2 = \frac{(1 - M_A^2)\ (M_A^2 - b_{xo}^2)}{\gamma\ b_{xo}^2 + b_{zo}^2}$$

shows.

Finally, these approximations have been used in the computation, and providing equations 4.50 and 4.51 are satisfied, and the validity of this assumption should be tested for different regions of the computation, for example the linear and non-linear regime, then the Alfvén mode may be reasonably approximated to by neglecting the two differentials $db_z/d\tau$ and $dv/d\tau$.

4.7 Summary

The six sub-section of this chapter have concerned themselves with the process of verifying that shock-like solutions to the equations exist for Alfvén Mach numbers which are less than unity, and essentially summarises earlier work. Other sections are concerned with discussing the characteristics of the various modes, and the final sections detail the approximations which are required to suppress unwanted oscillatory solutions and compute only the Alfvén mode.

The next chapter deals with the results of these computations, and makes an exploratory investigation of magnetometer data from the ISEE-1 and 2 spacecraft.

CHAPTER 5

SOME RESULTS AND OBSERVATIONS

5.1 Preliminaries

In this chapter attention is given to the results of computing equations 4.26 through 4.31, and some simple features which were discovered are discussed in terms of physical processes. The results are then compared to spacecraft magnetometer data for representative crossings of the plasma sheet and events are shown which illustrate similarities.

The software written to solve the equations employs an Euler algorithm which is essentially a one-step method in that values of the function are calculated one at a time, and these values are then used in the calculation of later values.

In general the problem is of the following form :

$$y(x_{k+1}) = y(x_k) + \int_{x_k}^{x_{k+1}} y'(x)\, dx \qquad 5.1$$

and Euler's method is then the means of approximating the integral in equation 5.1. Therefore, if the behaviour of $y'(x)$ in the interval (x_k, x_{k+1}) can be predicted, the exact value of $y(x_{k+1})$ may be obtained. Assuming $y'(x)$ is continuous, the mean value theorem states that :

$$y'(\varepsilon) = \frac{y(x_{k+1}) - y(x_k)}{x_{k+1} - x_k} \qquad 5.2$$

where $x_k \leq \varepsilon \leq x_{k+1}$.

Re-arranging equation 5.2 for $y(x_{k+1})$ gives

$$y(x_{k+1}) = y(x_k) + y'(\varepsilon)\ (x_{k+1} - x_k) \qquad 5.3$$

and if this equation is compared with equation 5.1 we have :

$$y'(\varepsilon)\ (x_{k+1} - x_k) = \int_{x_k}^{x_{k+1}} y'(x)\ dx \qquad 5.4$$

and equation 5.3 shows that the integral of a function over an interval is identical to the interval length multiplied by the value of the function at some point in the interval. The success of a method therefore depends on obtaining an approximate average derivative to use in place of the $y'(\varepsilon)$ term in equation 5.3; and the approximation used in the Euler method is to use the value of the derivative at the starting point of the interval. Thus if we write $h = x_{k+1} - x_k$ in equation 5.3 we have

$$y(x_{k+1}) = y(x_k) + h\ y'(x_k)$$

and upon writing $y(x_i) = y_i$, and substituting for y' we obtain finally the Euler algorithm, viz.

$$y_{k+1} = y_k + h\ f\ (x_k, y_k) \qquad 5.5$$

Equation 5.5 is straightforward and simple to use. It is particularly useful in the context of this work as the problem is essentially "one point", in that given suitable starting values solutions can be generated by repeated application of equation 5.5.

However, the algorithm is not without errors, and a full discussion of this is given in Appendix 1, but there can also be

hidden difficulties associated with the type of computer being used, for example, if h = 0.0001 then it cannot be represented exactly in a binary system, thus after sufficient steps, a significant error can be accumulated in the independent variable. Similarly, if the interval size is small the amount added to the ordinate at each step may be very small when compared to the ordinate itself; however, all of these errors are likely to be small when compared to any truncation error which may be present; and this point is discussed in the Appendix.

5.2 Results

From the linear theory done in Chapter 3, it may be expected that when the equations are computed they will initially show exponential growth from a uniform state, and that this will continue until non-linear effects become important. That this is the case may be seen from Figure 5.1. This figure corresponds to a cos θ value of 0.009 (θ = 89.484°), and it suggests that the non-linear effects constrain the perturbation in the y-component of the magnetic field to increase steadily.

Further examples of this effect are shown in Figures 5.2 through 5.5, and the range of parameters used in the computations are given in Table 5.1. These plots show that for a wide range of parameter space the solutions initially obey linear predictions, however, when non-linear terms become important they appear as a straight line increase in the $\underset{\sim}{B}_y$ perturbation, the sign of which is crucial in determining the character of the non-linear behaviour.

The interpretation of this may be through of in terms of constant current, whereby the effect of the wave field accelerates electrons steadily in the field-aligned direction, thereby producing

Figure Number	cos θ	w(1)	$B_{\sim y}(1)$	$B_{\sim z}(1)$	u(1)	ΔT
5.1	0.009	-0.0023	0.000199	1.000000	0.00998	3.0
5.2	0.0095	-0.001895	0.0000948	1.000000	0.009982	6.0
5.3	0.0099	-0.001818	0.0000909	1.000000	0.00994	6.0
5.4	0.00995	-0.00996	0.0000901	1.000000	0.009982	20.0
5.5	0.00892	-0.00231	0.000197	0.999999	0.00997	3.0

TABLE 5.1 Showing parameter space examined for Figures 5.1 - 5.5

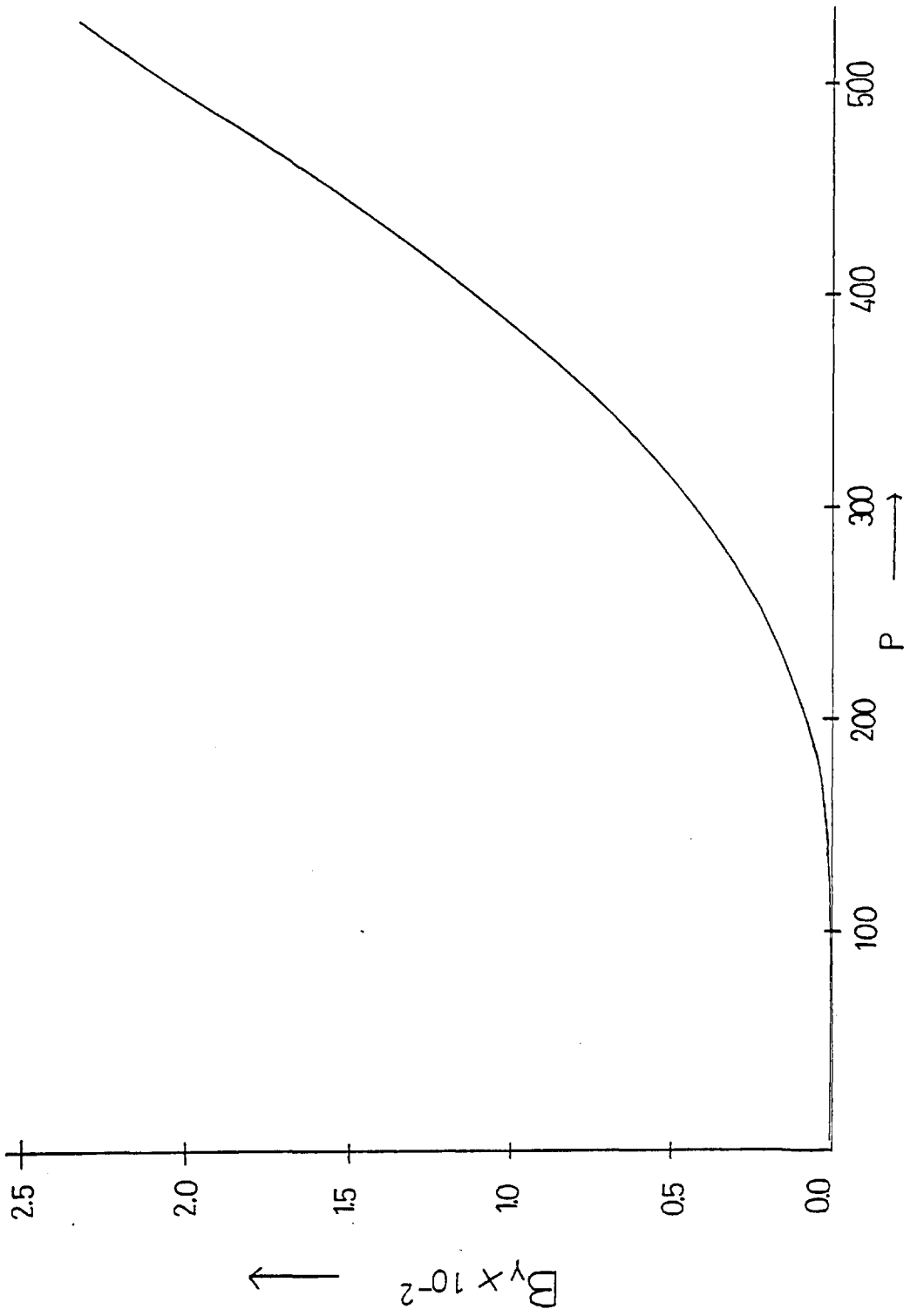

Figure 5.1 Plot of the B_y component against the 'P' parameter, which is a function of the plasma wavelength $c/\omega p_e$

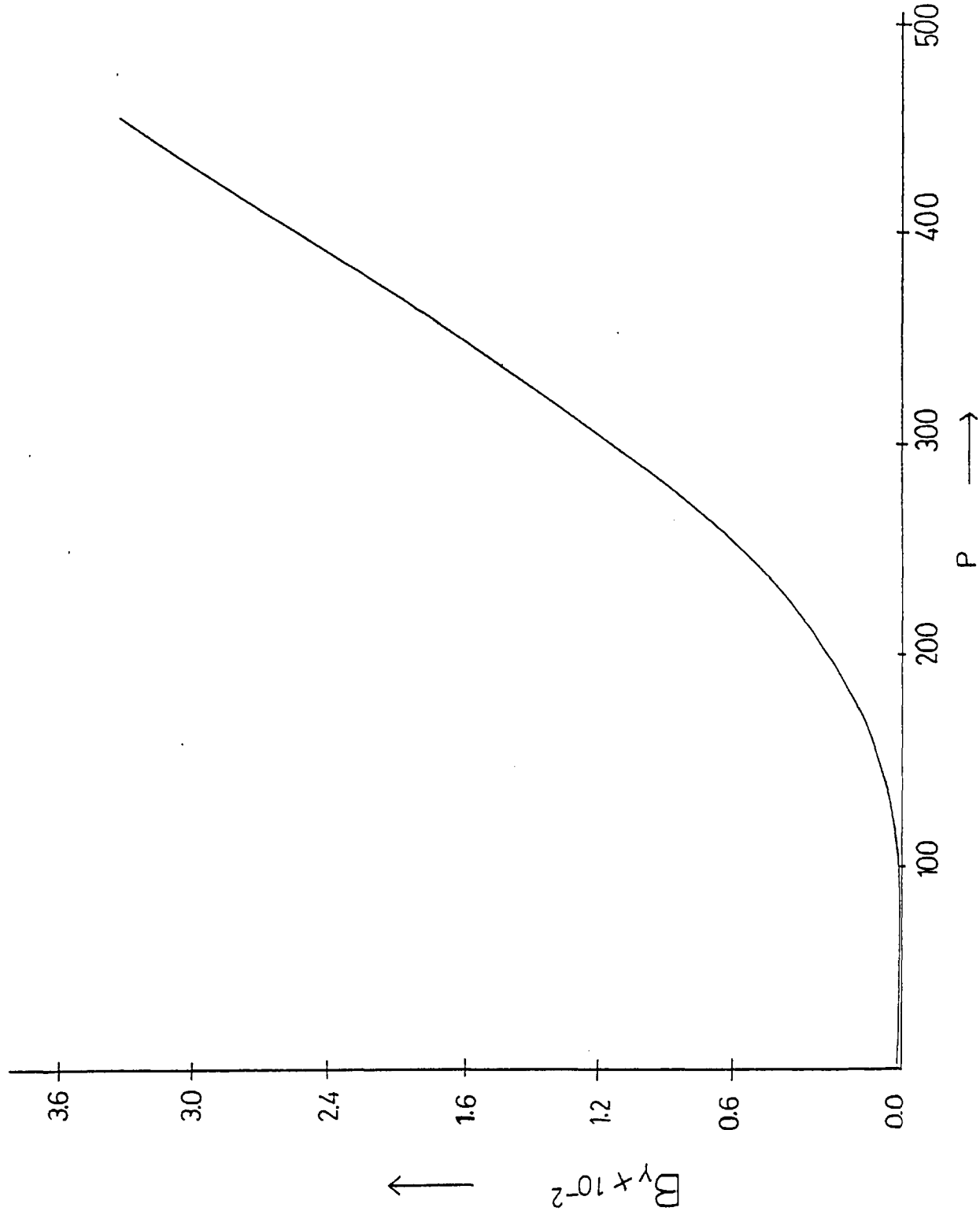

Figure 5.2 As for Figure 5.1 but refer to Table 3.

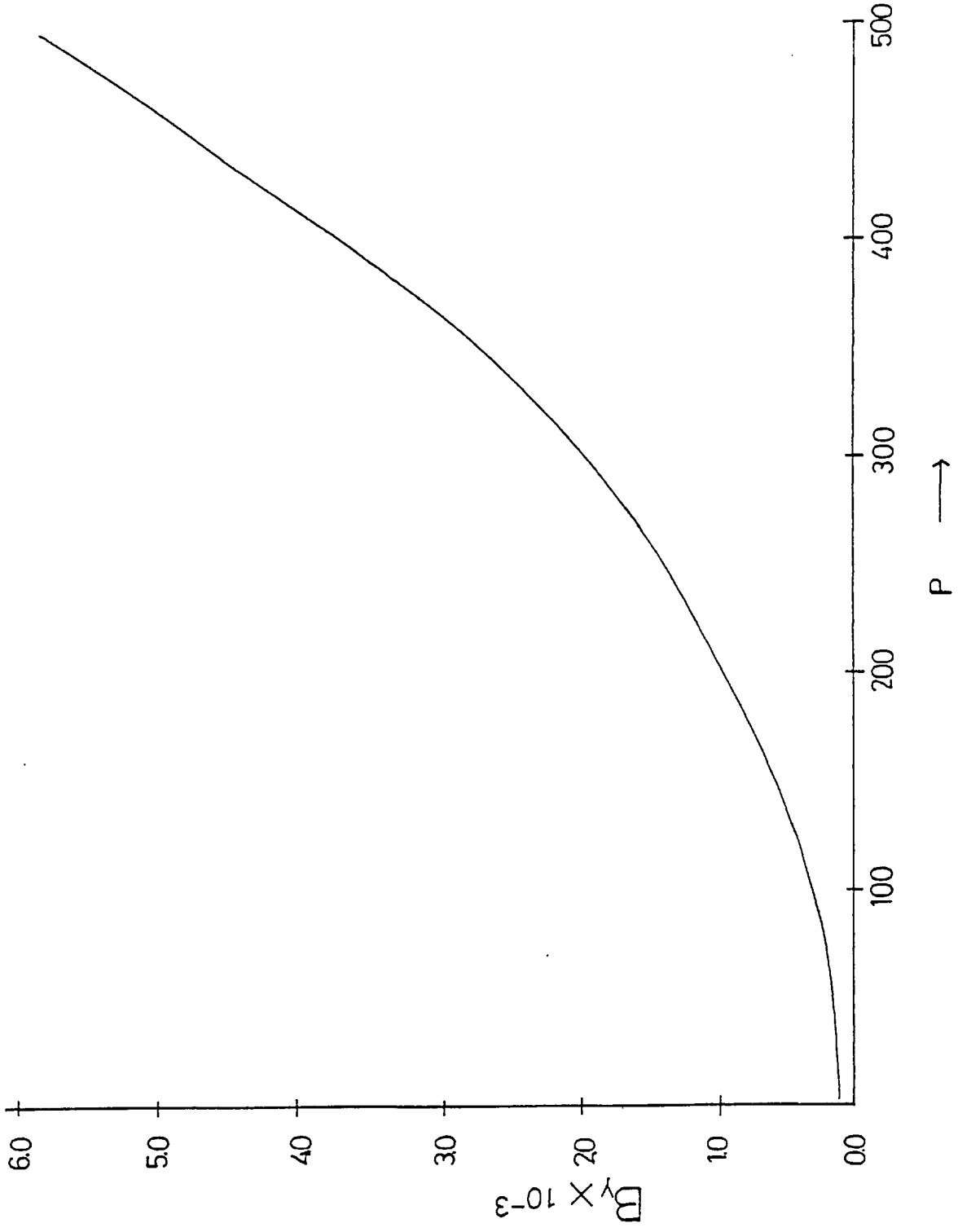

Figure 5.3 As for Figure 5.1

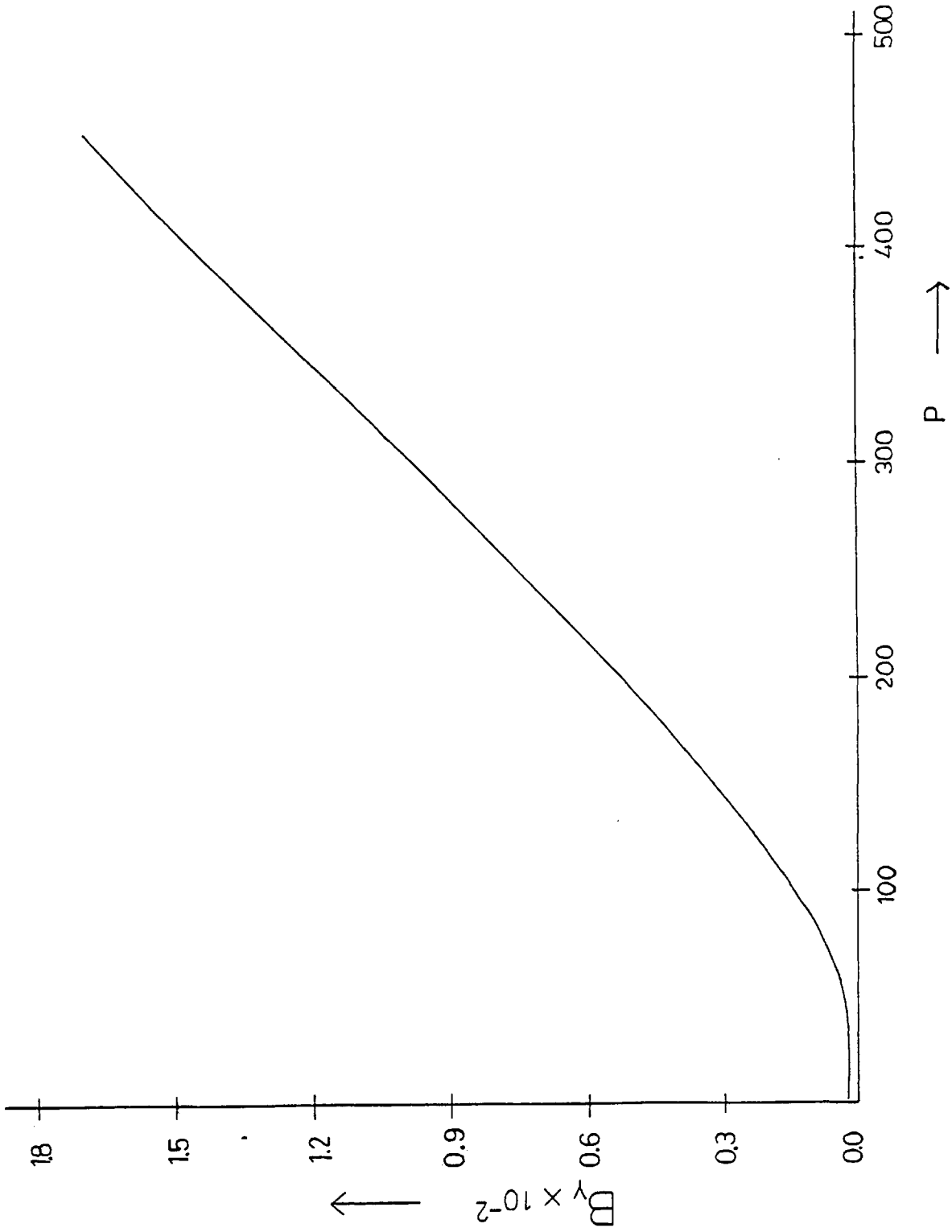

Figure 5.4 As for Figure 5.1

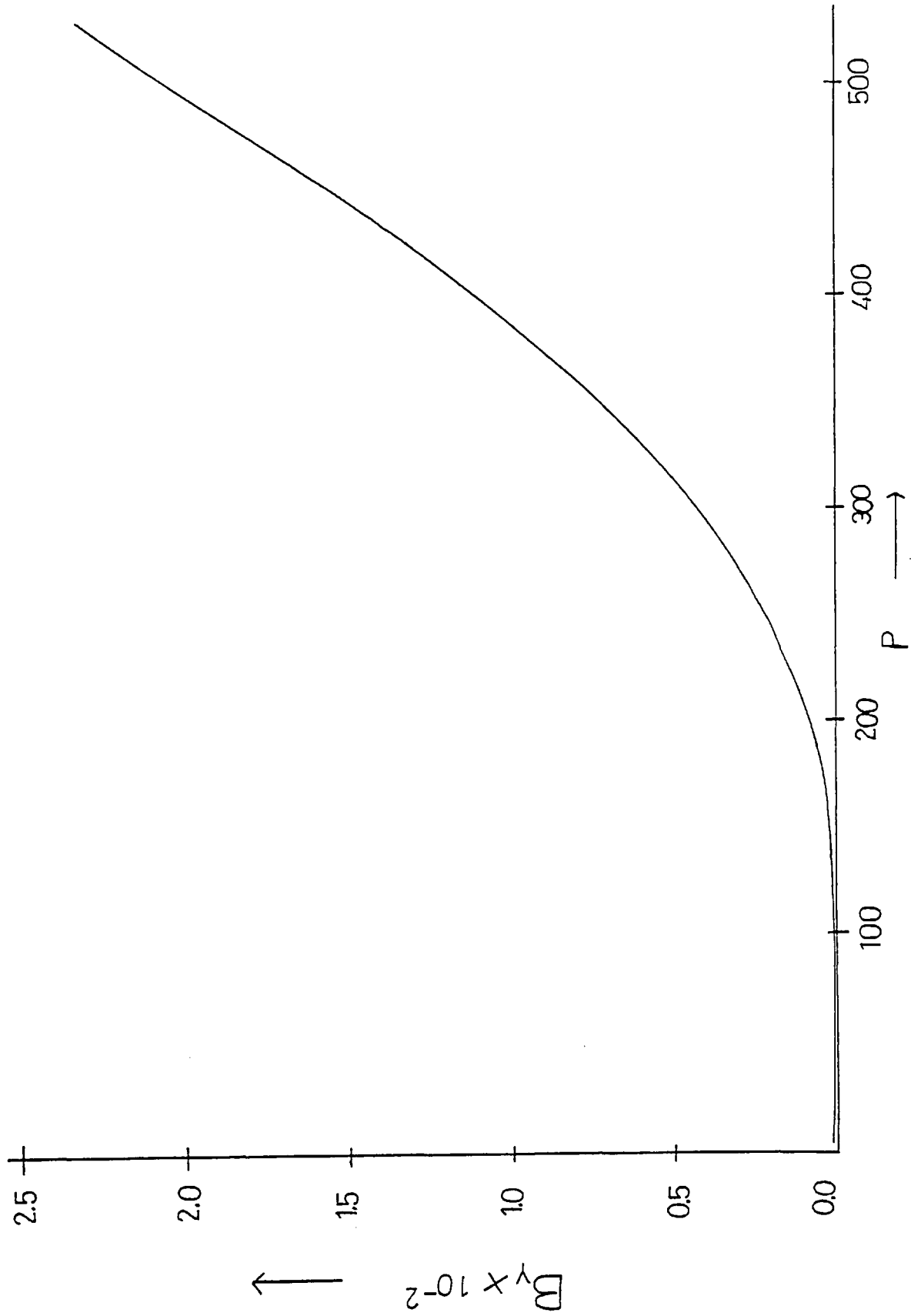

Figure 5.5 As for Figure 5.1

the current which is necessary to describe the behaviour of the $\underset{\sim}{B}_y$ component. The direction of particle flow is towards the earth, the current therefore flows tailwards.

An obvious consequence of this field-aligned acceleration would be a substantial increase in the field-aligned velocity, and Figures 5.6 through 5.10 show the corresponding velocity plots for the Table 5.1 events. All these plots show essentially the same type of behaviour, namely that as the magnetic field perturbation increases, the field aligned velocity increases accordingly and in the case of Figures 5.6, 5.7 and 5.10 we see at least a two order of magnitude increase.

It can also be seen that as cos θ approaches 0.0099, and particularly at higher values, the maximum value of velocity achieved is substantially reduced, and this corresponds to an order of magnitude reduction in the growth rate. An important point to note from Figures 5.1 through 5.5 is that the rate of growth of the exponential region varies : that this is primarily a function of the angle θ may be seen by recalling equation 3.46, which stated :

$$\frac{\sigma^2}{\Omega^2_p} = \frac{u^2/V_A^2 - \cos^2\theta}{2\cos^2\theta + 1/1800}$$

and which was shown to be almost equivalent to $\sigma \approx (M_A^2 - \cos^2\theta)^{\frac{1}{2}}$... (equation 3.47). Computationally, this dependence is best shown by holding all parameters except the angle constant, and this has been done for the set of starting values which correspond to Fig.5.1 (cf. Table 5.1). Figures 5.11 and 5.12 show the results of computing for cos θ = 0.007 and 0.0009 respectively. It can be seen from these plots that the values of the $\underset{\sim}{B}_y$ perturbation are an order of magnitude greater in the case of Fig.5.12 than the corresponding Fig.5.11. As

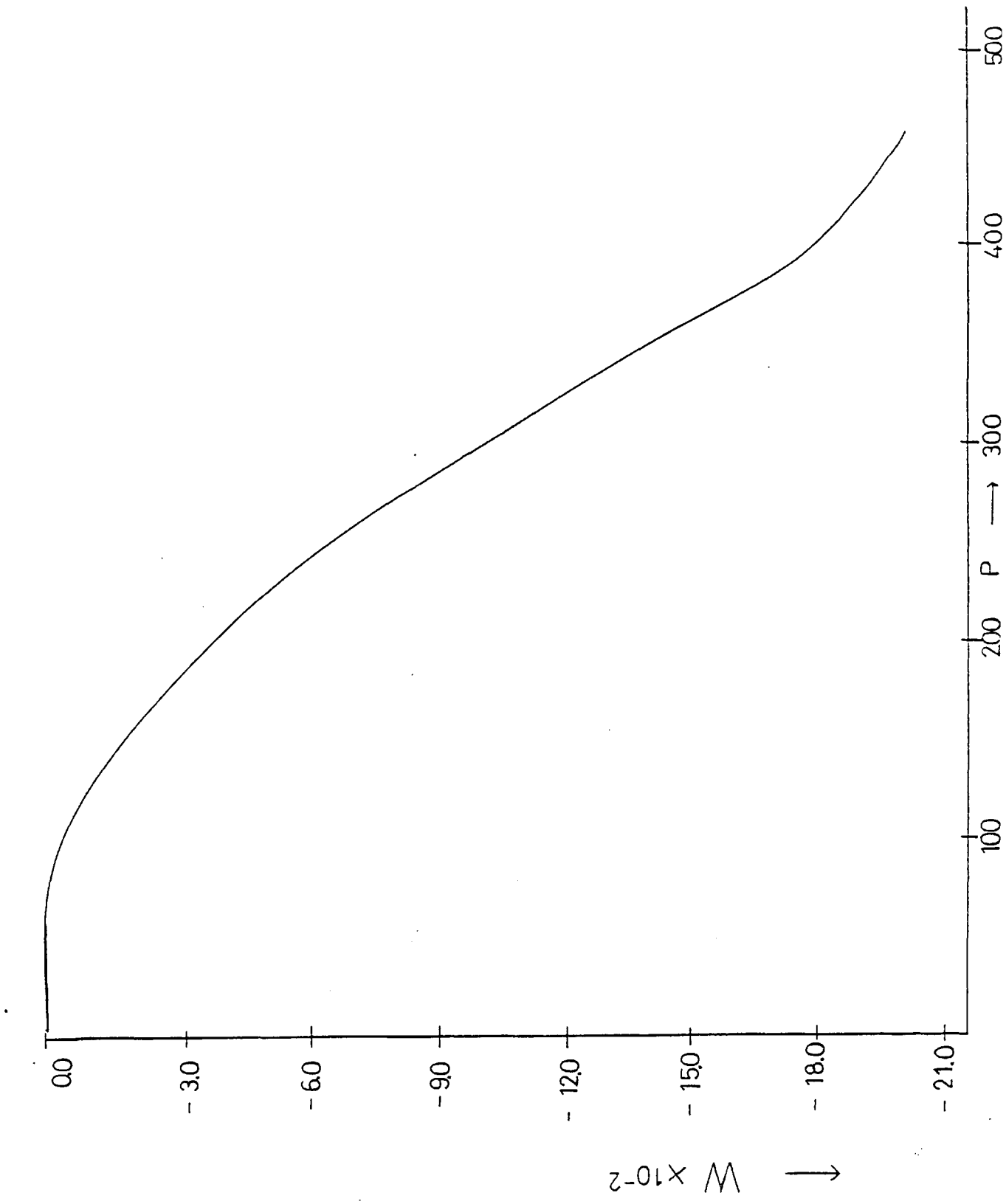

Figure 5.6 Plot of the fleid-aligned velocity against P for the Figure 5.1 case.

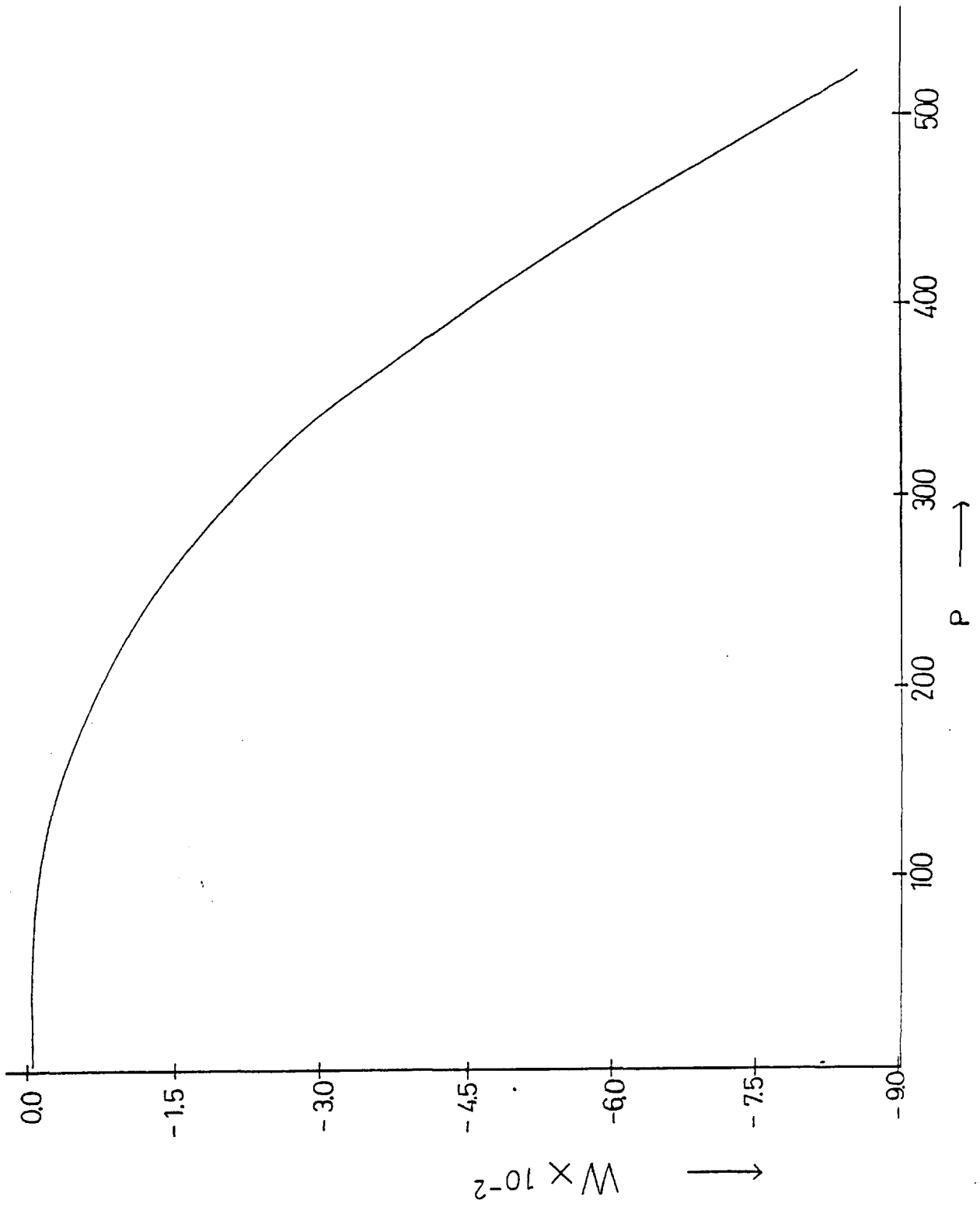

Figure 5.7 w plot, for Figure 5.2.

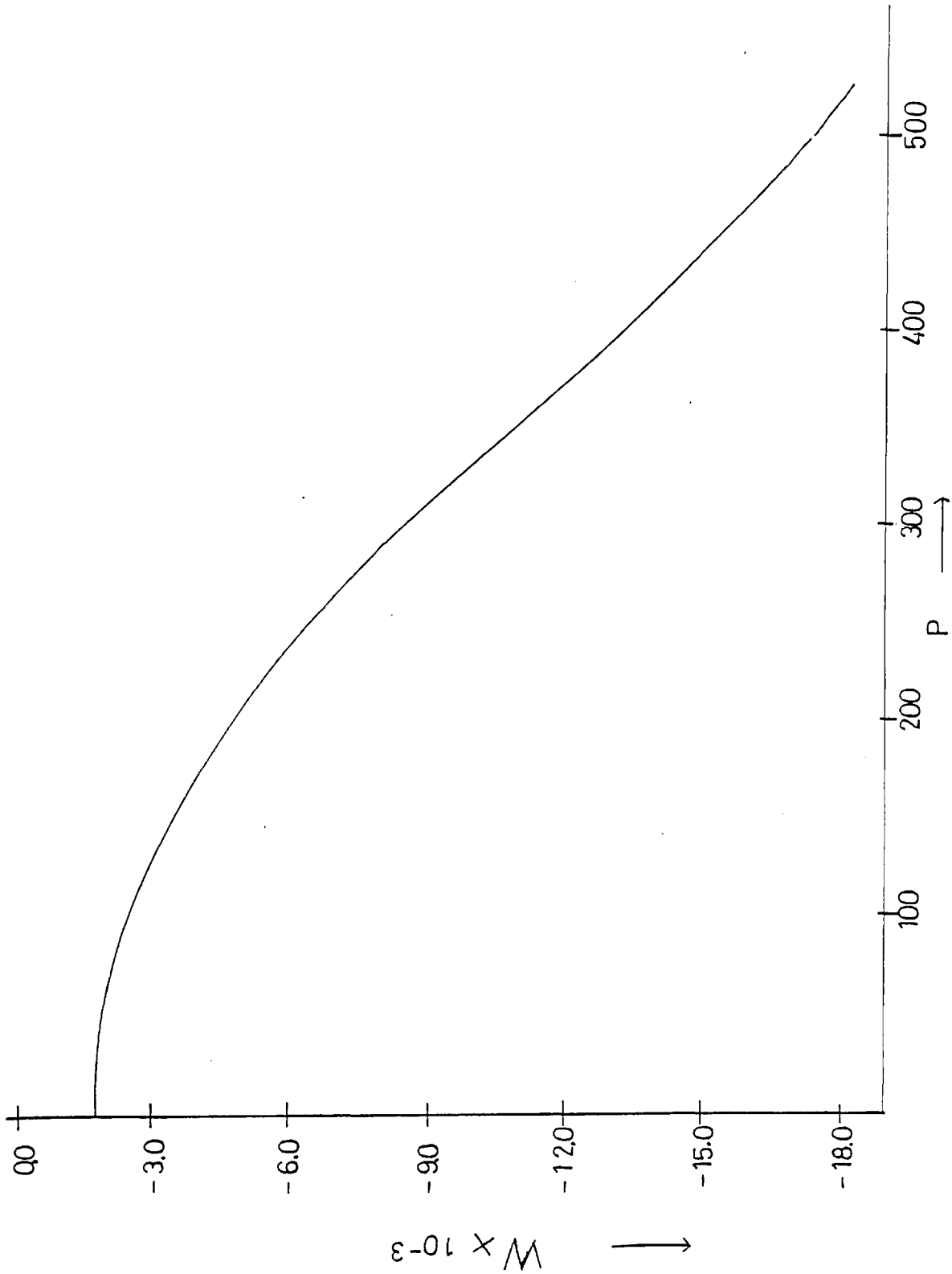

Figure 5.8 w plot, for Figure 5.3.

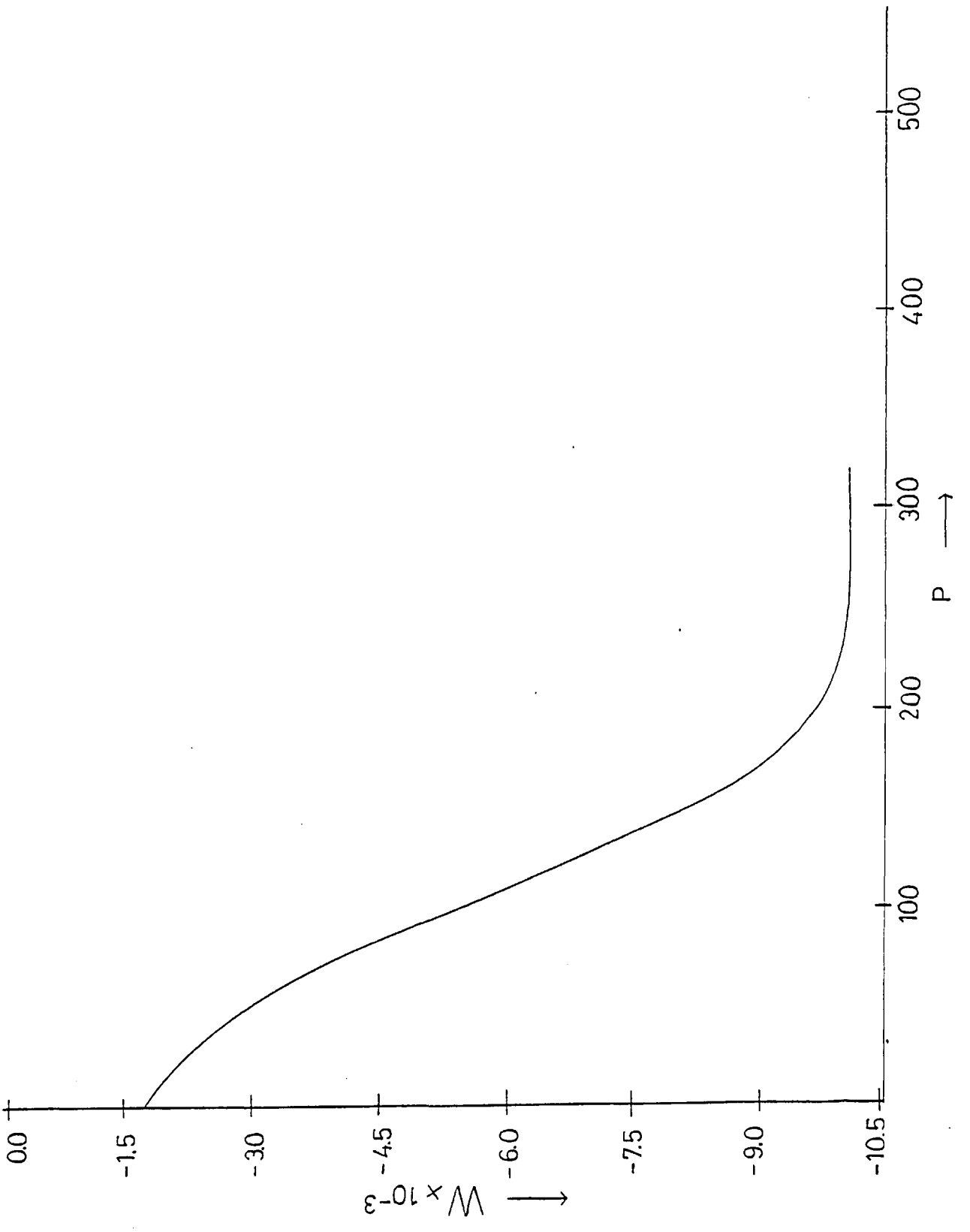

Figure 5.9 w plot, for Figure 5.4.

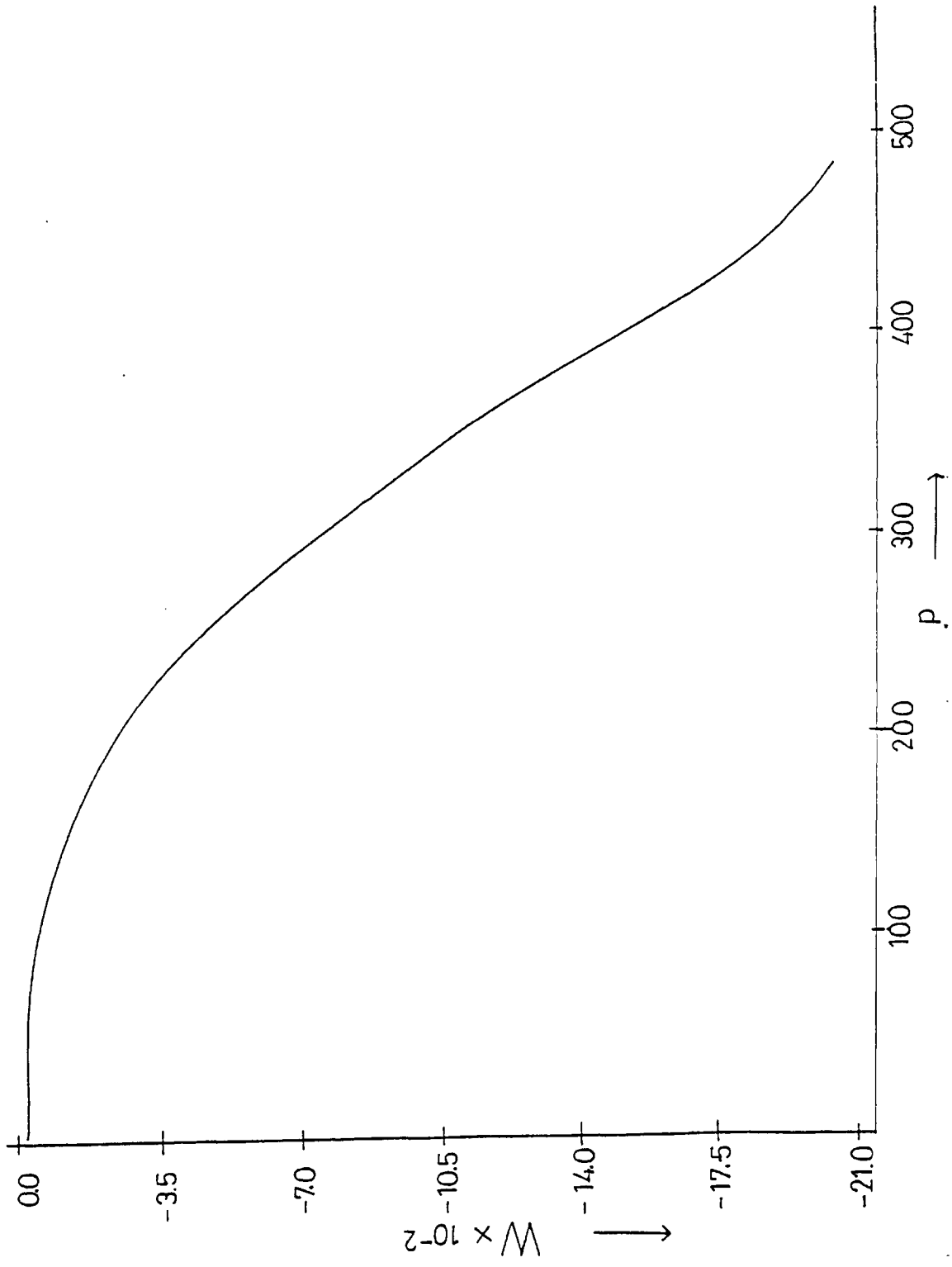

Figure 5.10 w plot, for Figure 5.5.

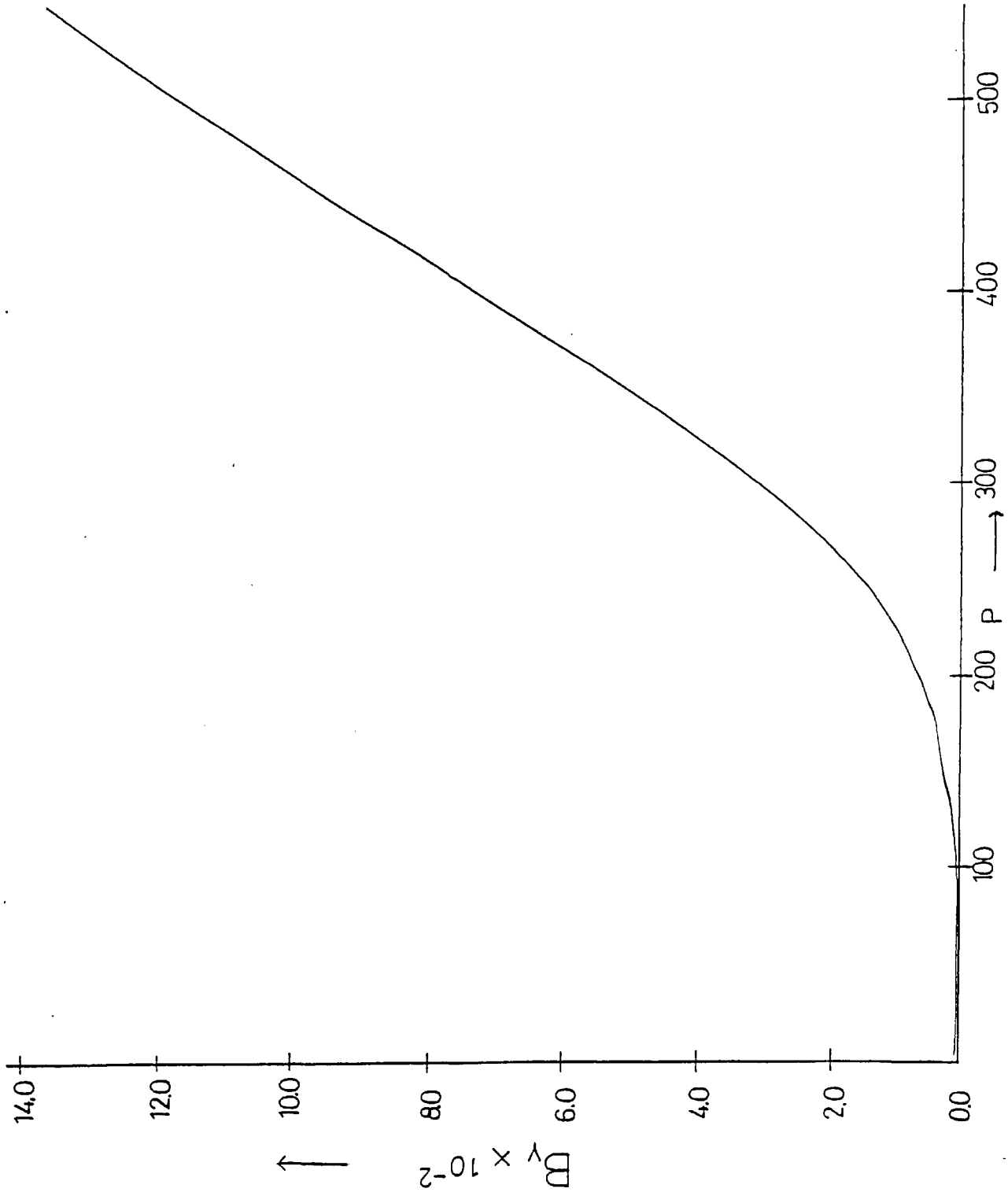

Figure 5.11 B_y against P for cosθ = 0.007.

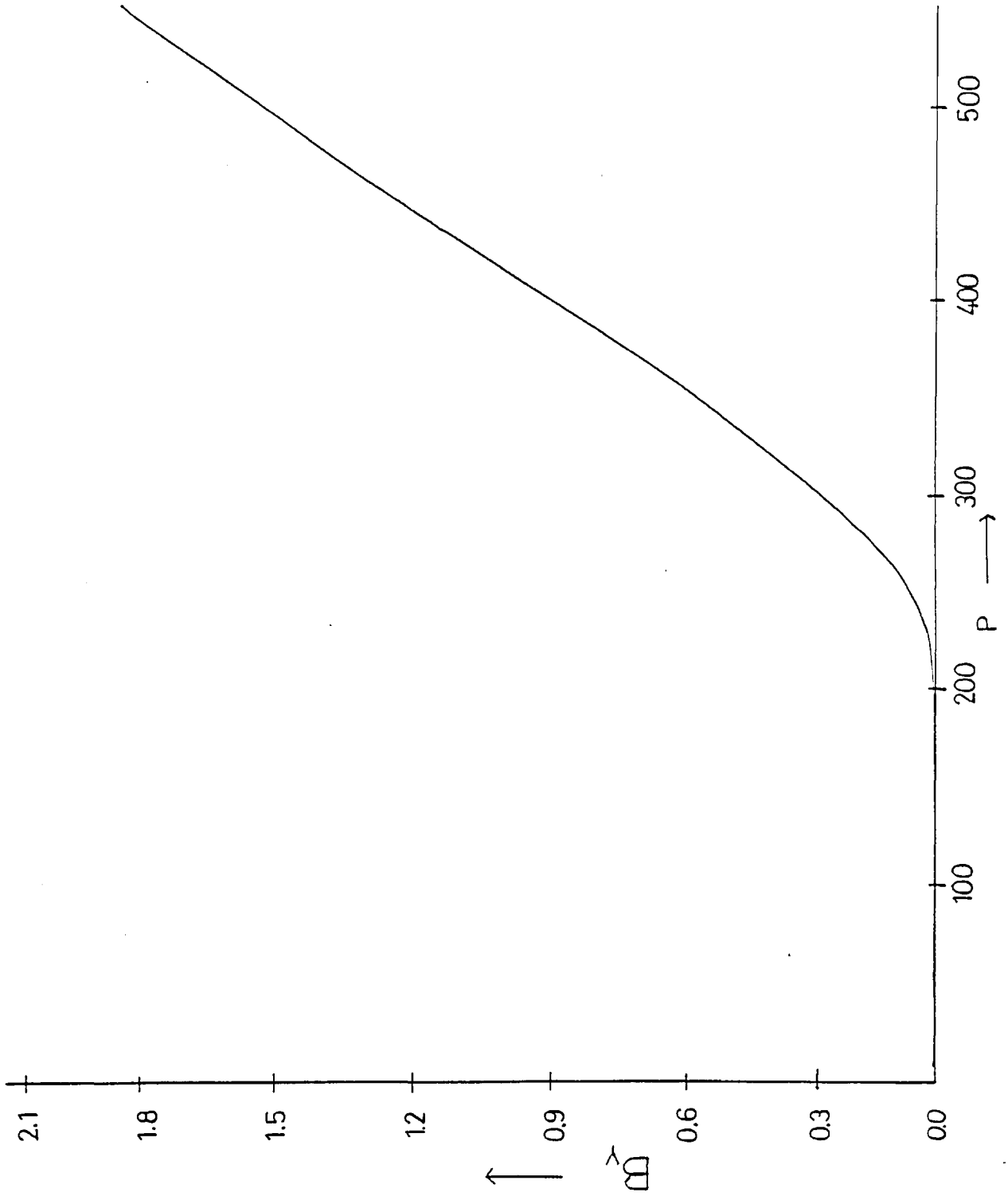

Figure 5.12 B_y against P for $\cos\theta = 0.0009$.

the Alfvén mach number was constant for each case at 0.01, the growth rate can be easily estimated, and is 0.007 and 0.011 s^{-1} for Figures 5.11 and 5.12 respectively, thus an angular change of less than 0.35^{o} results in an order of mangitude reduction in the $\underset{\sim}{B}_y$ perturbation.

The full dependence of σ on cos θ is shown in Fig.5.13 which represents the results of several computations for which $0.0009 \lesssim \cos\theta \lesssim 0.00999$. The computation itself is insensitive to very small changes in $\underset{\sim}{B}_z$, hence as $\underset{\sim}{B}_z$ is almost 1.0 it is generally adequate to approximate it to be exactly unity. However, in order to check the Alfvén mode approximations (eqns 4.50 and 4.51), we require a knowledge of b_{xo}. This is easily obtained from eqn.4.25 which defines the normalised magnetic field by the following equation :

$$\underset{\sim}{B}_o = (\underset{\sim}{B}^2_{xo} + \underset{\sim}{B}^2_{zo})^{\frac{1}{2}}$$

and upon using $b_{xo} = \underset{\sim}{B}_{xo}/\underset{\sim}{B}_o$ we obtain,

$$b^2_{xo} + b^2_{zo} = 1$$

and if b_{zo} is now taken as 0.999999 (cf. Fig.5.5, Table 5.1), then this produces a value of b_{xo} equal to 0.0014, hence, from equation 4.51, which states :

$$\sigma << (\gamma b_{xo})^{-1}$$

we are able to satisfy this condition.

However, the other condition (equation 4.50), states :

$$\frac{\sigma v}{\gamma^{\frac{1}{2}} w b_{xo}} = -\frac{1}{(\gamma b_{xo})^2}$$

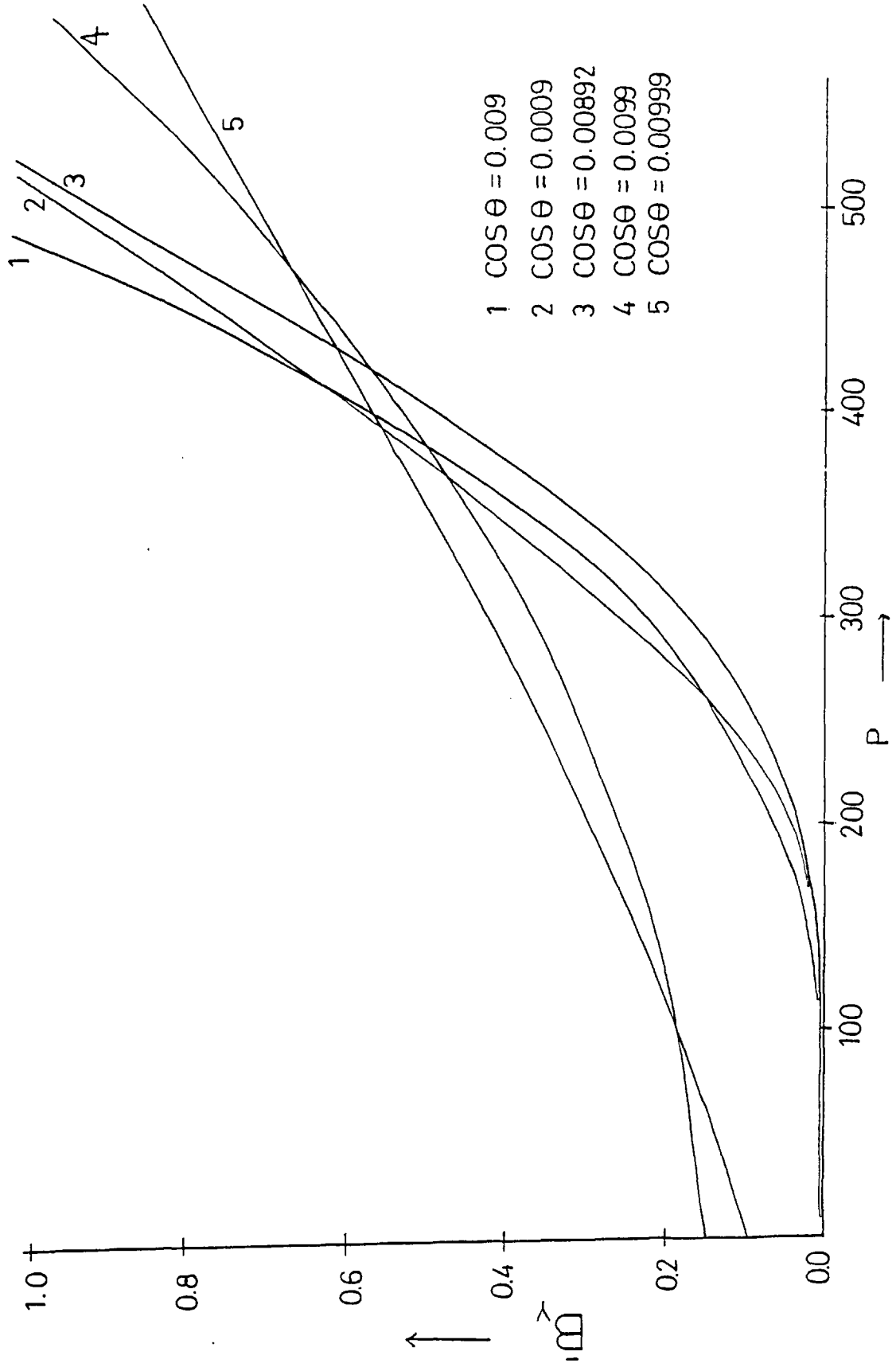

Figure 5.13 B_y against P for five values of cosθ. The B_y scale is normalised and the diagram is to show variation of growth rate only.

in which we compute v from $v = \frac{b_{xo} b_y}{M_A}$ (see Chapter 4); and upon taking representative values of b_y and w from the non-linear region, for which purposes we may assume that when b_y goes from the exponential to the non-linear region, then this corresponds to the point on the exponential where w assumes the value for the straight line portion.

If this is done we find that the second approximation is no longer valid; this therefore implies that $\frac{dv}{d\tau}$ in equation 4.30 should now be computed in a similar fashion to $\frac{dw}{d\tau}$ and $\frac{db_y}{d\tau}$. We therefore need to reconsider the approximations, and to base new ones on the non-linear region. The main point here is in the scales of the linear and non-linear regions of the plots; the linear theory done in Chapter 3 is adequate to allow an estimation of the space scales of the linear region, however the corresponding scales for the computed non-linear portion are different. We therefore require approximation which are based on the straight line part of the plot and this is explained in more detail in the next subsection.

5.2.1 Scales for the Exponential and Non-linear Regions

Considering the exponential region first, we have defined in Section 4.3, Chapter 4, the following equation :

$$\frac{d}{d\tau} = u\frac{d}{dx}$$

However, on the right hand side u and x are dimensionless, i.e. $u = u/V_A$ and $x = x\omega_{pe}/c$ it is therefore convenient now to re-define according to :

$$\frac{d}{dx'} = u\frac{d}{dx} \quad \text{(as we wish to consider spatial scales).}$$

Thus for the purpose here we have

$$\frac{d}{dx'} \approx \frac{(M_A^2 - \cos^2\theta)^{\frac{1}{2}}}{M_A}$$

As the abscissa of the plots are expressed in terms of the electron plasma wavelength c/ω_{pe}, where C is the velocity of light and ω_{pe} the electron plasma frequency, we therefore have sufficient information to estimate the computed scale. As c/ω_{pe} is a function of the number density n, and for most purposes can be approximated by

$$\frac{c}{\omega_{pe}} = \frac{5}{(n)^{\frac{1}{2}}} \text{ km}$$

the scale of the linear region is therefore given by

$$\text{Scale} = \frac{M_A}{(M_A^2 - \cos^2\theta)^{\frac{1}{2}}} \frac{5}{(n)^{\frac{1}{2}}} \text{ km}$$

However, for the non-linear, straight line region we know from Chapter 4 that $u = \cos^2\theta/M_A$, to quite high accuracy. We also have an expression for w, viz.

$$w = (ub_z - M_A b_{zo})/b_{xo}$$

whereupon substituting for u, and using $b_{zo} \approx 1$ and $b_{xo} \approx \cos\theta$ we obtain

$$w = \frac{\cos\theta}{M_A} - \frac{M_A}{\cos\theta}$$

Furthermore, from equation 4.28, viz

$$\frac{db_y}{d\tau} = \gamma^{-\frac{1}{2}} \{M_A w + b_{xo}(b_z - b_{zo})\}$$

Whereupon, keeping only the dominant term and substituting for w produces :

$$\frac{db_y}{d\tau} \approx \gamma^{-\frac{1}{2}} \{\frac{M_A^2 - \cos^2\theta}{\cos\theta}\}$$

The point where the exponential passes over to the straight line corresponds to the point where the non-linear effects begin to predominate. We can find an expression for b_y at this point by noting that $\frac{d}{d\tau} \approx (M_A^2 - \cos^2\theta)^{\frac{1}{2}}$, which gives

$$b_y \approx \frac{\gamma^{-\frac{1}{2}}(M_A^2 - \cos^2\theta)^{\frac{1}{2}}}{\cos\theta}$$

This equation is a function of $\cos\theta$, and is generally $< \gamma^{-\frac{1}{2}}$. We therefore see that at the point of non-linearity b_y is usually small.

In addition to the above equation, we also have from the approximations done in Chapter 4 :

$$v = \frac{ub_y}{b_{xo}} = \frac{ub_y}{\cos\theta}$$

and substituting again for u produces :

$$v = \frac{\cos\theta}{M_A} b_y$$

Differentiating with respect to τ gives :

$$\frac{dv}{d\tau} = \gamma^{-\frac{1}{2}} \frac{(M_A^2 - \cos^2\theta)}{M_A}$$

Hence from the approximation equation (4.50), we have

$$\frac{dv/d\tau}{\gamma^{\frac{1}{2}} w \cos\theta} = \frac{M_A^2 - \cos^2\theta}{\gamma M_A w \cos\theta} \approx -\frac{1}{\gamma}$$

which suggests that the approximation is still valid.

In discussing the scale size for the non-linear region it is

important to note that a rotation of the field is occurring at this point, the increase in the field-aligned electron speed constitutes the current which then perturbs the b_y component of the magnetic field; as this perturbation grows the field undergoes a rotation which is just b_y radians.

Thus, in this case for unit radian rotation the scale is given by :

$$\frac{M_A \cos\theta}{M_A^2 - \cos^2\theta} 5\left(\frac{\gamma}{n}\right)^{\frac{1}{2}} \text{ km}$$

and the straight line scale is therefore greater than the linear exponential region.

Summarising, for both regions, linear and non-linear, the scales are functions of the angle θ, and the number density n, which may be taken as 0.1 cm^{-3}. The value of b_y when the non-linear terms take over is small, and generally $< \gamma^{-\frac{1}{2}}$, however from equation 4.50 we can infer that the approximation is probably still valid.

The essential difference between the computed plots and observation lies in the fact that the computation shows the perturbation to be continually increasing. This is clearly something which could not take place in reality, and by the time the computation would exhibit this facit warm plasma effects should have become important. At this time instabilities will also become important, especially the two stream instability, a simulation of which would require extra terms in the equations. This is primarily because in many cases the velocity grows from zero and goes unstable at a drift velocity which is much less than the electron thermal speed. At this time non-linear effects arise to prevent the further increase of the drift velocity. However it is unlikely that the inclusion of a

pressure term would be sufficient to simulate the above effect. This may be seen by considering the following :

The Lorentz equation with pressure included can be written in the following form :

$$n_\varepsilon m_\varepsilon \frac{Dw}{Dt} = e_\varepsilon n_\varepsilon (\underset{\sim}{E} + \underset{\sim}{V} \Lambda \underset{\sim}{B}.) - \nabla P$$

where $\varepsilon = \pm$ depending on species and $\frac{D}{Dt} \equiv \frac{\partial}{\partial t} + \underset{\sim}{u}.\nabla$, if $P \approx \gamma nkT$ and $c^2 = \gamma kT/m$ then we can perturb, and solve for w in the form :

$$w = \frac{e_\varepsilon}{m_\varepsilon i\omega} (\underset{\sim}{E} + \underset{\sim}{V} \Lambda \underset{\sim}{B}) - \frac{c^2}{\omega^2} \underset{\sim}{k} (\underset{\sim}{k}.\underset{\sim}{w})$$

However, for general θ, the shear mode wave has $\underset{\sim}{k}.\underset{\sim}{\omega} \approx 0$, because they are almost perpendicular, therefore cold plasma theory should be adequate, at least initially, to describe the behaviour. It is therefore likely that to account for the actual non-linear behaviour throughout the whole range of the computation would at best require a term in the equations which would take account of any microturbulence which may be present, or at worst a kinetic approach along the lines of quasi-linear theory.

5.2.2 A case of particular interest to consider is the changes which occur as $\cos\theta$ approaches, and becomes equal to 0.00999, and Figure 5.14 shows the variation of the $\underset{\sim}{B}_y$ perturbation for $\cos\theta$ = 0.0099, 0.00995 and 0.00999, which corresponds to an angular change of only 0.005^o. The growth rate is clearly substantially reduced for the $\cos\theta$ = 0.00999 case, and can again be calculated approximately from $\sigma \approx (M_A^2 - \cos^2\theta)^{\frac{1}{2}}$ which gives values of $\sigma = 1.4 \times 10^{-3}$ and 4.6×10^{-4} for the $\cos\theta$ = 0.0099 and 0.00999 cases respectively. This is more clearly seen in

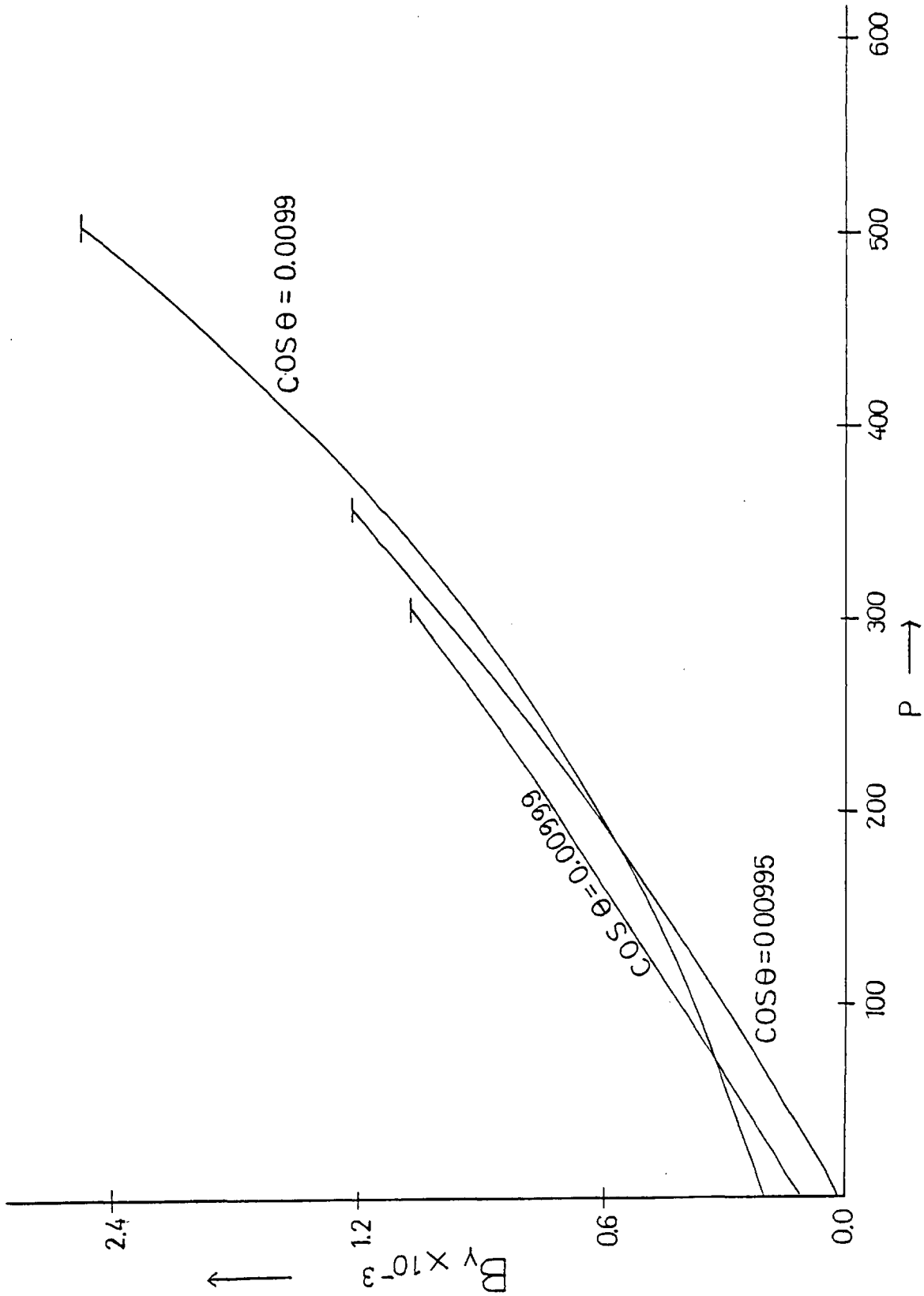

Figure 5.14 Variation of growth rate as cosθ approaches 0.00999.

the velocity plots (Figures 5.15, 5.16 and 5.17), in which Figure 5.17 represents the case of $\cos\theta$ = 0.00999 and shows that w exhibits a tendency to decrease slightly, if only in the second decimal place. Once again, if the approximations for the Alfvén mode are tested we find that equation 4.50 is violated, and we can no longer trust the predictions of the computation. The order of magnitude decrease in the growth rate for such a small change in angle exemplifies how crucial the orientation of the wave normal with respect to the magnetic field is in determining a sensible rate of growth.

5.3 The Case for Positive w(1) and Negative $B_y(1)$

It can be seen from Table 5.1 that the sign of the starting values for w(1) and $B_y(1)$ were the same for each run. However, the predictions of linear theory should be essentially unchanged if w(1) is made positive and $B_y(1)$ negative. Figure 5.18 shows the case for the following set of parameters :

$\cos\theta$ = 0.0096

$B_y(1)$ = -0.0000935

w(1) = 0.00187

B(z) = 1.000000

u(1) = 0.009982

and a ΔT = 2.0. The figure shows the same initial exponential growth, and an order of magnitude increase across the region of computation (which is largely in the linear regime). Figure 5.19 shows the corresponding velocity plot which again shows features which are almost identical to the case of opposite sign.

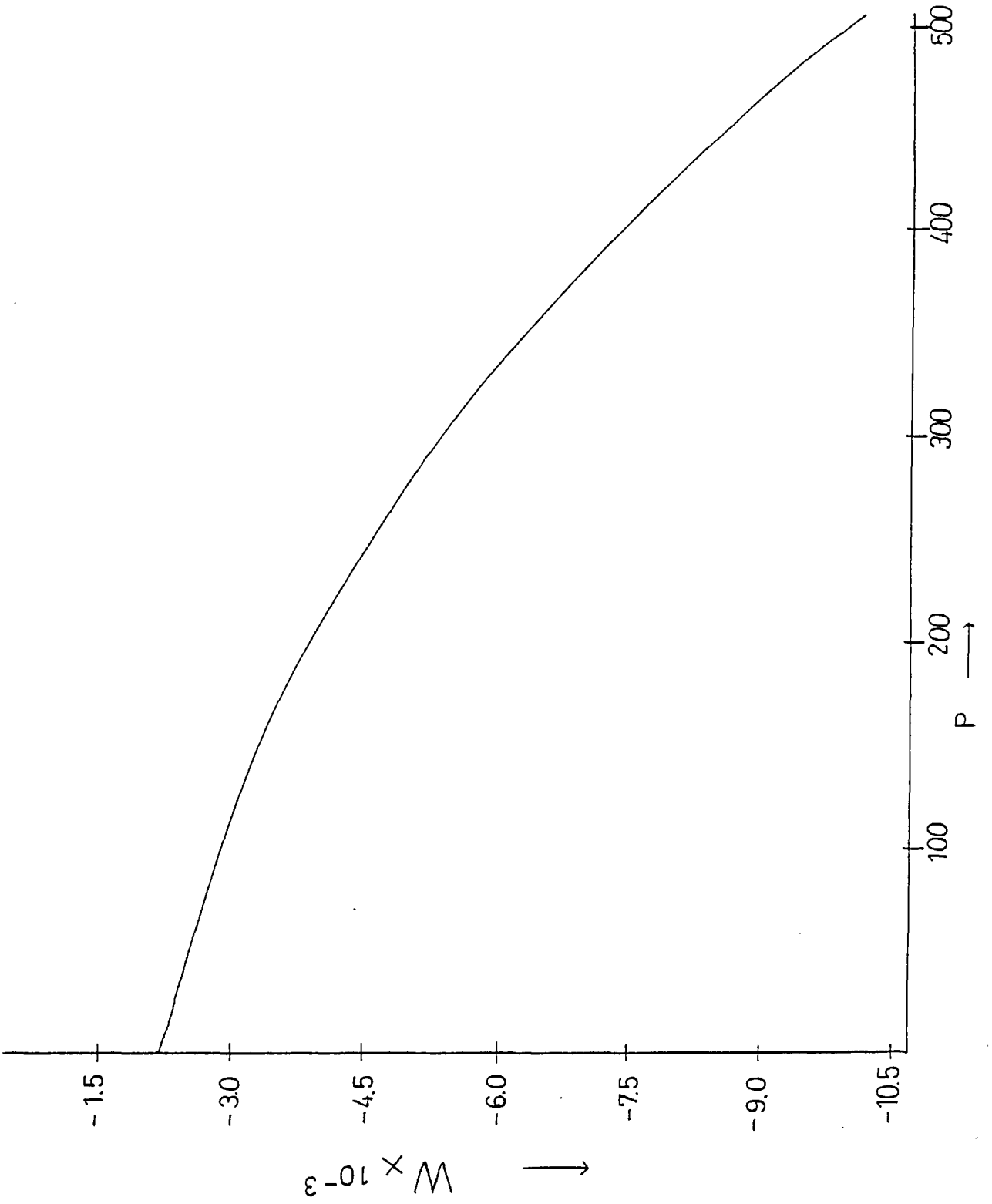

Figure 5.15 w plot for cosθ = 0.0099.

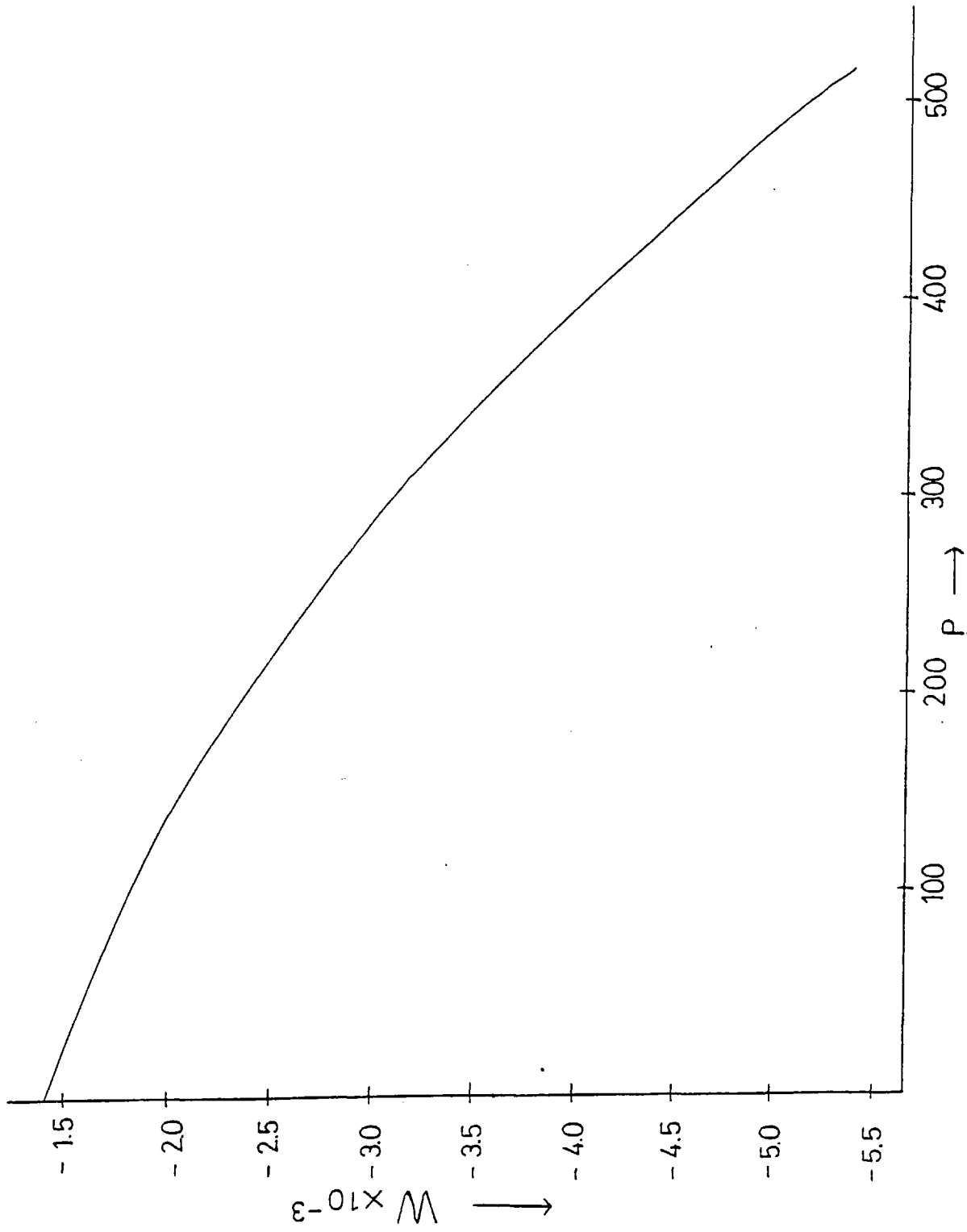

Figure 5.16 w plot for cosθ = 0.00995.

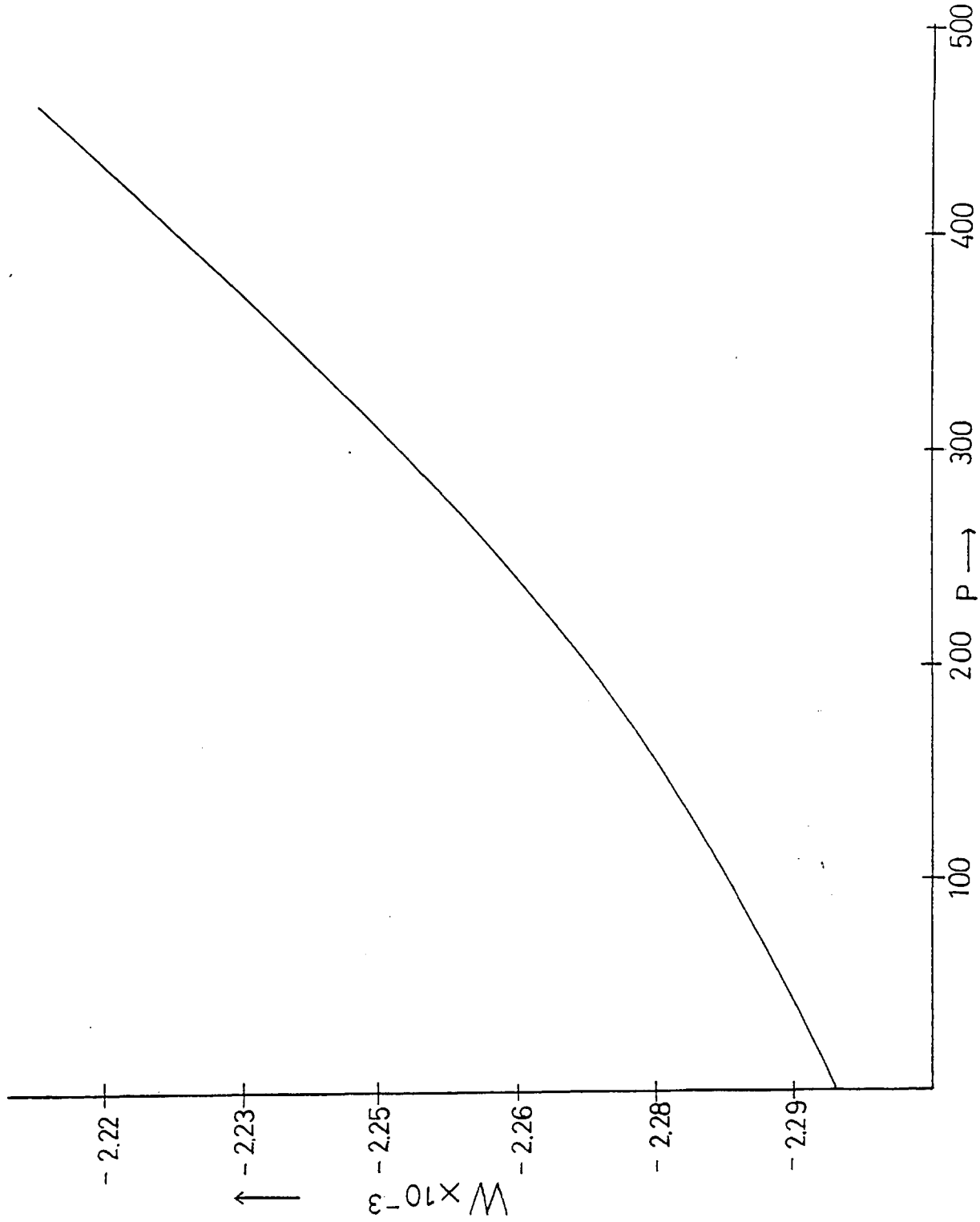

Figure 5.17 w plot for cosθ = 0.00999.

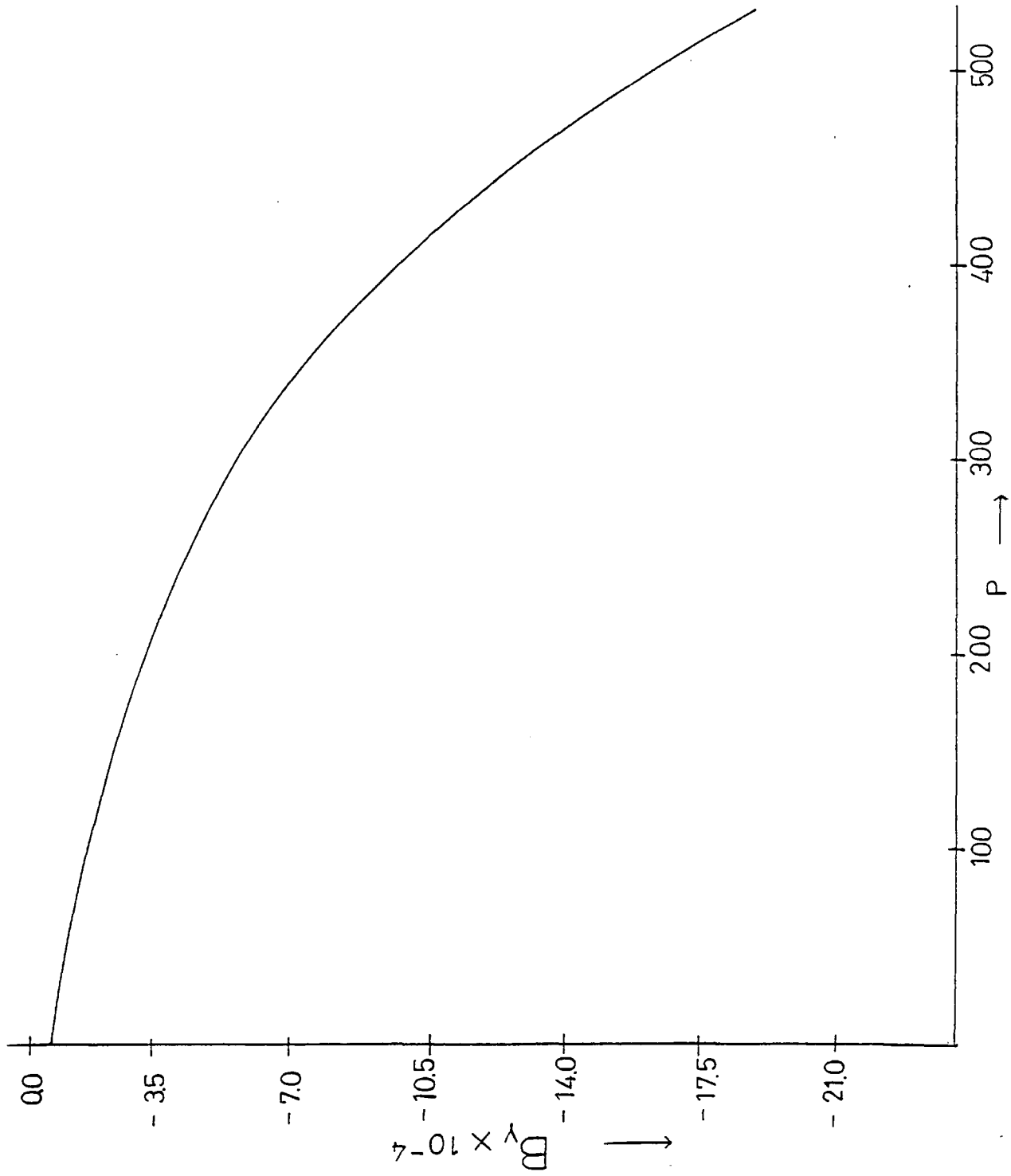

Figure 5.18 Plot of B_y against P for negative $B_y(1)$ and positive $w(1)$. $\cos\theta = 0.0096$.

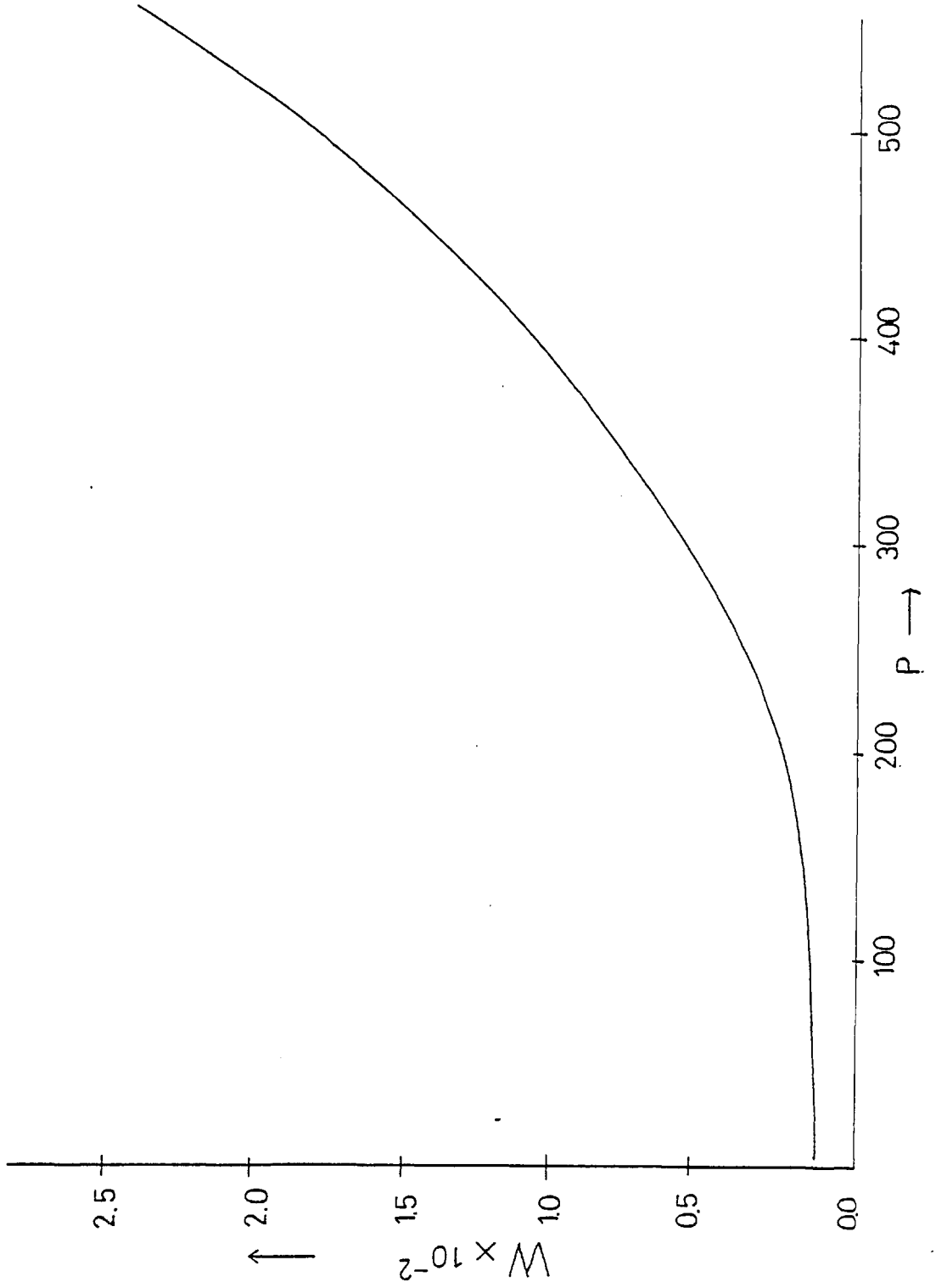

Figure 5.19 w plot for Figure 5.18 case.

5.4 Summary

The previous two subsections have displayed plots resulting from solutions of the cold plasma equations which were used to model the propagation of a current carrying shear mode Alfvén wave which could arise via the scenario given in Chapter 1. The essential point is that because of the field-aligned flow towards the earth, the current is tailwards and the linear theory predictions of exponential growth from a uniform state ahead of the wave should be followed by a period of constant current, which is also field-aligned, and which should manifest itself as a non-linear effect present in the $\underset{\sim}{B}y$ component of the magnetic field perturbation. This effect has been shown to be present for a wide range of parameters and the effect of the angle between the wave normal and the magnetic field was shown to be the crucial parameter in determining the growth rate. The question to be asked now is whether such signatures are seen in actual spacecraft magnetic data and if so can a similar interpretation as to the nature of the field-aligend currents causing them be made? The next subsection will therefore briefly introduce the ISEE mission and discuss what is seen upon crossing the boundary of the plasma sheet.

5.5 The ISEE Spacecraft

The International Sun-Earth Explorer (ISEE) is a three spacecraft mission deployed to measure the dynamic properties of the magnetosphere and its surrounds. The heart of the mission consists of a pair of spacecraft (ISEE 1 and 2), with carefully matched payloads which orbit through the magnetosphere at a known, and controllable distance apart. By observing the time difference and the variation of characteristics between the passage of each spacecraft through a given phenomena, the speed and direction of

magnetospheric boundaries such as the bow shock, magnetopause or the boundary of the plasma sheet can be determined, and the spatial and temporal variations can be separated, something which is not usually possible from single platform measurements.

ISEE 1 and 2 were launched in October 1977 and both spacecraft travel in identical orbits which have an initial apogee and perigee of 22.6 R_e and 270 km respectively. The orbit remains static in space, so as the Earth orbits around the sun the line of apsides rotates through the magnetosphere, as shown by Fig.5.20, where the date circle indicates the apogee line at the time shown. This figure also shows why spacecraft data presented in this chapter comes from the first half of the year. The speeds and separation distance of the two spacecraft vary considerably around the orbit and although the separation in time is almost constant, separation distances vary from about 200 km at apogee to about 1000 km at perigee. Adjustment to the separation distance can be controlled by means of thrusters on board ISEE 2.

At the beginning of this section mention was made of a three spacecraft mission, and while no ISEE 3 data is discussed in this work it should perhaps be stated that the third spacecraft is in a halo orbit around the Earth-Sun libration point, and is therefore well placed for solar wind studies, and correlative work between upstream and downstream phenomena.

Finally, the instrument on board ISEE 1 and 2 which supplies the magnetic data, later to be discussed, is the UCLA fluxgate magnetometer which consists of orthogonal triads of ring core sensors having two ranges, ± 8192γ and ± 256γ for each of the three magnetic field components. The accuracy is ± 0.0025% of full range, and the data available is averaged over 0.5, 4.0, 16.0 and 64.0 seconds; the

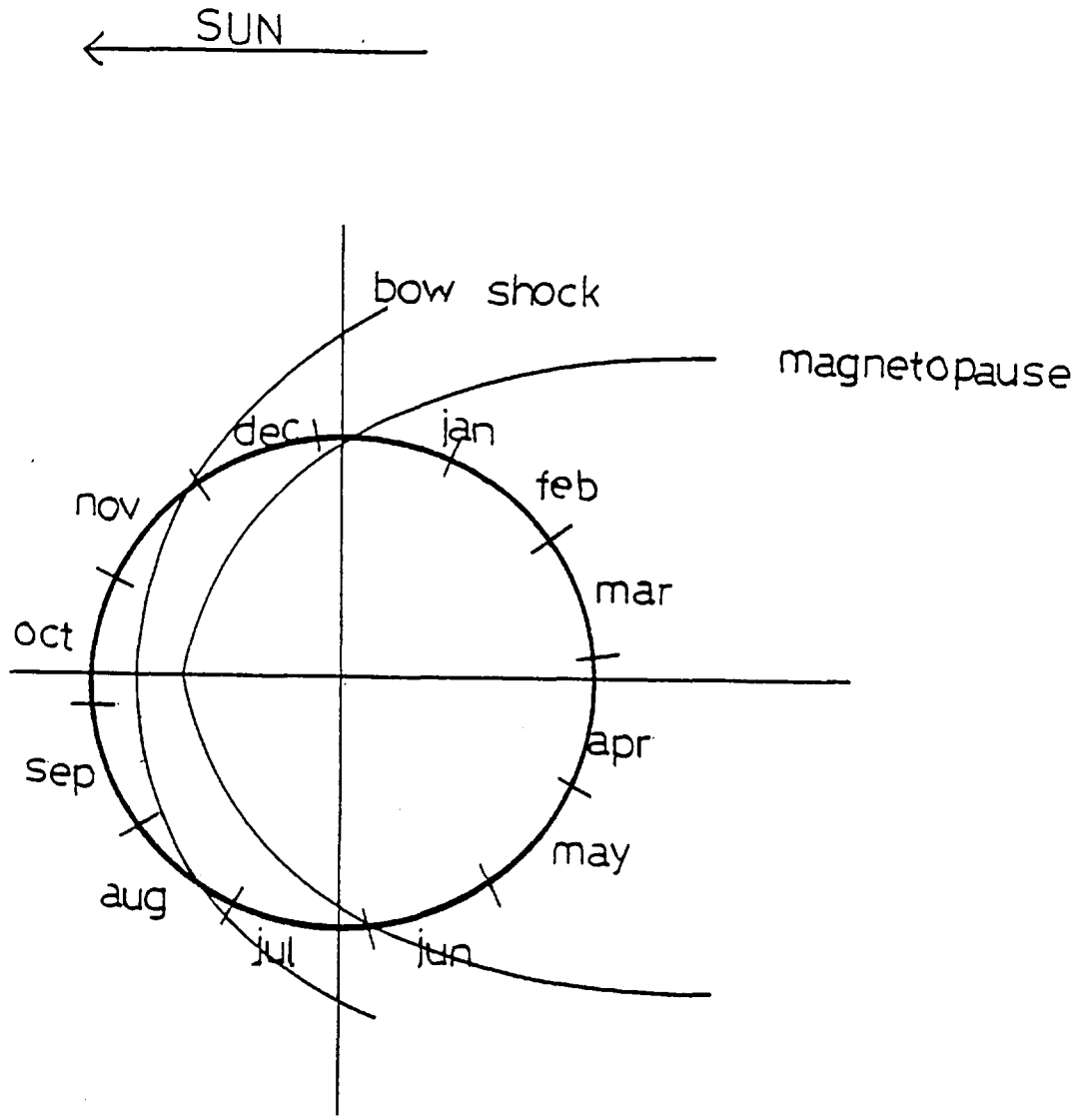

Figure 5.20 Lines of apsides for ISEE spacecraft orbit.

lesser dynamic range, ± 256γ is generally employed for magnetotail measurements (Russell, 1978; Frank et al, 1979).

5.6 Plasma Sheet Characteristics

The plasma sheet, the location of which is shown in Fig.1.1, Chapter 1, is perhaps the most dynamic region in the terrestrial magnetosphere; it consists of a reservoir of warm plasma particles with an inner edge located between 7-10 R_e in the geomagnetic equator, and although the magnetotail has been calculated to extend to at least 1000 R_e (Dungey, 1965), observations of the tailward extent of the plasma sheet have been reported at lunar orbit, which is about 60 R_e down tail. The plasma sheet was predicted theoretically by Parker (1958) and seems to be an intrinsic feature of the interaction of a plasma flow agains a magnetised obstacle. The importance of studying plasma sheet dynamics is based upon the fact that it is central to the fundamental processes that control the dynamic response of the magnetosphere to certain changes in solar wind conditions. In the near Earth plasma sheet unidirectionally streaming particles are seen as the spacecraft encounters the boundary of the plasma sheet (BPS), the fast flow layer being terminated on its inner boundary by the return flux of particles which has the effect of reducing the net bulk speed to smaller values (Coroniti et al, 1980; Carbary and Krimigis, 1979). Observed thicknesses of this layer are about 1 R_e (Hones, 1977; Frank et al, 1979), and relate to plasma flows observed in the plasma sheet region during both expansion and recovery phase associated with substorms (Hones et al, 1972a; Hones, 1977; Frank et al, 1976); these flows have been shown to be predominantly field-aligned (Lui et al, 1977; Frank et al, 1978b; De Coster and Frank, 1979). The ion distribution functions of

these flows have been investigated by several authors (Frank et al, 1979), who show them to be of the "mushroom cap" variety, the axis of which is almost field-aligned, which may be interpreted as a wide spread in pitch angle combined with a narrow spread in velocity about the mean.

Inside this fast flow layer, that is closer to the centre line, is the plasma sheet proper, which is characterised by particle distributions which are more nearly Maxwellian : Spjeldvik and Fritz (1980).

The overall picture then is consistent with an acceleration region (neutral line), downstream of the spacecraft observation point, and we are interested in the magnetic signature of the plasma sheet as the ISEE spacecraft cross the boundary, which is marked by field lines mapping between the neutral line and the auroral zone. The characteristic magnetic signature of a plasma sheet crossing is shown in Fig.5.21 and is seen to consist typically of a decrease in $|B|$ and B_x and a perturbation in the B_y component, the B_z component is usually seen to increase slightly.

While the fine structure of crossings may vary, the gross features given above are fairly consistent in that field-aligned currents are almost always seen to be flowing in the vicinity of the plasma sheet boundary : Parks et al (1979). It can be seen from the figure that the overall character of the plasma changes as the spacecraft traverse the plasma sheet, and the turbulent nature of the field trace is a result of the diamagnetic plasma within the sheet; this again is typical of almost all plasma sheet encounters.

5.7 BPS Events

This subjection will show a few selective plots of data

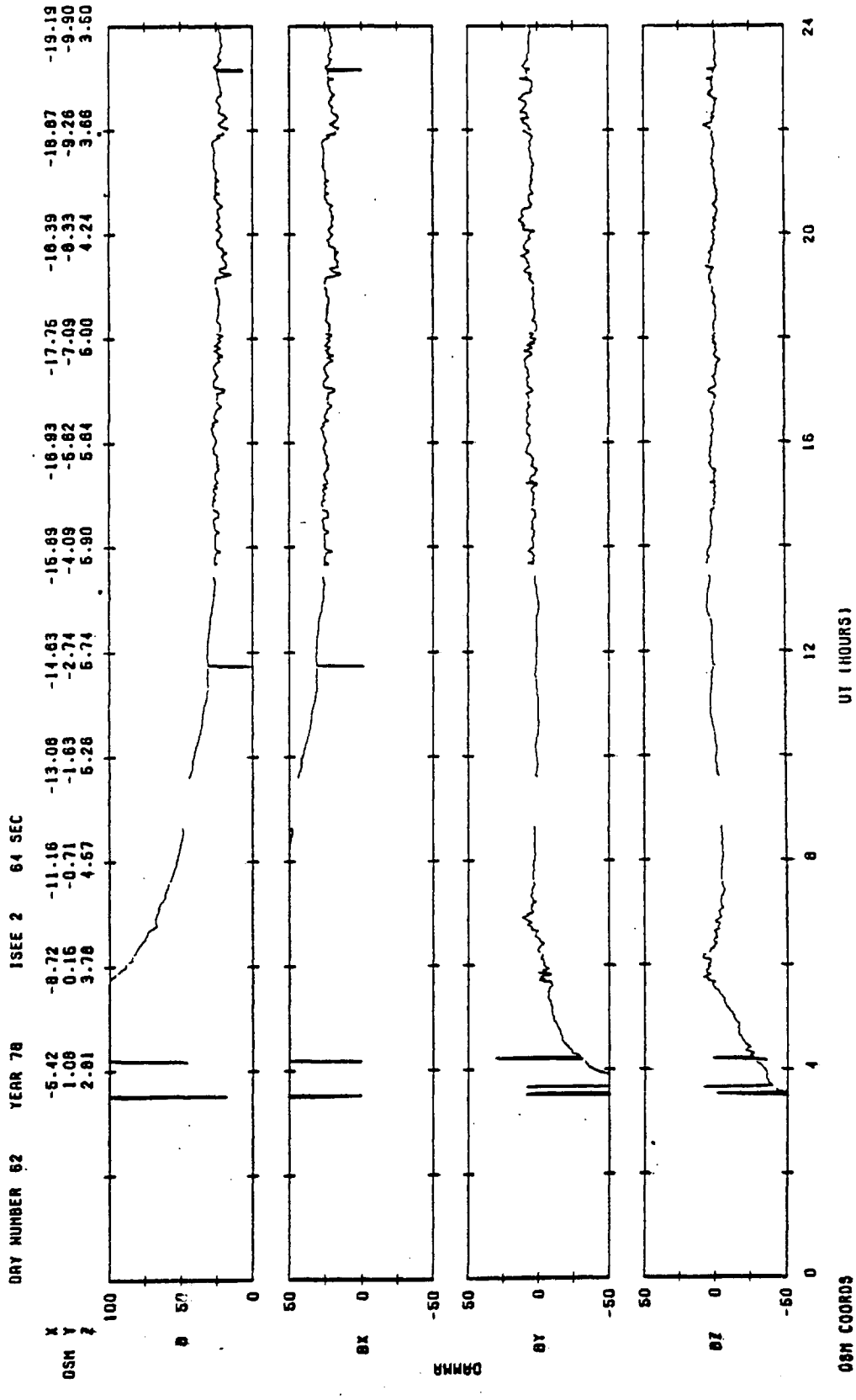

Figure 5.21 To show characteristics of plasma sheet crossing.

intervals which correspond to plasma sheet crossings. Because of the scaling, the x, y and z components are shown on separate plots, but both ISEE 1 and 2 are plotted on the same scale. Table 5.2 lists the relevant data for each event, and the events themselves correspond to Figures 5.22 through 5.33. Figures 5.25, 5.29 and 5.33 are magnetic hodograms, one purpose of which is to test the assumption of plane geometry upon which the cold plasma equations were computed, and Figure 5.29 in particular shows that this assumption is largely born out. These three figures will be returned to shortly.

The event represented by day 128 is an encounter with the plasma sheet which probably corresponds to the expansion phase of a substorm during which the plasma sheet undergoes large scale thinning; the boundary therefore contracts past the spacecraft which then finds itself in the high latitude lobe. As the sheet contracts the B_x component jumps to a lobe value of about 20γ, and the y-component shows the signature of field-aligned current flowing at the boundary. The B_y component shows a characteristic exponential rise from a hitherto quiet state, followed by a 4γ general increase in the perturbation; this would correspond to the non-linear region of the computed plots shown in Fig.5.2 etc. There is however a maximum reached, and the perturbation settles down to a value some 5γ higher than the initial state, the signature is therefore very much that of a collisionless shock, and if the argument for warm plasma effects causing the turn-over in B_y is applied then the data bears a reasonable relationship to the theoretical predictions.

The other events, days 94 and 86 are slightly different in that they occurred during the recovery phase of a substorm; a period during which the plasma sheet is being inflated with fresh plasma from the reconnection zone as the neutral line moves rapidly down

Figure Number	Day Number	Time at Start	Plot Duration	Approximate Crossing Time	x-position (R_E) (GSE)	y-position (R_E) (GSE)	z-position (R_E) (GSE)
5.22 5.23 5.24, 5.25	128	10.18	7 mins	10.20	-16.00	7.90	6.50
5.26 5.27 5.28 5.29	94	17.21	2 mins	17.22	-19.70	-3.39	6.22
5.30 5.31 5.32 5.33	86	10.44	6 mins	10.45	-15.00	2.70	7.00

TABLE 5.2 Showing Plot information and corresponding Figure numbers

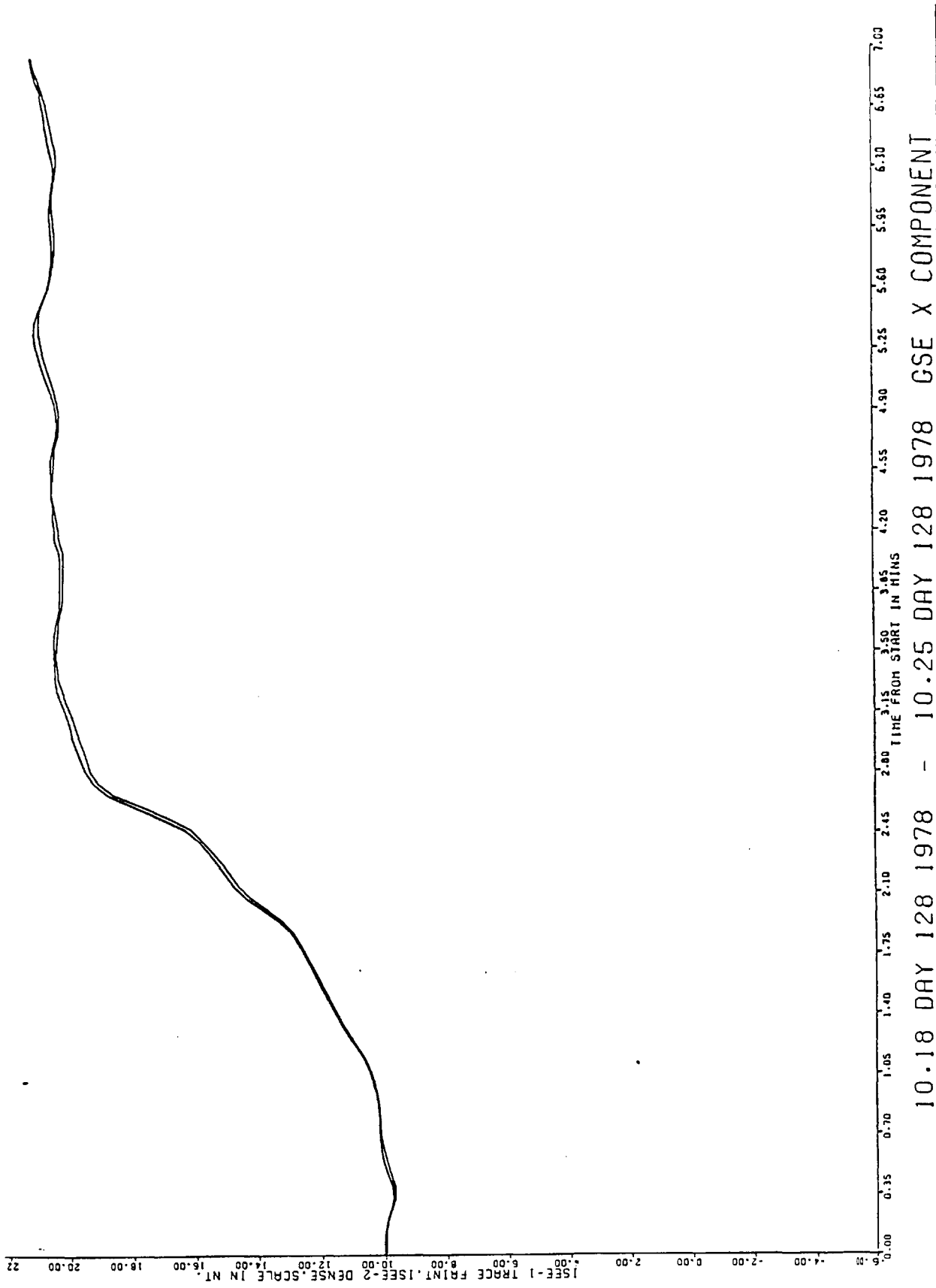

Figure 5.22 B_x for day 128 (10.18-10.25). ISEE 1 is the faint trace and ISEE 2 the heavy.

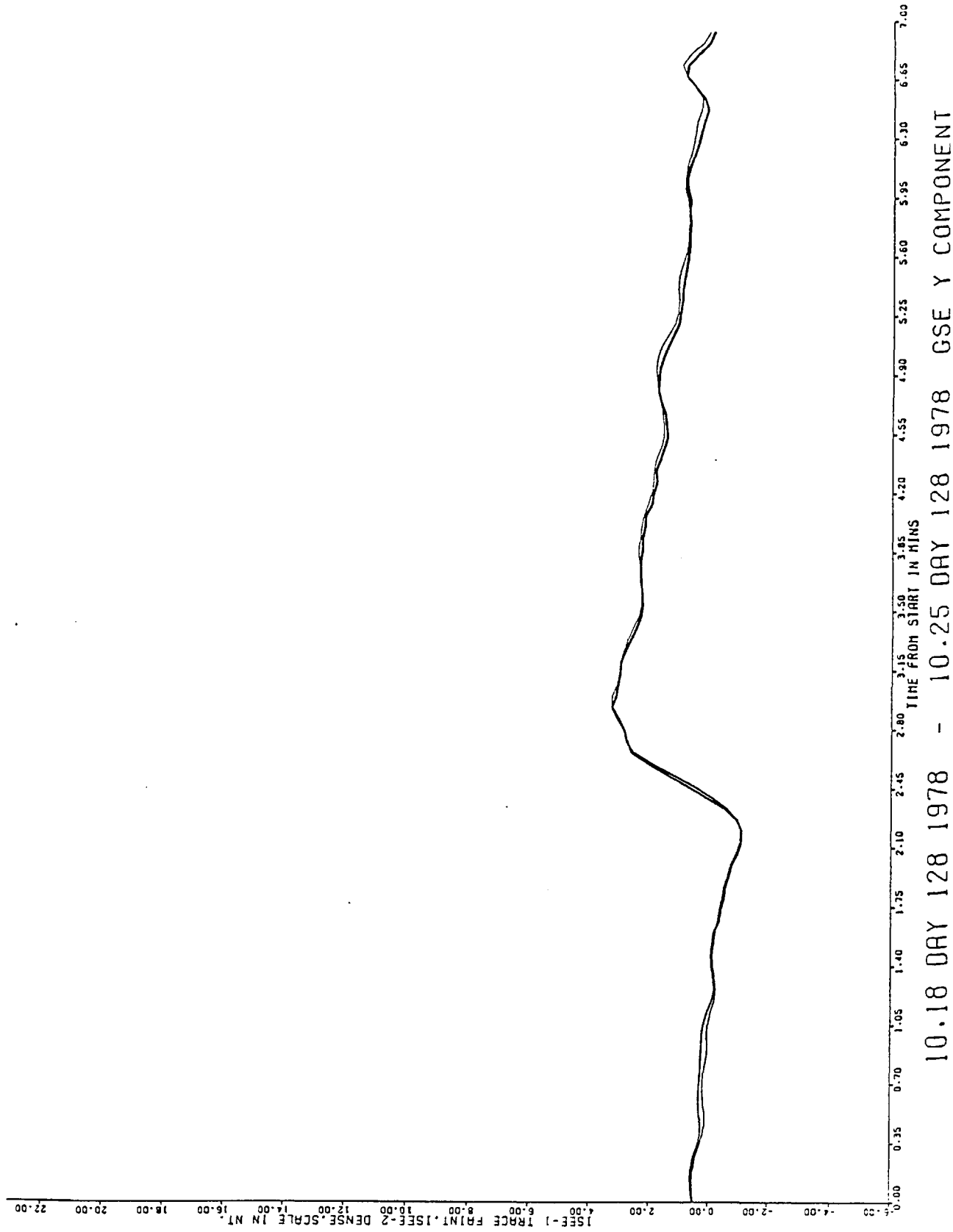

Figure 5.23 $\underset{\sim}{B}_y$ for day 128.

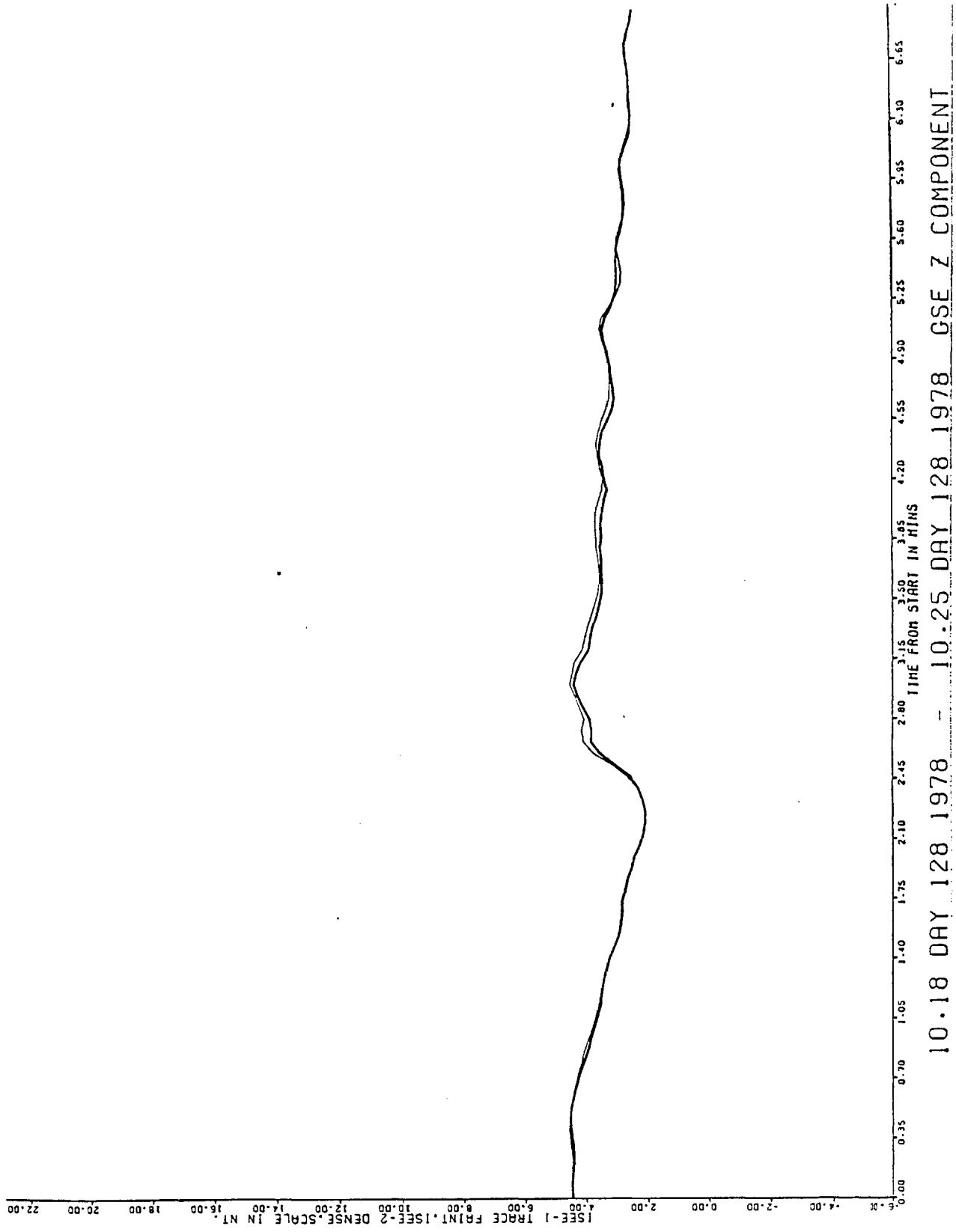

Figure 5.24 $\underset{\sim}{B}_z$ for day 128.

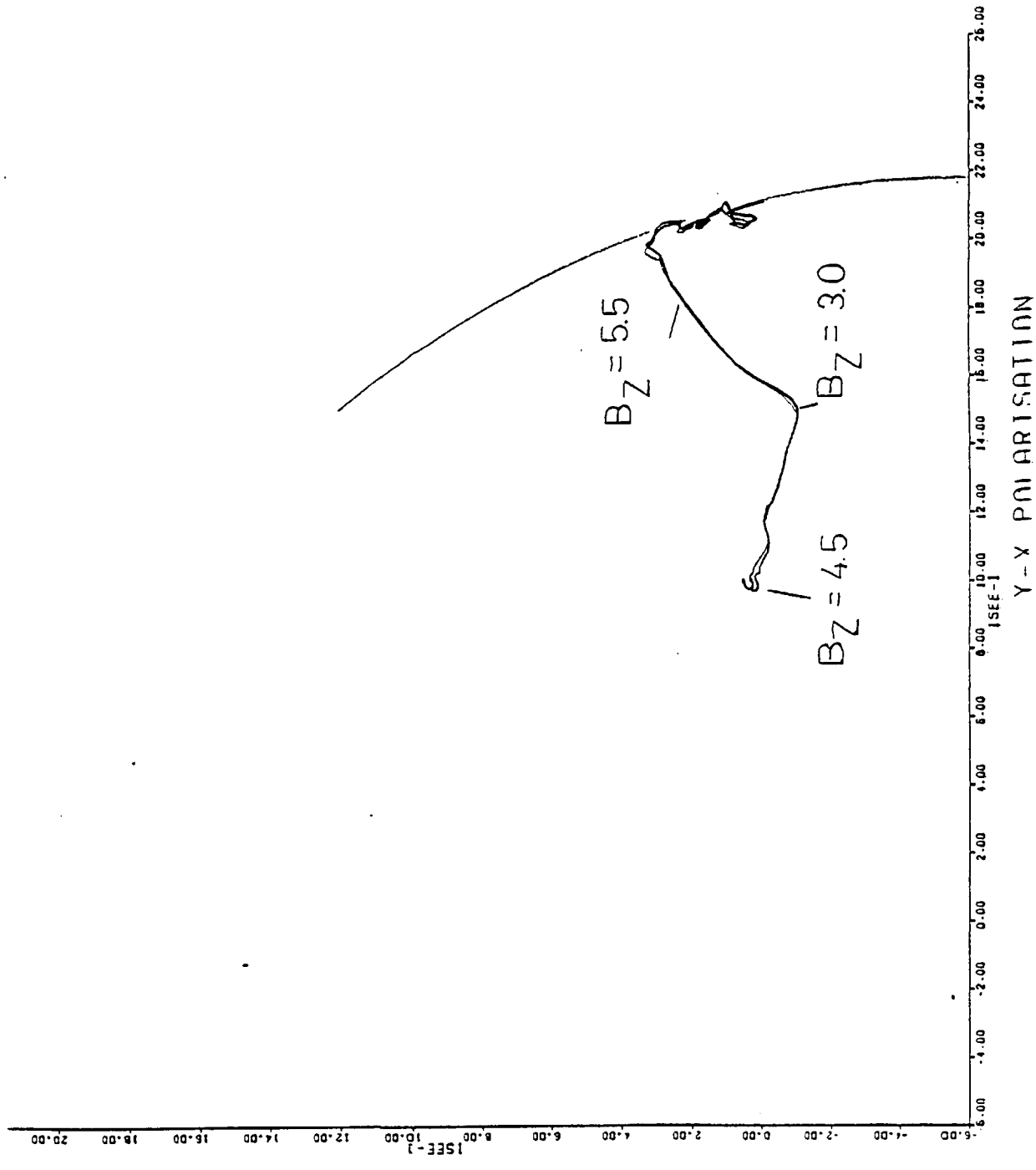

Figure 5.25 Magnetic hodogram for day 128 event.

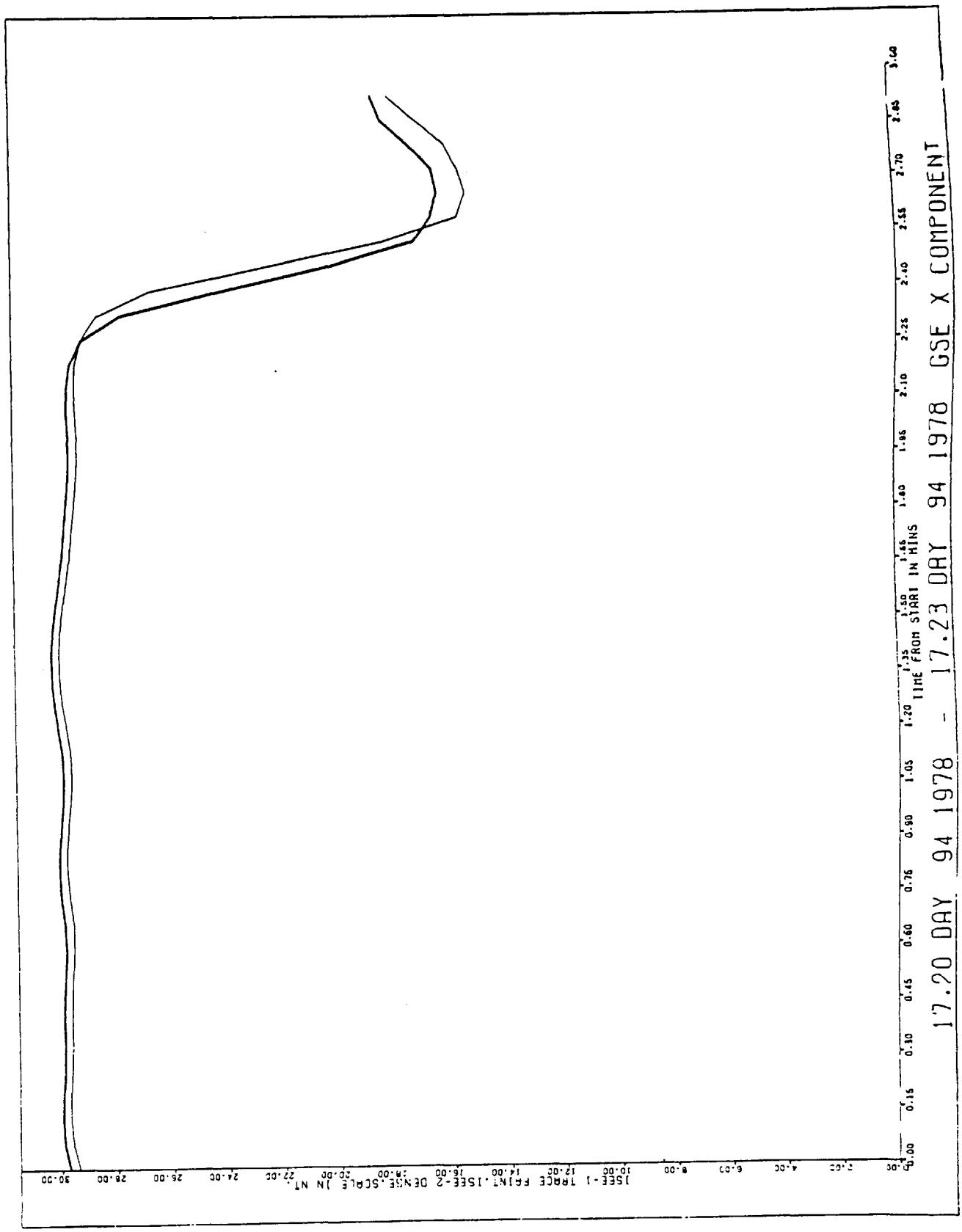

Figure 5.26 $\underset{\sim}{B}_x$ for 17-21-17.23 (day 94).

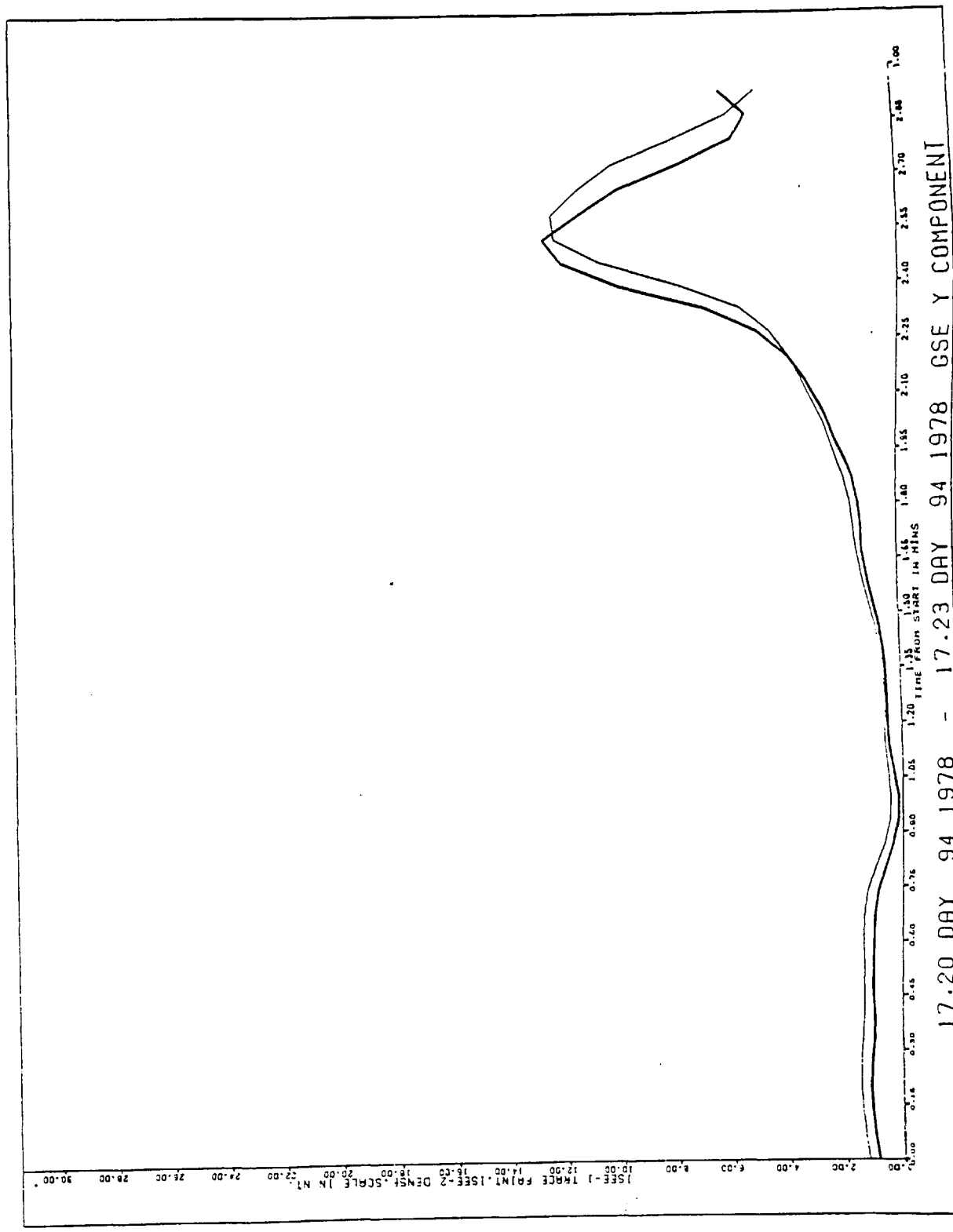

Figure 5.27 B_y for day 94.

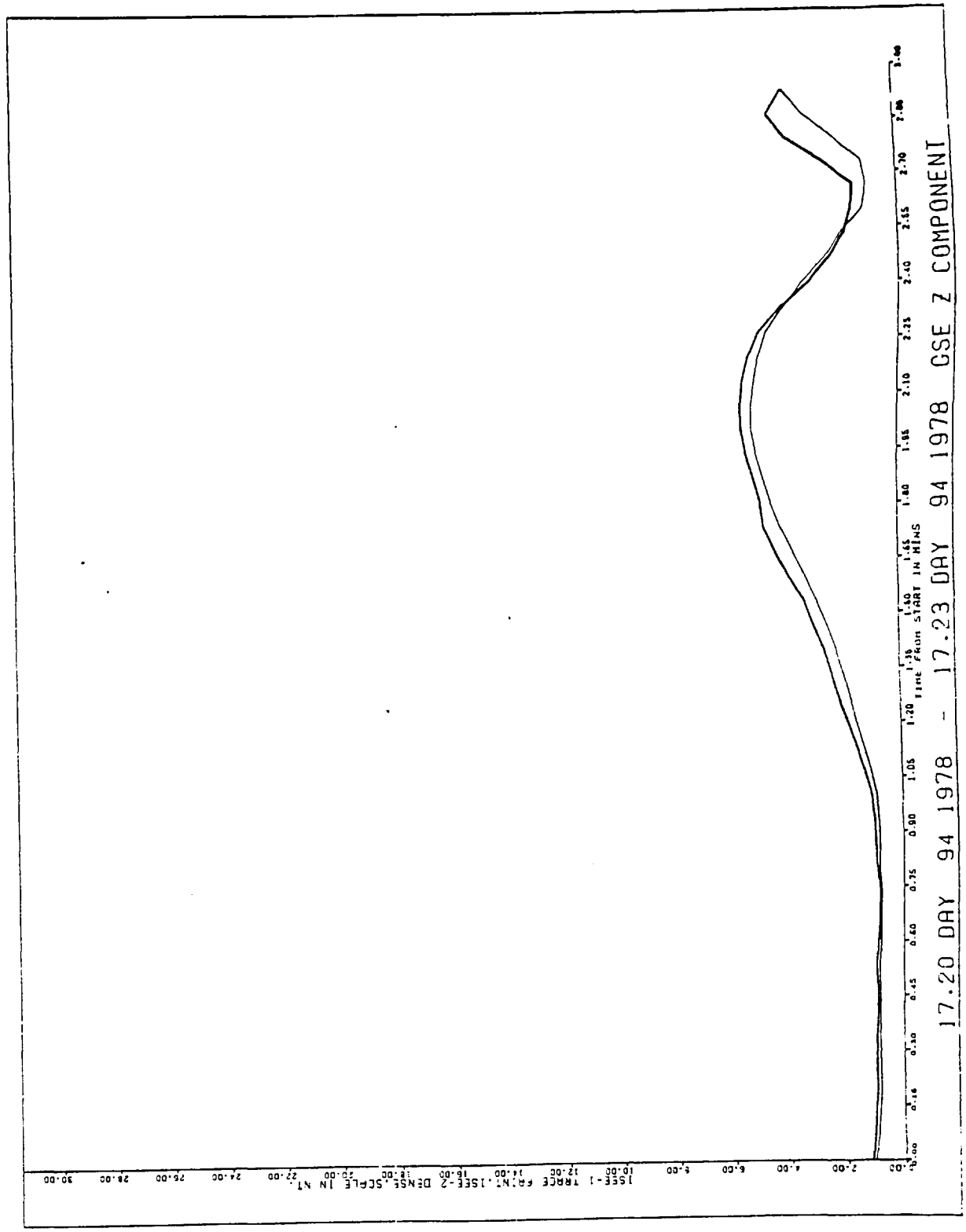

Figure 5.28 B_z for day 94.

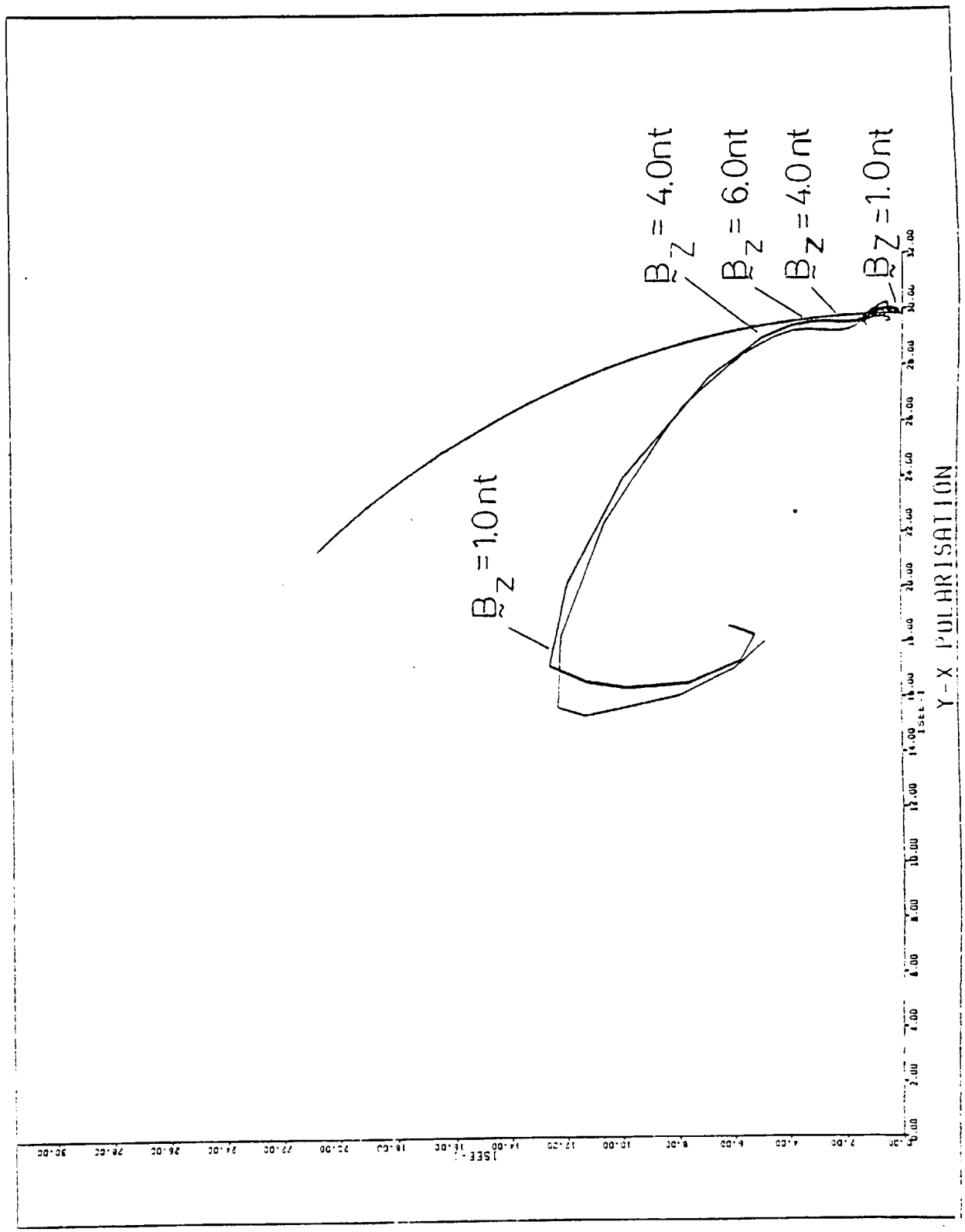

Figure 5.29 Magnetic hodogram for the day 94 event.

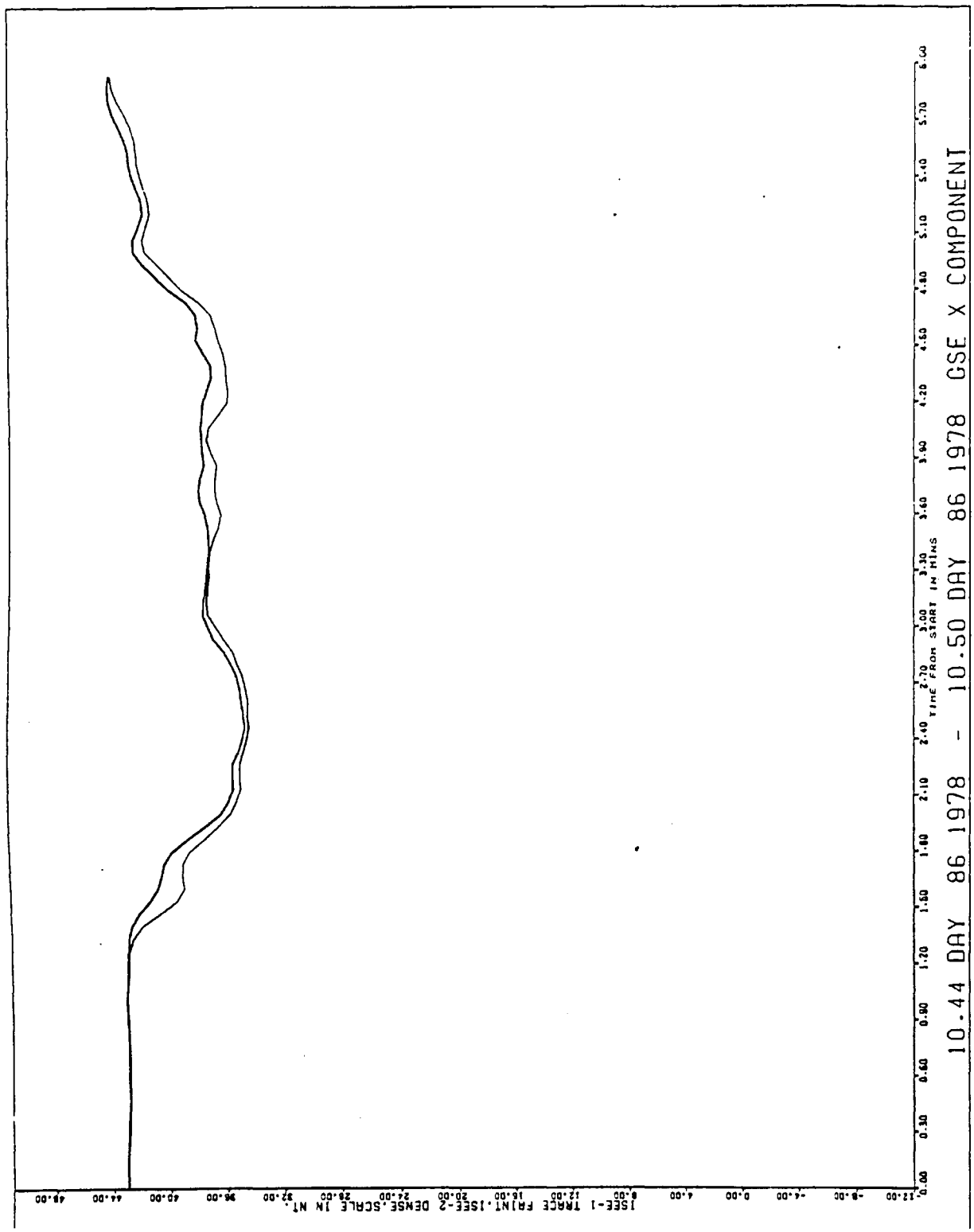

Figure 5.30 $\underset{\sim}{B}_x$ for 10.44-10.50 (day 86).

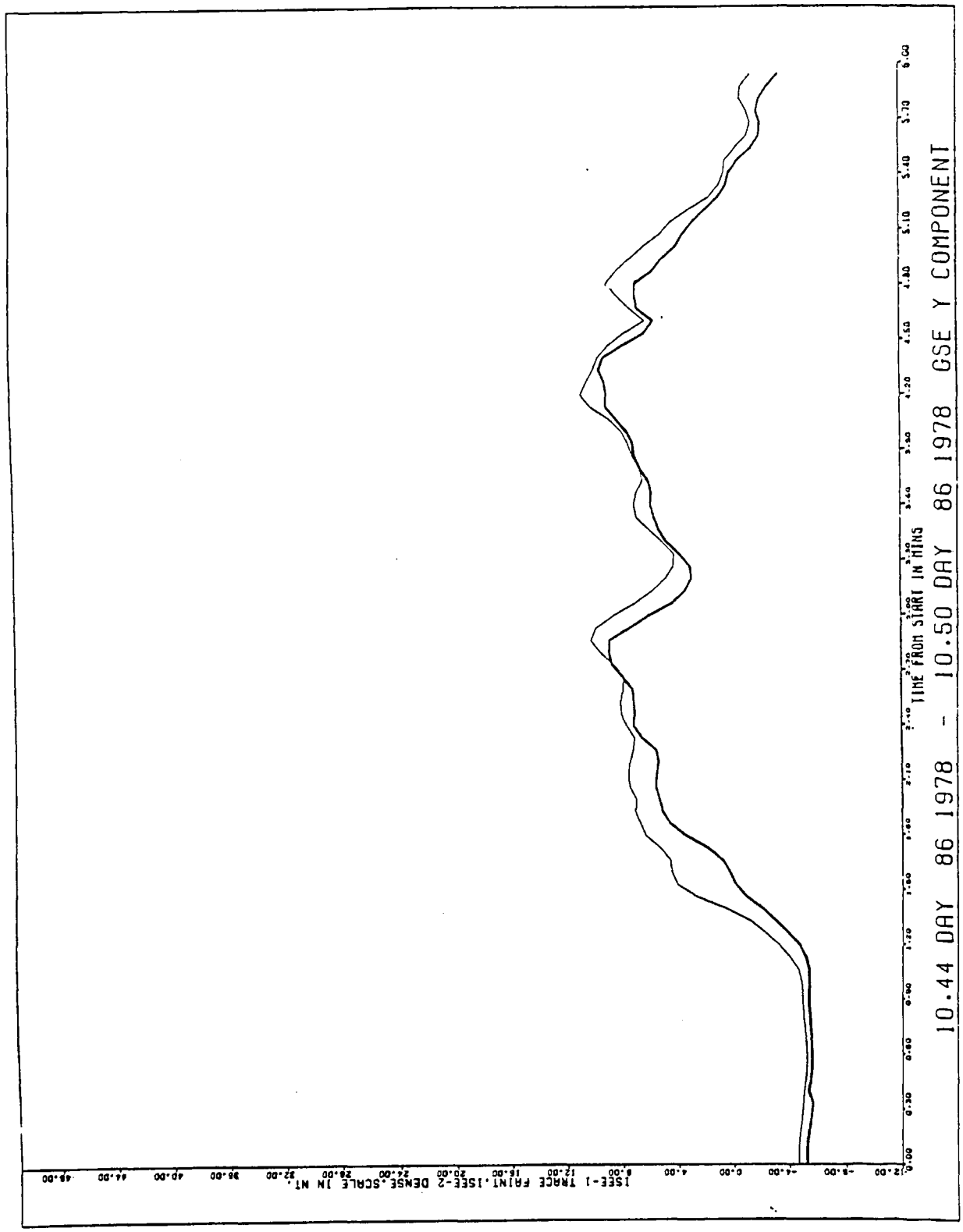

Figure 5.31 $B_{\sim y}$ for day 86.

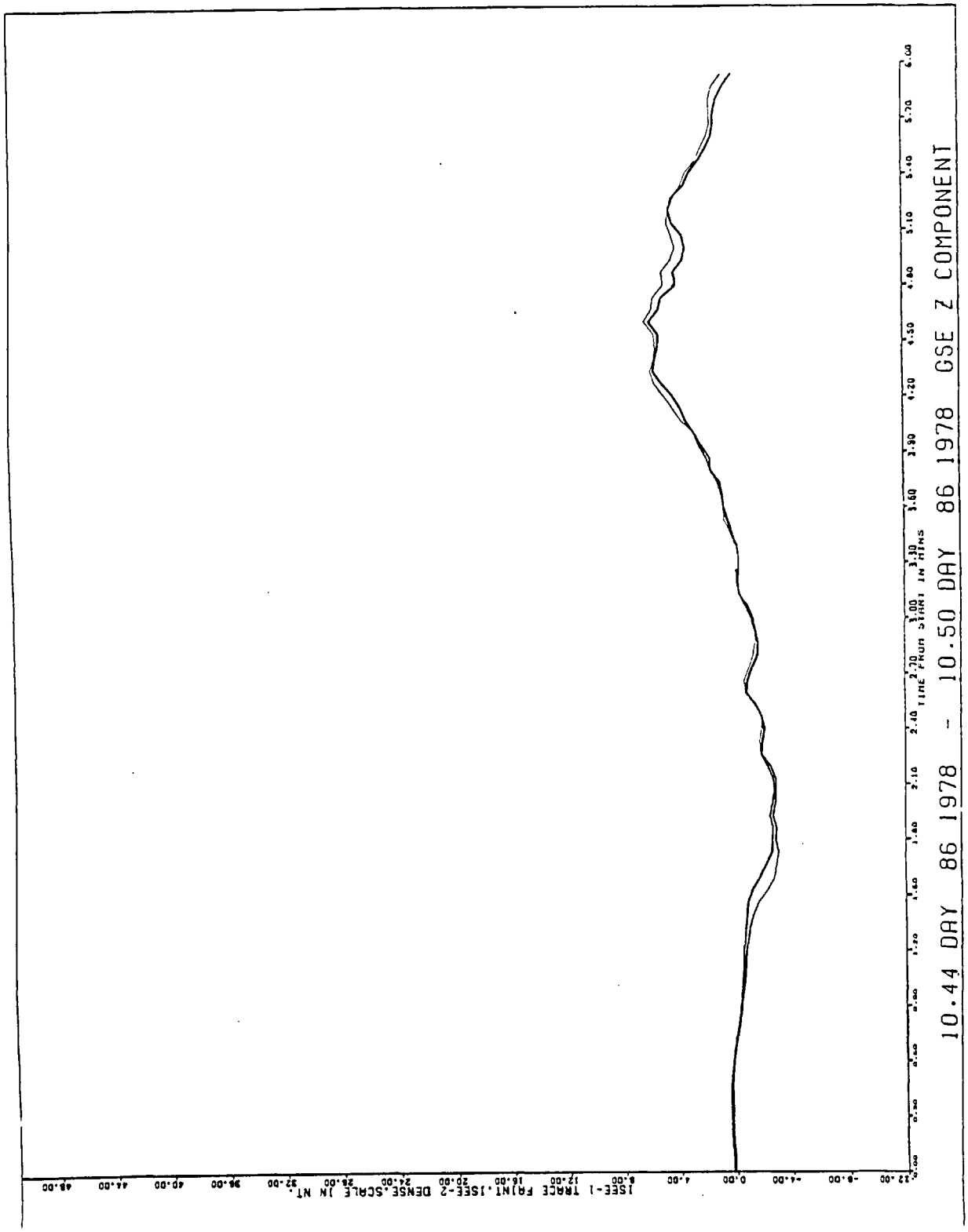

Figure 5.32 $\underset{\sim}{B}_z$ for day 86.

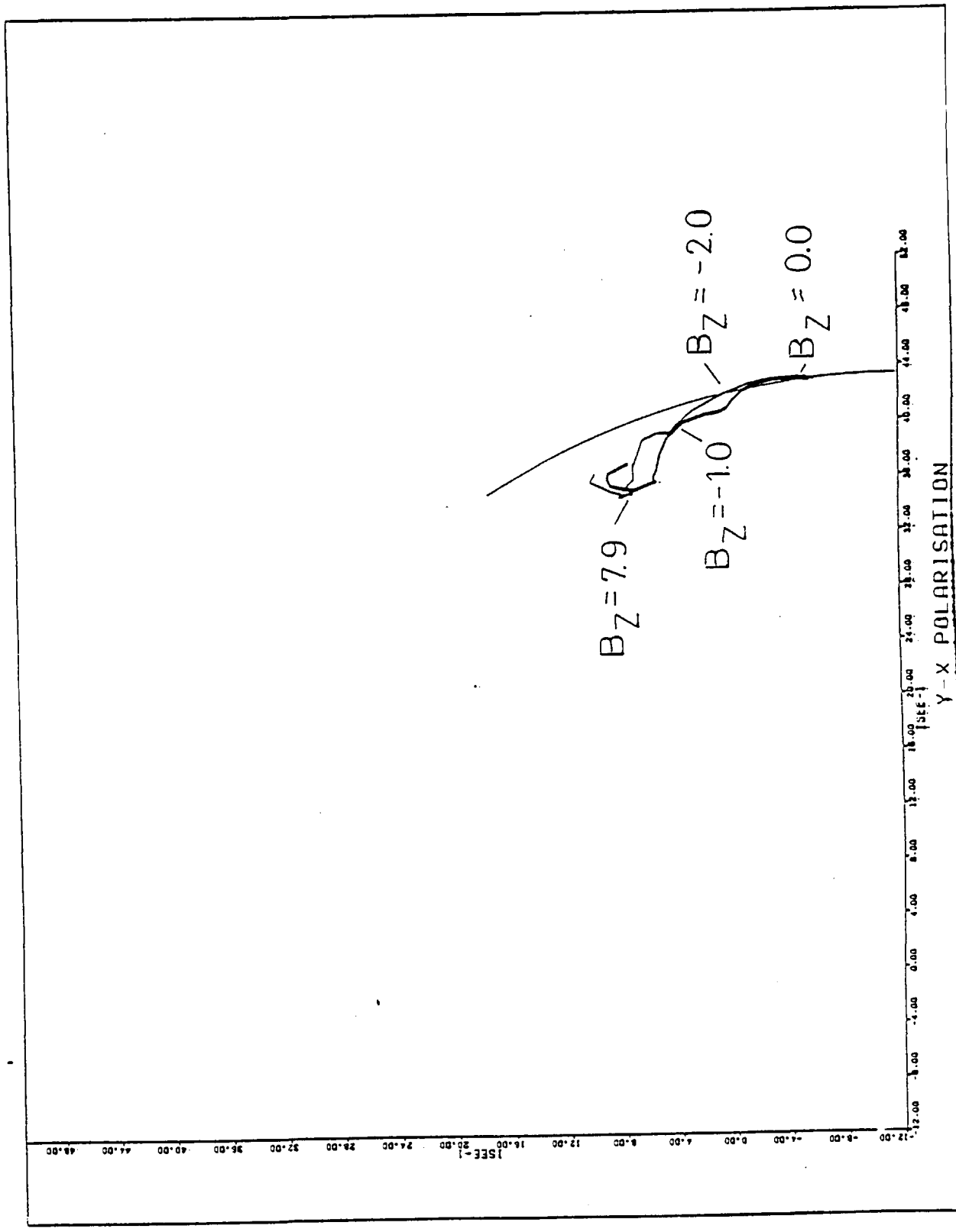

Figure 5.33 Magnetic hodogram for day 86 event.

tail. They were therefore seen by the spacecraft as the boundary of the plasma sheet expanded past them. Considering day 94, i.e. Figures 5.26 through 5.29, which show two minutes of data, the $\underset{\sim}{B}_x$ component shows a clear plasma sheet entry with ISEE 2 sampling the boundary some 10 seconds before ISEE 1 and passing from a lobe field of 30γ to a plasma sheet field of about 18γ. The $\underset{\sim}{B}_y$ component again shows the effect of the field-aligned currents, and the perturbation is again seen to have an exponential start going into a steady increasing region. Figure 5.29 is clearly indicative of plane geometry, showing a steady increase in $\underset{\sim}{B}_y$ as $\underset{\sim}{B}_x$ falls.

Because of the short time interval plotted in this event the similarity with the earlier computed plots is especially clear; and Fig.5.27 also enables a determination of the spatial scale, which also will be returned to shortly.

The final example, day 86, shows an example of multiple entry to the plasma sheet, and is again taken from a recovery phase when the plasma sheet was expanding past the spacecraft.

Multiple entry is a common feature and may be often seen on both the magnetic and plasma data; this is probably due to corrugations of the plasma sheet boundary, where the spacecraft then pass briefly into the sheet, exit from the corrugation and then re-enter for an extended period of time. This is clearly seen from the $\underset{\sim}{B}_x$ component on day 86, the first entry occurring at 10.45 where the field strength drops from 42γ to 34γ, the spacecraft samples the diamagnetic plasma of the plasma sheet for some 3.5 minutes only to exit back into the 42γ lobe field at about 10.48; a second entry then occurs at about 10.52 and the spacecraft then goes on to be engulfed by the expanding plasma sheet. The $\underset{\sim}{B}_y$ component shows a large system of currents flowing on the boundary, but we can still see the quiet lobe field

rising exponentially into a large (almost 12γ), steadily increasing region; by 10.45.40 the spacecraft is well into the plasma sheet, thus, the plasma β is large (≃ 1), and warm plasma is certain to be present; this is also the region in which counter streaming flows are reported (Frank et al, 1979), thus instabilities such as the two-stream may also be important. However, this is well past the region of validity for the approximations with which we have computed the Alfvén mode.

Returning now to Figures 5.25, 5.29 and 5.33 which show the magnetic hodograms; much more information is available from these diagrams in addition to a test for plane geometry. On each of these figures an arc of a circle is drawn which is centred on the origin of coordinates. This is of value in time sequencing the plots, for example Fig.5.25, which corresponds to an exit from the plasma sheet, and is therefore best considered by working backwards in time. It shows that at about 10.21.00 the spacecraft encounter the plasma sheet boundary whereupon the magnetic pressure falls rapidly, while the plasma pressure increases, thereby causing the decrease in field strength. The close adherence to the circle is exhibited by all the hodograms as the spacecraft first sample the boundary, and it is this region which is the expected location of the Alfvén wave. Fig.5.29 again shows the sequence as the interchange between magnetic and plasma pressure occurs, however the difference here is that the spacecraft are being engulfed by the expanding plasma sheet and the overall appearance of the hodograms may be thought of in terms of the wave field of the Alfvén wave, at about 17.22.00, accelerating particles in a field-aligned direction, which in turn produce the increasing perturbation in the B_y component of the magnetic field, and upon encountering the plasma sheet proper, at about 17.22.50, the plasma pressure increases

and the magnetic pressure falls away while the $\underset{\sim}{B}_x$ component of the magnetic field settles down to a plasma sheet value of about 19γ (cf. Fig.5.26). However, one point to be noted is that the picture is really three dimensional, and for this reason the magnitude of $\underset{\sim}{B}_z$ is indicated at selected points on each hodogram.

As a final point in this subsection some mention must be made of the spatial scales which are relevant to these events, and this information can quite easily be obtained from the magnetic data. At this point in their orbit ISEE 1 and 2 are separated by a total distance of about 370 km, with a time separation of 250s; however the trace-time separation for day 94, Fig.5.27, is about 15s. This implies a boundary speed of around 25 km s^{-1}, a value which is consistent with observation.

Returning to Fig.5.27 and considering the field at 17.22.3 we see that ISEE 2 observes a different field orientation to ISEE 1, which has to go a distance equal to the y-coordinate separation of the spacecraft before it encounters the same field, by which time ISEE 2 is sampling a different field again; and hence until about 17.22.55 when both spacecraft see the same field. Thus by knowing the y-coordinate separation and the number of "steps" through the event we can estimate its size to be at least 1200 km, and as for this event $|\underset{\sim}{B}|$ was 30γ, and if the near earth field is taken as 50,000γ, a size of 1200 km at the plasma sheet boundary will map to about 30 km at ionospheric altitudes. In this context there are two points to be noted, firstly, that the size of the events is thin when compared to the boundary itself, which is of the order of 2500-3000 km (Andrews et al, 1980), and secondly that the ionospheric size is within the range of dimensions reported for the "inverted V" events (Mozer et al, 1980).

5.8 Discussion

Sections 5.2 through 5.7 have presented both theoretical and actual data plots, the latter of which confirm in part the predictions of linear theory, and enable a simple interpretation to be made for the events which were seen in the data.

It has been shown how the thin events seen in the boundary of the plasma sheet map to ionospheric sizes which correspond to the inverted V events, and while these are often of sizes of the order of 100 km they have been reported at very much smaller dimensions.

Returning to the computed plots shown in Figures 5.1 etc., for the $\underset{\sim}{B}_y$ component, as the abscissa is in units of $c/\omega p_e$, an estimate of the computed scale size can be made. This is achieved by making use of the formulae in section 5.2.1, and by considering a lobe density of 0.1 cm^{-3}. It is clear that we can consider a wide range of $\cos\theta$ values, and for $\cos\theta = 0.00999$ we can estimate an approximate scale size of about 800 km. While this is less than the observational size as deduced above it is still very much thinner than the plasma sheet boundary itself. The order of magnitude agreement between computation and observation does suggest that the model may have some physical significance.

Before summarising this chapter, a short section will be included on the subject of streaming plasma which has been reported on the boundary of the plasma sheet. While not directly associated with the work done here, it is possible, from the magnetic data examined, that some insight can be gained as to what processes are at work in this region of the magnetosphere.

5.9 Particle Beams and the Plasma Sheet Boundary Layer

Brief mention has already been made earlier in this chapter as to the existence of particle beams seen in the vicinity of the

boundary of the plasma sheet. However most authors have used plasma data to examine plasma sheet crossings, and at most supported these conclusions with only small amounts of magnetic data. It is often seen in such crossings that detached spikes of plasma can sit just outside the plasma sheet, separated by about 1-2 minutes from the main entry; mention was made above of corrugations which are frequently present on the boundary and such conditions are capable of explaining the presence of detached spikes. However a possible candidate for producing the vertical flapping of the plasma sheet is a transverse Alfvén wave, and if such a wave is present we may expect to see some kind of magnetic signature. If the wave is fast mode, such a signature, if it exists, should be present in the $\underset{\sim}{B}_z$ component.

The purpose of this sub-section is to consider briefly this possibility by examining suitable events for which we also have the plasma data.

a) Day 109

The period of interest is about 07.40 UT. At this time the spacecraft were situated at :

$x = -17.08\ R_e$

$y = 1.03\ R_e$ GSM coordinates

$z = 5.89\ R_e$

At this time the $\underset{\sim}{B}_x$ component of the magnetic field data indicates that the spacecraft briefly entered the plasma sheet (Fig.5.34-36), the $\underset{\sim}{B}_y$ component confirms the presence of a small system of field-aligned currents flowing towards the earth, as evidenced by the northward tilt of the field, which is seen from the positive $\underset{\sim}{B}_z$ component. Fig.5.37 shows the flux of high energy protons (E > 115 keV), from both ISEE 1

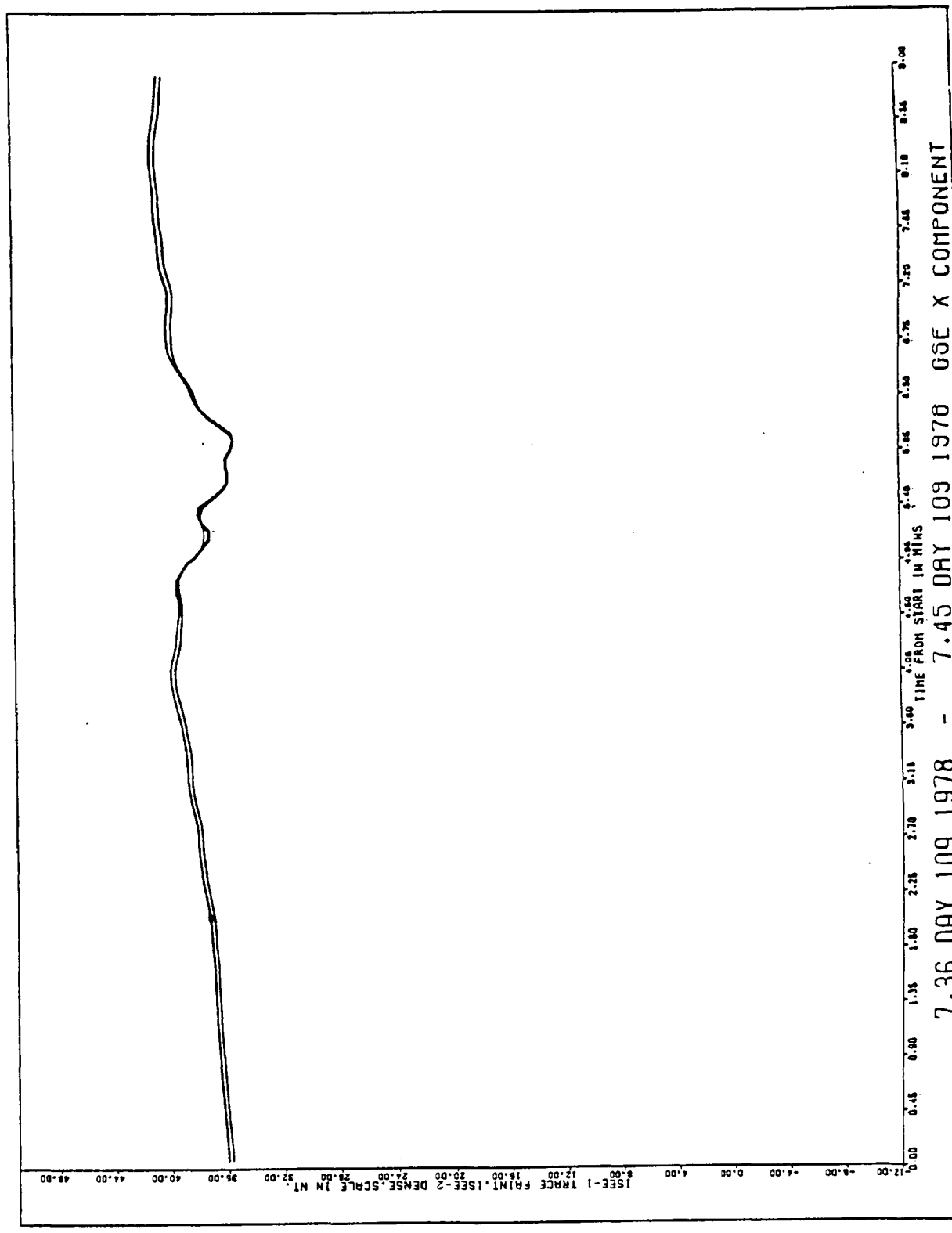

Figure 5.34 B_x for ISEE 1 and 2 for 07.36-07.45 on day 109 (plasma sheet encounter ≈ 07.39). ISEE 1 trace is faint.

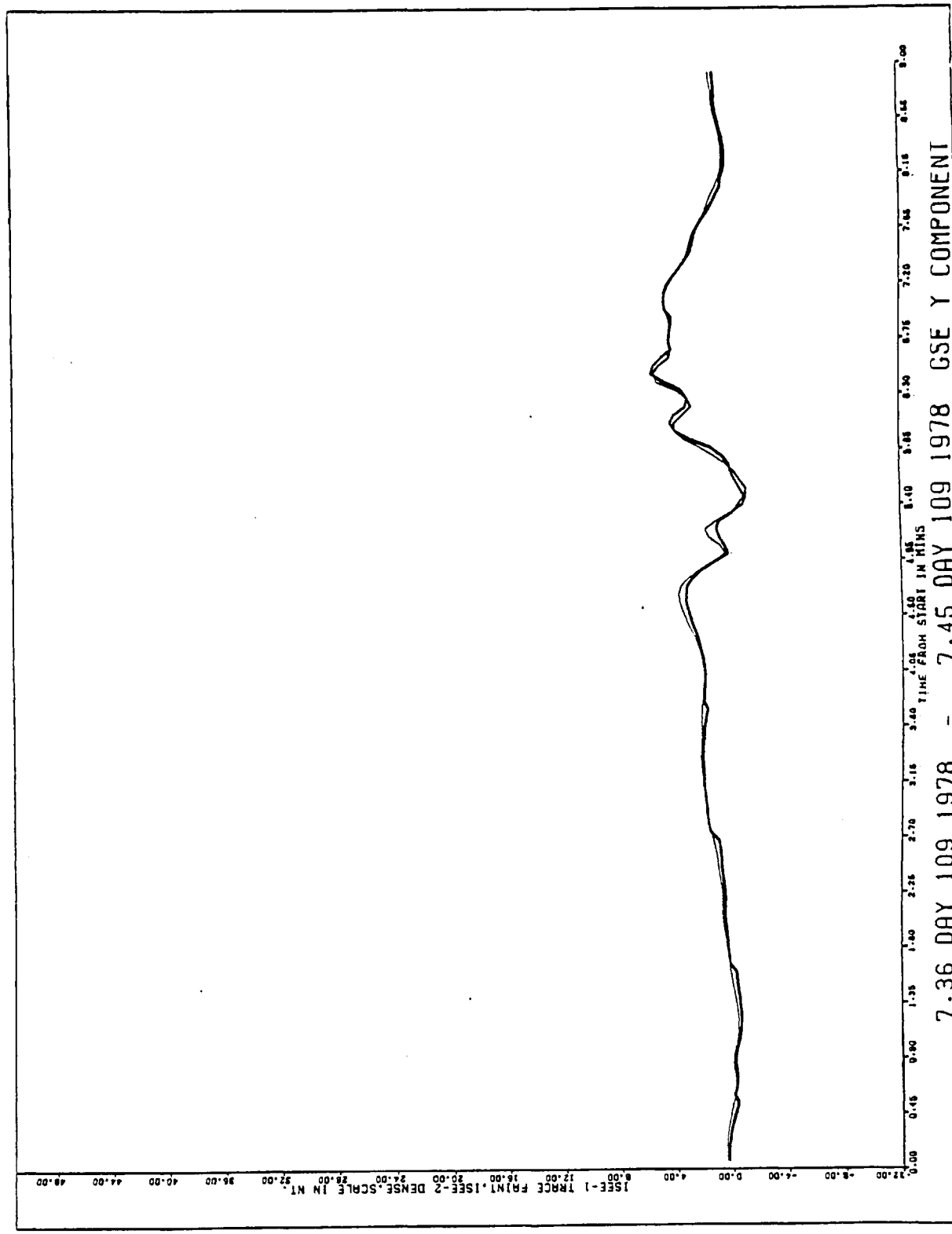

Figure 5.35 $\underset{\sim}{B}_y$ for ISEE 1 and 2 on day 109.

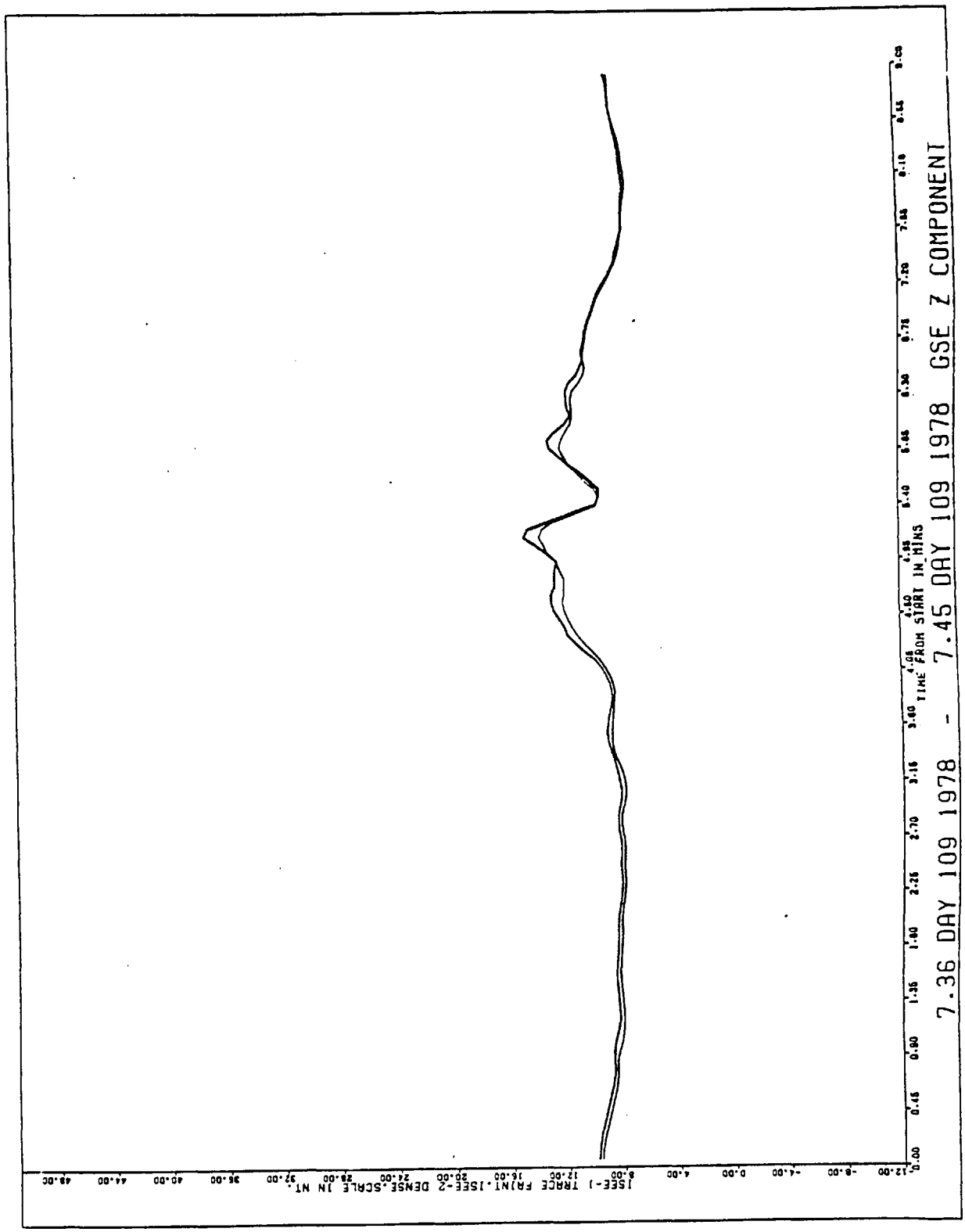

Figure 5.36 $\underset{\sim}{B}_z$ for ISEE 1 and 2 on day 109.

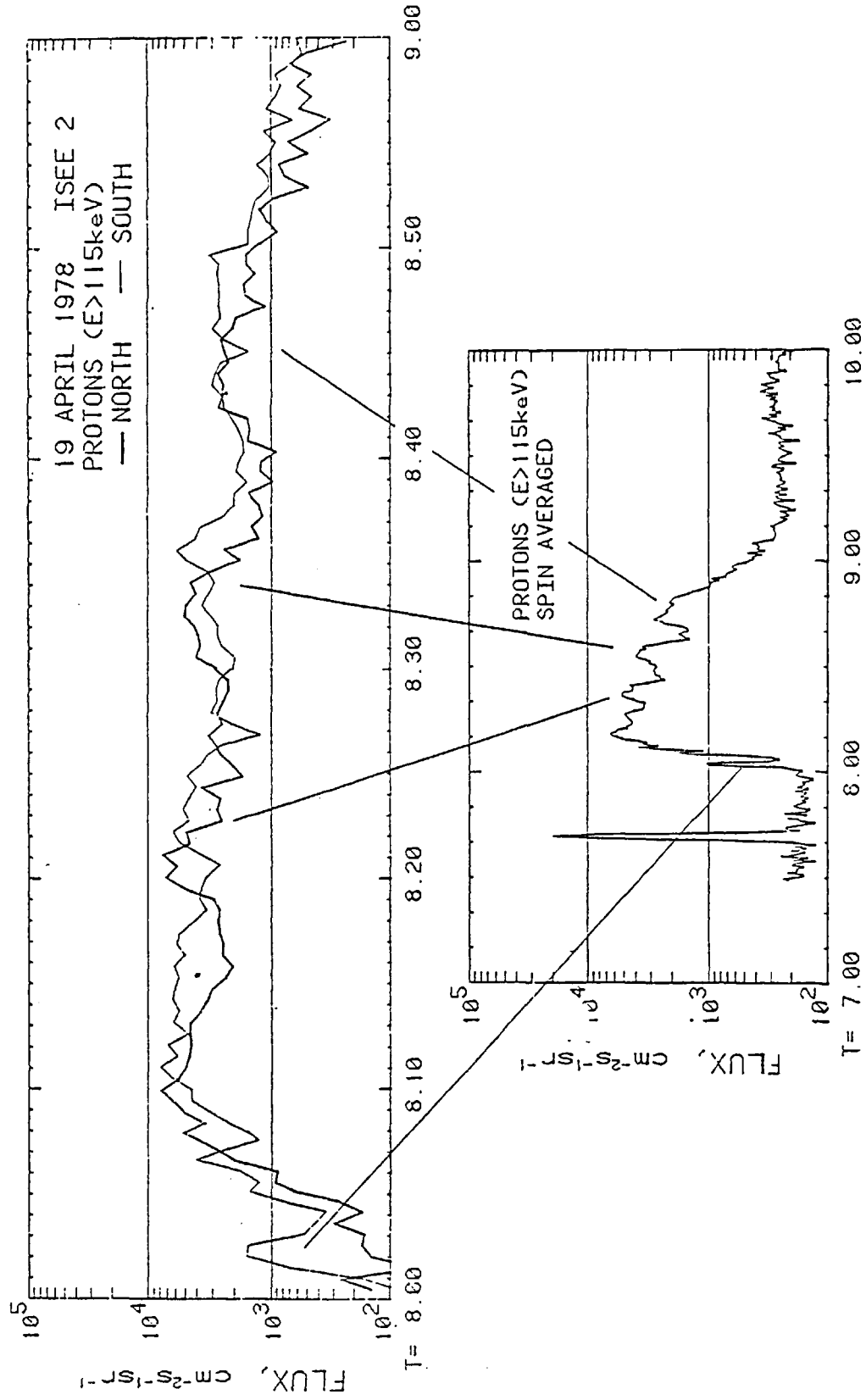

Figure 5.37 Proton flux data (energy > 115 keV) for day 109 (after Andrews et al, 1980).

and 2, and shows clearly the presence of a detached plasma spike at 07.42 UT which is clearly just prior to the main plasma sheet entry; simultaneously with this the $\underset{\sim}{B}_z$ component was seen to undergo a ± 4γ oscillation. It can also be seen that a second smaller spike occurred right on the boundary at about 08.02 UT. However, for this event there was hardly any significant change in either the $\underset{\sim}{B}_x$, $\underset{\sim}{B}_y$ or $\underset{\sim}{B}_z$ components.

The second example, which is slightly different in that the spike is seen to be attached to the boundary occurred on day 87.

b) Day 87

The time of interest is about 03.40 UT, however, during the whole of day 87 the spacecraft was seldom further than 8 R_e from the neutral sheet, and often as close as 1 R_e. It therefore encountered the plasma sheet on three distinct occasions, the first of which was at about 03.40 when the spacecraft were situated as follows :

$x = -20.00\ R_e$
$y = -3.60\ R_e$ GSM coordinates
$z = 7.40\ R_e$

Fig.5.38-40 show the magnetic data and are typical plasma sheet entries. Prior to the encounter ISEE 1 was unfortunately suffering some directional uncertainty, and the large negative pulse on entry is an artefact of the data, however ISEE 2 shows a decrease of some 4γ in the $\underset{\sim}{B}_x$ component while the $\underset{\sim}{B}_y$ component again registers the presence of a small current system flowing on the boundary. The next figure, Figure 5.41, again shows energetic proton flux, and it is clear that the spike at 03.42 UT coincides almost precisely with the boundary crossing. Looking now at the $\underset{\sim}{B}_z$ component, there is again a ± 4γ perturbation which comes out of a quiet field. This perturbation is

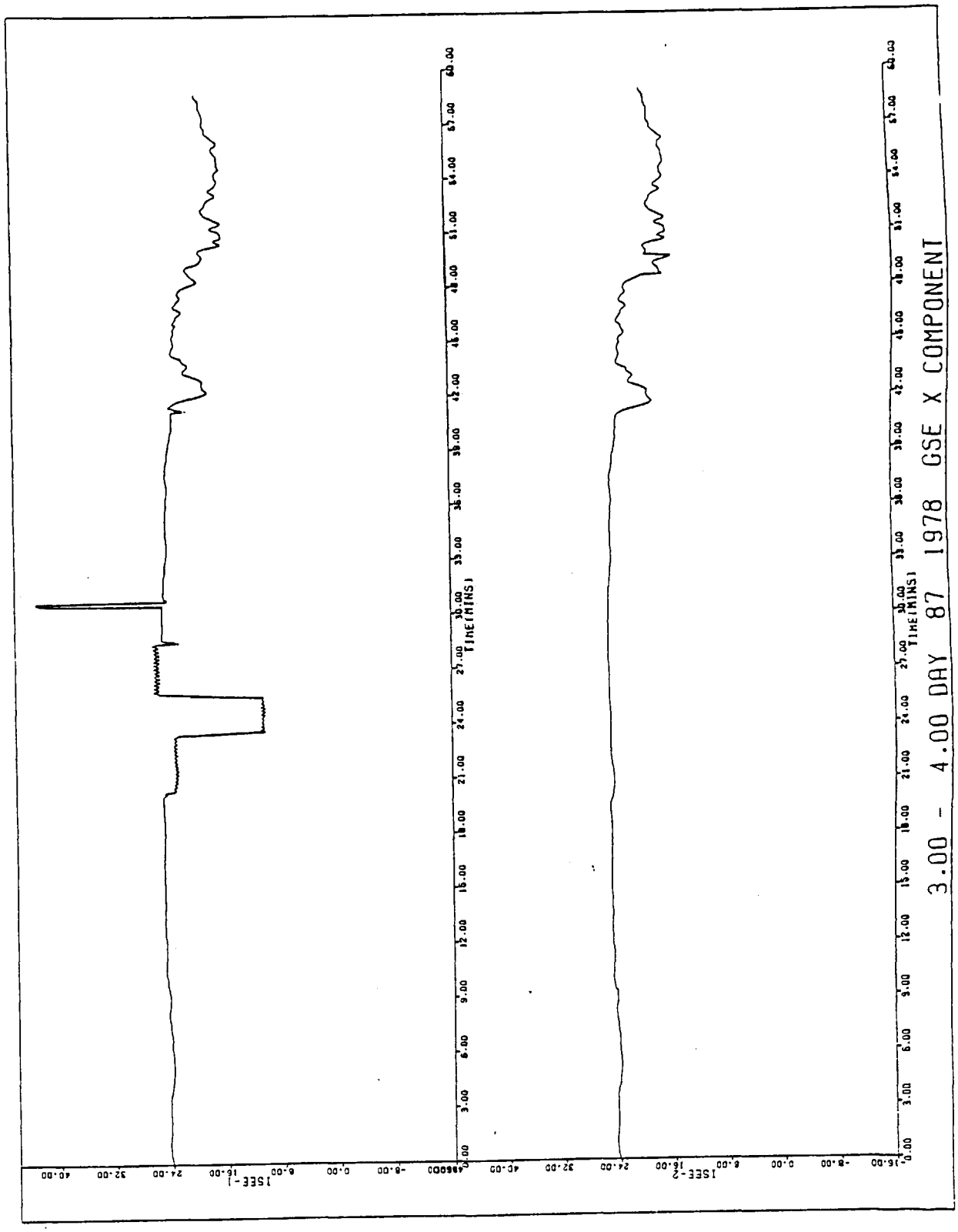

Figure 5.38 $\underset{\sim}{B}_x$ for 03.00-04.00 on day 87.

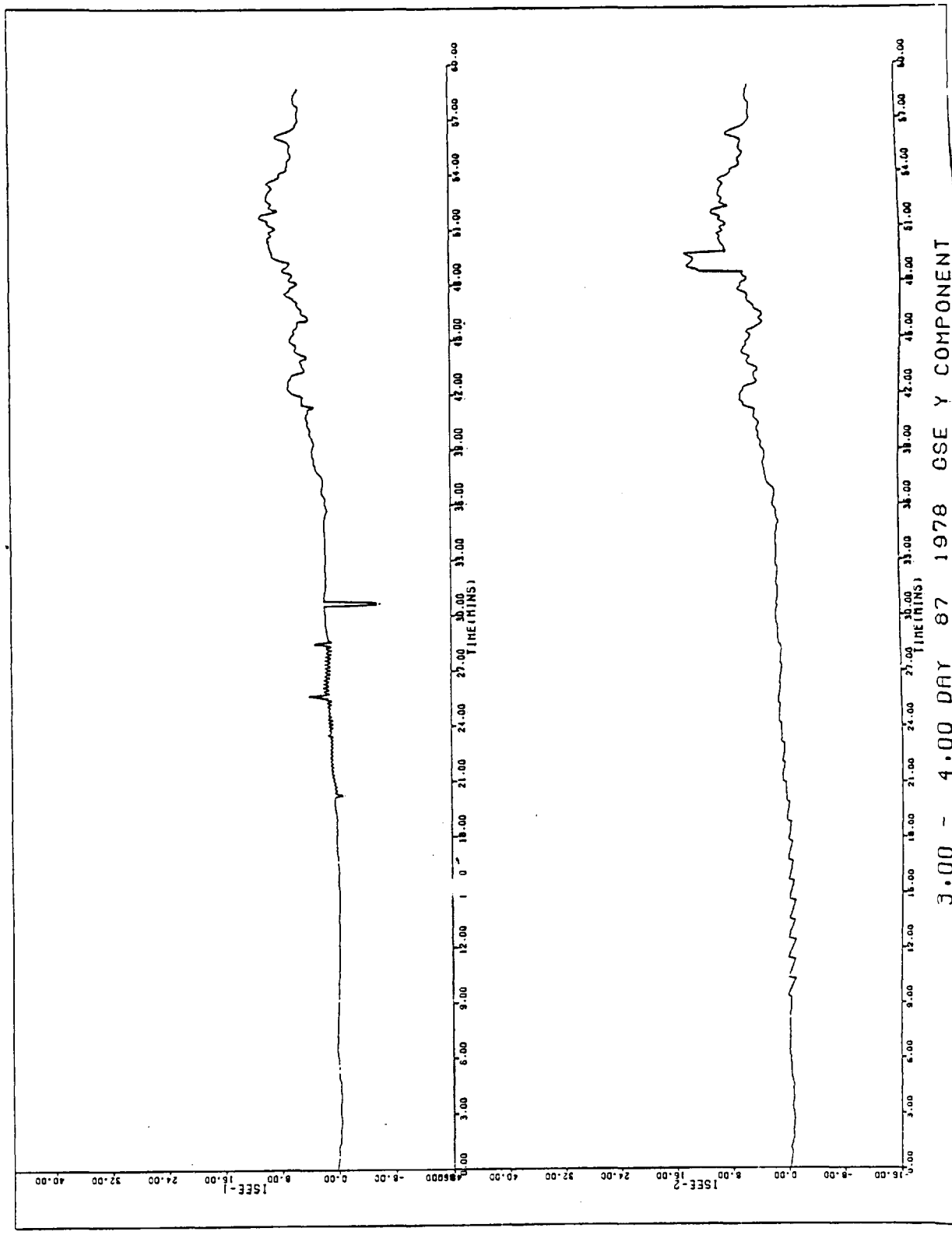

Figure 5.39 $\underset{\sim}{B}_y$ for 03.00-04.00; day 87.

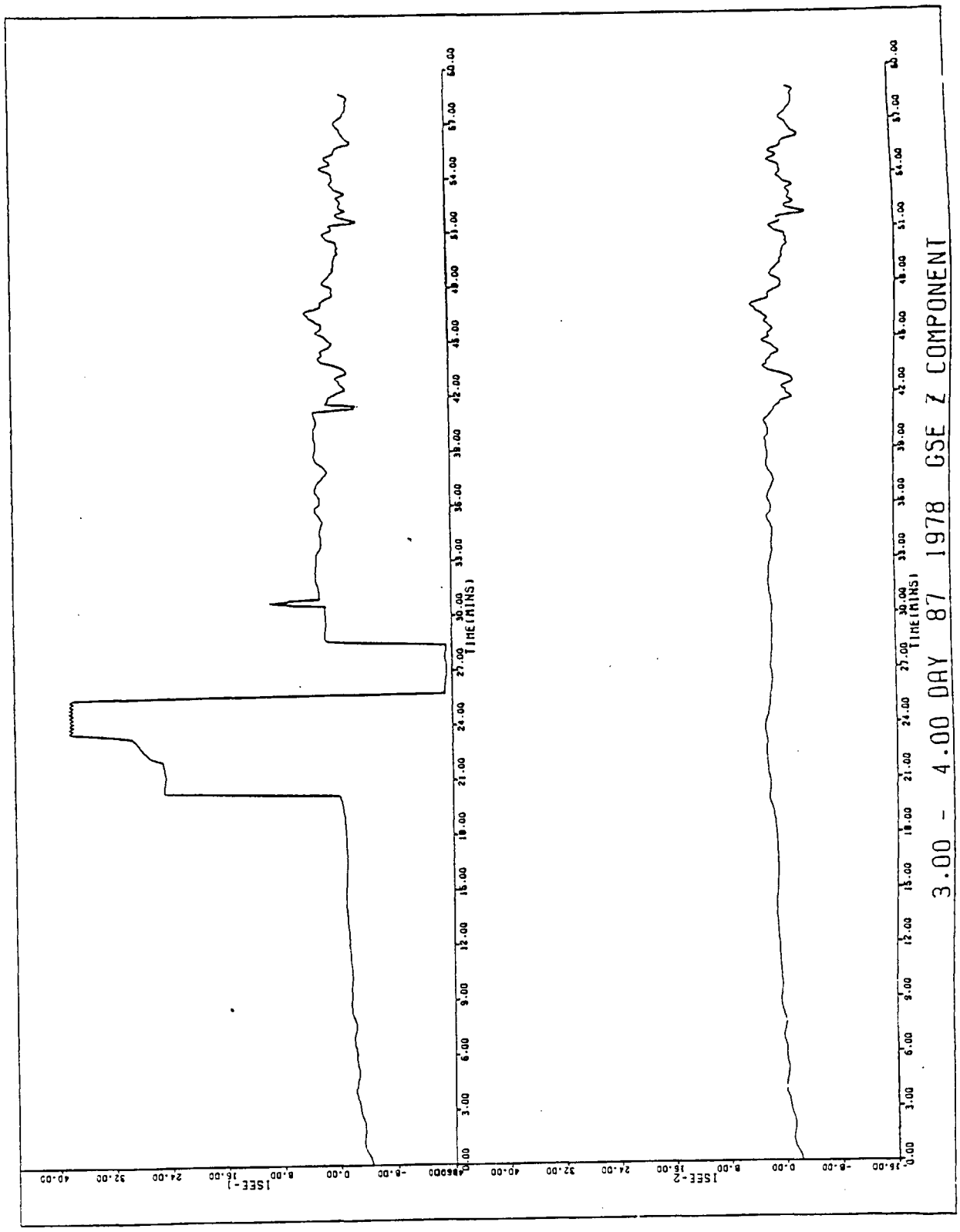

Figure 5.40 B_z for 03.00-04.00; day 87.

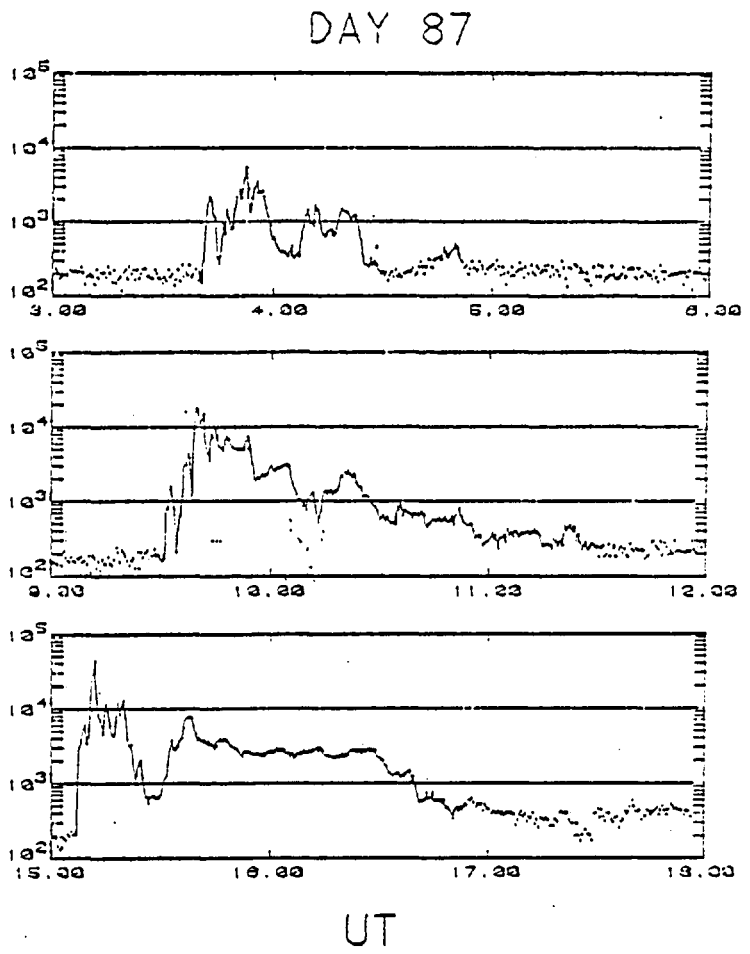

Figure 5.41 Proton flux data (as for Figure 5.37) for day 87 (after Andrews et al, 1980).

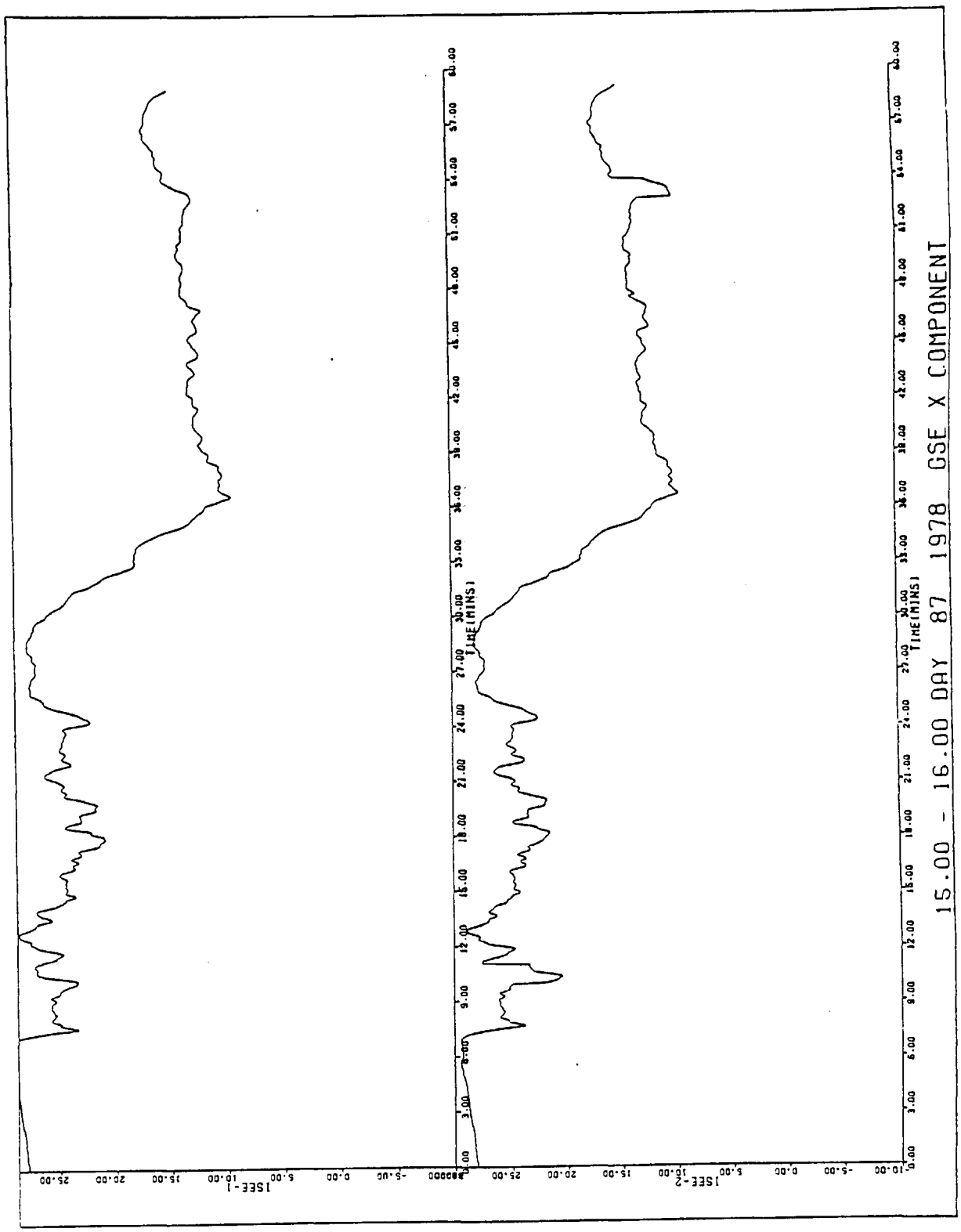

Figure 5.42 $\underset{\sim}{B}_x$ for 15.00-16.00 on day 87.

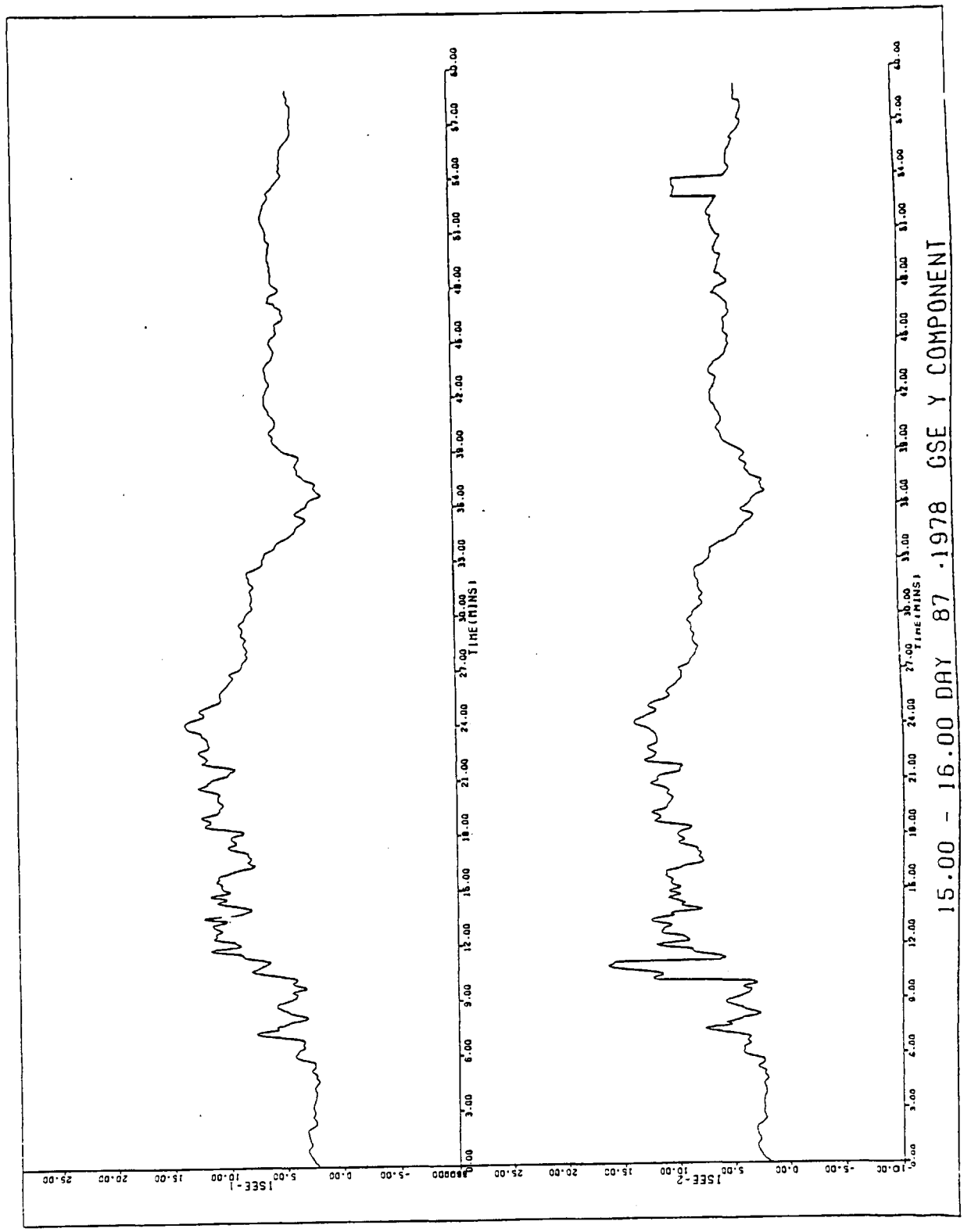

Figure 5.43 B_y for 15.00-16.00 on day 87.

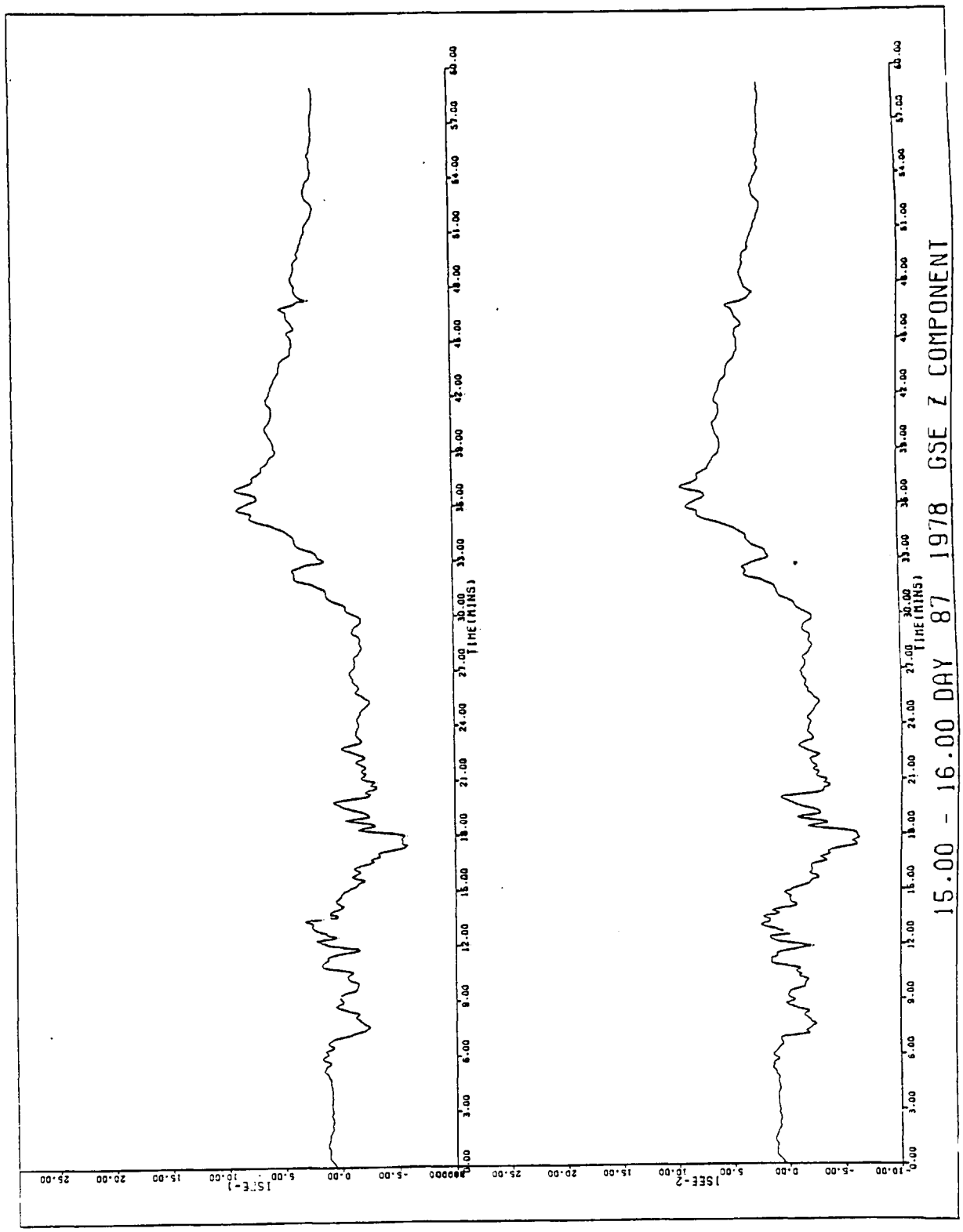

Figure 5.47 B_z for 15.00-16.00 on day 87.

centred on 03.42 UT and shows a "double humped" appearance similar to the plasma data.

A second example occurred at about 15.12 UT on day 87 (Figs.5.41 - 44), and this is seen again to correspond to the main plasma sheet boundary crossing. The plasma data shows a spike of flux which is clearly sitting on the boundary itself, and checking with the $\underset{\sim}{B}_z$ component, a sharp ± 5γ perturbation is seen; however it is not easy to associate this directly with the spike as the $\underset{\sim}{B}_z$ field displays a rather noisy character just before and after the perturbation, although it can be stated that both events occur almost simultaneously.

To conclude this sub-section, while three examples cannot be said to be conclusive evidence of a magnetic signature, and a more complete analysis would need to attempt a match between the periods of the magnetic fluctuations and the appearance and disappearance of the plasma sheet for many crossings, it can perhaps be said that Alfvén waves cannot be ruled out as a cause of vertical flapping of the plasma sheet.

As a final note, the small scale, local, north-south oscillations of the $\underset{\sim}{B}_z$ component are difficult to interpret, but because of the component in which they occur they could possible be related to loops of closed flux, caused perhaps by the tearing mode instability, Schindler (1974), and which are subsequently convected over the spacecraft. However, these beams are not the subject of this work, and the final sub-section serves to summarise sections 5.2 to 5.7.

5.10 Summary

The accuracy and success achieved when obtaining numerical solutions to differential equations is a function of several factors,

and to a large extent the characteristics of the equations concerned determine the type of algorithm which could be used. Section 5.1 discussed briefly the choice for solving the equations which were relevant to this work, while the subsequent two sections presented typical solutions for a range of parameters. Special reference was made to the growth rate and its relationship to the magnitude of the angle θ. Following from the approximations derived towards the end of Chapter 4, it was seen in these sections how the validity of these approximations changed as the non-linear effects assumed an increasingly important role, finally reaching a point where the computation could no longer be relied upon to give accurate predictions.

Section 5.5 gave an introduction to the ISEE mission and extended the discussion of the plasma sheet given in Chapter 1, while the following two sections discussed selected events in relation to the computer predictions. Also mentioned both here and in the discussion (section 5.8), was the relationship between the dimensions of these events and the inverted V's.

Finally, section 5.9 discussed the possibility of a magnetic signature which may be present when plasma spikes are seen both on, and separated from the plasma sheet boundary. The presence of $\underset{\sim}{B}_z$ component field fluctuations suggested a possible explanation for the flapping of the boundary region in terms of fast mode Alfvén waves.

CHAPTER 6

SUMMARY AND DISCUSSION

6.1 Results for the Model and their Magnetospheric Relevance

The contents of the previous chapter resulted entirely from a computation of the cold plasma equations. This was done subject to the observational constraint that the Alfvén Mach number, M_A, be very much less than one; and a value of $M_A = 0.01$ was chosen based on the $\underset{\sim}{E} \Lambda \underset{\sim}{B}$ drift velocity and the Alfvén speed at about 20 R_e down tail.

In the case of $b_y > 0$, the computation led to the discovery of non-linear effects which cause the perturbation to increase at a constant rate. This is the "straight line" region of the computed b_y plots and is exhibited by all the plots, regardless of the value of $\cos\theta$. However $\cos\theta$ is the crucial parameter in determining the growth rate of the waves and the maximum value reached by the perturbation.

In the case of $b_y < 0$ the situation is less simple to describe, but departure from the linear exponential region still occurs at the corresponding value of w. It was found necessary to devise approximations which would ensure that the pure Alfvén mode only was computed, and these were obtained by neglecting $db_z/d\tau$ and $dv/d\tau$, however upon reaching the non-linear region a modification was required which involved basing the approximations on the straight line part of the plot. In both cases, for $b_y > 0$, and $b_y < 0$, the approximations are valid and break down only when the field has undergone an appreciable

rotation, which physically corresponds to b_y becoming an appreciable fraction of b_z. Computationally progress could still be made by introducing an angular variable for the field, however observationally it would be meaningless as generally $b_y < b_z$

Interpretation of the magnetic and velocity plots was made in terms of constant current, and an exploratory search of ISEE 1 and 2 magnetometer data for selected plasma sheet crossings was made on the basis of model predictions. Events were shown and discussed, which were in gross agreement with the results of computation, and phenomena which had ionospheric scale sizes of the order of inverted 'V' events were shown to results when the mapping to ionospheric altitudes was done. As the cold plasma equations were computed on the assumption of plane geometry it was necessary to test this hypothesis for each of the plasma sheet events.

It turns out that the magnetic hodogram, a plot of $\underset{\sim}{B}_y$ against $\underset{\sim}{B}_x$, is a useful device for achieving this test while at the same time enabling insight to be gained as to the physical processes at work. By examining such hodograms a point can be found where the plasma pressure begins to rise at the expense of the magnetic, this causes the field to decrease as the spacecraft goes deeper into the plasma sheet boundary, which is physically equivalent to a rise in temperature of the plasma and hence the onset of warm plasma effects.

It was found that in the majority of plasma sheet encounters the direction of the $\underset{\sim}{B}_z$ component is predominantly northward, with some small variation, and is thus in qualitative agreement with the requirements of the Petscheck model (Petschek, 1964), the essential point of which was the suggestion that the flow of a conducting incompressible plasma in the convection region surrounding an X-type neutral line should involve an exchange process involving field and

flow energies which occurs across a standing shock wave.

As for the model, which is essentially for an Alfvén wave, which is standing between the earth and a source region located at a distance of 20 - 30 R_e down tail. The gross features of the model require only the existence of a strong electric field which exerts its influence across a thin layer, and the justification of this field in terms of the Alfvén-Dungey-Cowley model, given in Chapter 1, was shown to be equivalent to the justification of the existence of such a standing wave. That the wave is able to stand in such a low Mach number flow is clearly seen from cold plasma theory, where $\cos\theta < M_A$, thus for this value of M_A, viz. 0.01, the angle is close to 90^o. Under these circumstances the wave, with its wavefront almost parallel to the magnetic field and with a substantial field-aligned component of current, is able to stand in the flow. This therefore permits a plausible explanation of the small scale field-aligned currents, which are observed to flow in the auroral zone, in terms of the standing shear mode Alfvén wave.

Furthermore, as such a wave propagates past a given altitude the field increases and the current density rises. At this point the finite inertia of the electrons requires a parallel electric field to be set up and for an $\underset{\sim}{E}_{\parallel}$ of 0.1 to 0.2 mvm^{-1} a cold electron population can be accelerated to the critical velocity whereupon electrostatic ion cyclotron turbulence sets in. Such acceleration can occur in milliseconds, which is much less than the period of the Alfvén waves, and Kindel and Kennel (1971) have shown that this instability can be current driven; whereas Hudson and Mozer (1978b) have shown a positive correlation between the location of such turbulence and the inverted 'V' events.

For the case of the model, we can estimate the magnitude of

$\underset{\sim}{E}_x$ from the following expression :

$$E_x = \frac{vB_o}{10^3} \text{ mvm}^{-1}$$

which for a lobe field of 15γ produces an $\underset{\sim}{E}_x$ of 0.15 mvm^{-1}. This is for the linear region and while it is fairly low it is within the range of observation.

6.2 Discussion

In Chapter 1 it was shown that upon reflection from the ionosphere the presence of the $\underset{\sim}{E} \wedge \underset{\sim}{B}$ convecting plasma in general assures that reflected waves return to a position which is well downstream from the original source. A consequence of the convection of the reflected wave away from the path of the incident, is the production of a pair of oppositely directed electric fields which exist above the ionospheric structure. Since the conductivity of the ionosphere is high the wave should lose little of its amplitude during reflection, thus as the field lines are closed, many transits through the magnetosphere may occur. However, as the wave propagates earthwards the cross-section of the flux tube in which it travels undergoes a change in cross-section. This effect, which is essentially geometrical in character, may have the effect of influencing the magnitude of the electric field and also the current, when the effect is mapped to ionospheric altitudes.

Another potentially more serious effect which may have an effect on the stability of the system, arises from local variations in density which can occur along the flux tube, thereby giving rise to small reflected waves before the ionosphere is reached. For low frequency waves the characteristic propagation speed is just the

Alfvén speed, and is given numerically by :

$$V_A = 22 \frac{B(\gamma)}{(n)^{\frac{1}{2}}} \text{ km s}^{-1}$$

and is therefore a function of field strength and number density, both of which increase earthwards. This implies that the value of M_A will change as the earth is approached, thus the calculations would require repeating for a different value of M_A than that used for $\sim 20\ R_e$. However the order of magnitude is unlikely to change by a significant amount. Mallinckroot and Carlson (1978) gave an expression for the magnitude of the ionospheric field-aligned current which showed that it is essentially a function of the incident wave magnitude, viz.

$$I_{\parallel} = \frac{- 2\Sigma_M(\lambda_o)\Sigma_p \underset{\sim}{E}_D}{\Sigma_M(\lambda_o) + \Sigma_p}$$

where $\Sigma_M(\lambda_o)$ is the mapped flux tube conductivity just above the ionosphere, Σ_p is the height integrated Pedersen conductivity and $\underset{\sim}{E}_D$ is the electric field of the incident Alfvén wave.

We can generally assume that $\Sigma_p >> \Sigma_M(\lambda_o)$, hence we have :

$$I_{\parallel} \approx - 2\Sigma_M(\lambda_o) \underset{\sim}{E}_D \qquad 6.1$$

where a typical value of $\Sigma_M(\lambda_o) \approx 0.15$ mho. Similarly, the ionospheric electric field is given by :

$$\Delta\underset{\sim}{E} = \frac{2\Sigma_M(\lambda_o)}{\Sigma_M(\lambda_o) + \Sigma_p} \underset{\sim}{E}_D \approx \frac{2\Sigma_M(\lambda_o)}{\Sigma_p} \underset{\sim}{E}_D \qquad 6.2$$

which shows that the ionospheric electric field is just that which is necessary to close the current with the local value of Σ_p. Also we see

that the electric field in the magnetosphere is larger than that in the ionosphere by a factor of $\Sigma_p/2\Sigma_M(\lambda_o)$.

Equations 6.1 and 6.2 illustrate two important features, firstly that the magnitude of the sheet current is directly proportional to the mangitude of the electric field of the incident Alfvén wave; and secondly if we use equations 6.1 and 6.2, we obtain an expression for the ratio of the current to the electric field, viz.

$$\frac{I_{\perp}}{\Delta \underset{\sim}{E}} = -\Sigma_p$$

Viewed in this context the wave nature of the auroral zone field-aligned current is apparent.

6.3 Conclusions and Suggestion for Further Work

The most obvious feature which is absent from the computed plots is the saturation of the b_y perturbation, the consequence of which would be the settling at a higher state of the magnetic field, i.e. a true collisionless shock. It was suggested in Chapter 5 that the inclusion of a pressure would not be sufficient to model this effect, and attention should now be given as to a possible course of action. In this region of the plasma sheet, β is increasing rapidly. The spacecraft pass from a cold to a hot plasma regime in a few minutes (at most) of time. The most likely course would be to use a kinetic approach, which is essentially a Vlasov-Maxwell formulation, but to include a term which has its origin in the microturbulence inside the wave. This would involve writing the Vlasov equation as follows :

$$\frac{\partial f}{\partial t} + \underset{\sim}{V}.\frac{\partial f}{\partial x} + \frac{e}{m}\{\underset{\sim}{E} + \underset{\sim}{V} \Lambda \underset{\sim}{B}\}.\frac{\partial f}{\partial V} = 0 \qquad 6.3$$

and then assuming that the distribution function and the electric and magnetic fields behave as follows :

$$f = f_o + \delta f, \qquad \underset{\sim}{E} = \underset{\sim}{E}_o + \delta\underset{\sim}{E}, \qquad \underset{\sim}{B} = \underset{\sim}{B}_o + \delta\underset{\sim}{B}$$

where subscript 'o' refers to the zeroth order and '∂' is the fluctuating portion.

Averaging 6.3 gives :

$$\frac{\partial f_o}{\partial t} + V.\frac{\partial f_o}{\partial x} + \frac{e}{m}\{\underset{\sim}{E}_o + \underset{\sim}{V} \Lambda \underset{\sim}{B}_o\}.\frac{\partial f_o}{\partial \underset{\sim}{V}} = C(\delta f)$$

where $C(\delta f) = -\frac{e}{m}\{(\delta\underset{\sim}{E} + \underset{\sim}{V} \Lambda \delta\underset{\sim}{B}).\frac{\partial \delta f}{\partial \underset{\sim}{V}}$ and is sometimes referred to as the 'stoss'. This quantity plays the role of a collision term in that it contributes to changes in the values of f_o etc., as a result of interactions between the fluctuating quantities. The quantity $C(\delta f)$ therefore depends entirely on momentum and energy transfer which goes back and forth between the fluctuating fields.

While this approach should describe the behaviour in a more accurate fashion there are still the usual problems of deciding on suitable expressions for f_o, as well as closing the equations by deciding on the form of the fluctuations in $C(\delta f)$. However, in practice simplification is possible and $C(\delta f)$ is often approximated by an expression of the form : $-\upsilon(\underset{\sim}{V}_e - \underset{\sim}{V}_i)$ where $\underset{\sim}{V}_e$, $\underset{\sim}{V}_i$ are velocities of electrons and ions respectively and υ is a constant.

While this approach, although complex, might prove its worth in the longer term, the model used in this work is still capable of extension. The most obvious extension follows from the observation in the previous chapter that the approximations to the Alfvén mode break down for both cases considered, viz. $b_y > 0$ and $b_y < 0$, when

the field has undergone a rotation of a few radians or less. This implies that b_y is becoming an appreciable fraction of b_z thus by introducing an angular field variable would enable the calculation to proceed further. However, as was pointed out in Chapter 5 this would have little meaning observationally.

A more desirable procedure would be to perform a fully time dependent analysis. In Chapter 4, which dealt with the computation it was stated that one of the principal boundary conditions was the restraint on the x-component of the velocity, i.e. u, not to change sign. If the calculation was performed with $\partial/\partial t \neq 0$ this restraint could be relaxed. This however would lead to instability problems as the physical consequence of relaxing this condition is to permit the particles which are accelerated by the wave to reverse direction. This in turn would lead to the growth of two stream instability.

As a final word of conclusion, the model in its present form is both plausible and realistic in its predictions for the linear, and part of the non-linear behaviour of the shear-mode Alfvén wave and its application to explaining small scale auroral zone field-aligned currents. It successfully predicts non-linear features which are visible in part in spacecraft data. However, if extensions were made to the model on the lines of the above suggestions a more complete description should be possible.

Ultimately, the characteristics of the plasma sheet itself must determine the approach to the problem. In view of the presence of what are often substantial corrugations on the plasma sheet boundary, the dimensionality of the problem would need to be increased. Finally, the concept of a normal to the plasma sheet boundary would need to be defined with some precision.

REFERENCES

Alfvén, H., 1939, *A Theory of Magnetic Storms*, I. Kungl. SV. Vet-Akademiens Handl. (3), 18, No.3.

Alfvén, H., 1950, *Cosmical Electrodynamics*, OUP.

Alfvén, H. 1968, J. Geophys. Res., 73, 4379.

Akasofu, S.I., Hones, E.W., Montgomery, M.D., Bame, S.J. and Singer, S., *Association of magnetotail phenomena with visible auroral features*, JGR, 76, 5985, 1971.

Akasofu, S.I. and Chapman, S., 1972, *Solar Terrestrial Physics*, Clarendon Press.

Akhiezer, A.I., Akhiezer, I.A., Polovin, R.V., Sitenko, A.G. and Stepanov, K.N., 1975, *Plasma Electrodynamics*, Pergamon Press, Oxford.

Anderson, H.R. and Vondrak, R.R., 1975, Rev. Geophys. Space Phys., 13, 243.

Andrews, M.K., Keppler, E., Daly, P.W., *Plasma sheet motions inferred from medium-energy ion measurements*, Preprint, December 1980.

Arnoldy, R.L., 1974 Rev. Geophys. Space Phys., 12, 217.

Bame, S.J., Asbridge, J.R., Felthauser, H.E., Hones, E.W. and Strong, I.B., 1967, *Characteristics of the plasma sheet in the Earth's magnetotail*, J. Geophys. Res., 72, 113.

Birkeland, K., 1913, *The Norwegian Aurora Polaris Expedition 1902-1903*, vol.1, H. Aschehoug Christiania.

Bohachevsky, I.O., 1962, Phys. Fluids, 5, 1456.

Carbary, J.F., Krimigis, S.M., *Energetic particle activity at 5 min and 10 s time resolution in the tail and associated phenomena*, JGR, 84, 7123, 1979.

Chapman, S. and Ferraro, V.C.A., 1931, *A new theory of magnetic storms*, Terr. Mag. Atmosph. Elect., 36, 77.

Chen, L. and Hasegawa, A., 1974, J. Geophys. Res., 79, 1624.

Cloutier, P.A., Anderson, H.R., Park, R.J., Vondrak, R.R., Spiger, R.J. and Sandel, B.R., 1970, *Detection of geomagnetically aligned currents associated with an auroral arc*, J. Geophys. Res., 75, 2595.

Coroniti, F., Frank, L., Williams, D.J., Lepping, R., Scarf, F., Krimigis, S. and Gloeckler, G., *Variability of plasma sheet dynamics*, JGR, 85, 2957, 1980.

Cowley, S.W.H., 1971, Cosmic Electrodyn., 2, 90.

De Coster and Frank, 1979, *Observations pertaining to the plasma sheet*, JGR, 84, 5099.

Dungey, J.W., 1961, *Interplanetary magnetic field and the auroral zones*, Phys. Rev. Lett., 6, 47.

Dungey, J.W., 1965, *The length of the magnetospheric tail*, JGR, 70, 1753.

Dungey, J.W., 1975, *Acceleration processes in the plasma sheet*, reprint.

Fairfield, D.H., *Magnetic field signatures of substorms on high-latt field lines in the nighttime magnetosphere*, JGR, 78, 1553, 1973.

Feldstein, Y.I., 1963, *Some problems concerning the morphology of auroras and magnetic disturbances at high latitude*, Geomag. Aeronom., 3, 183.

Frank, L.A. et al, 1976, JGR, 81, 5859.

Frank, L.A., De Coster, R.J., 1978b, Space Sci. Rev., 22, 739.

Frank, L.A. et al, 1979, *Field-aligned currents in the Earth's magnetotail*, Preprint.

Frank, L.A., McPherron, R., De Coster, R., Burek, B., Ackerson, K. and Russell, C.T., *Field-aligned currents in the Earth's magnetotail*, Preprint, Jan. 1980.

Gurnett, D.A., Frank, L.A. and Lepping, R.P., 1976, JGR, 81, 6059.

Gurnett, D.A. and Frank, L.A., 1977, JGR, 82, 1031.

Herlofson, N., 1950, Nature, 165, 1020.

Hones, E.W., Asbridge, J.R., Bame, S.J., Montgomery, M.D., Singer, S. and Akasofu, S.I., *Measurements of magnetotail plasma flow with Vela 4B*, JGR, 77, 5503, 1972a.

Hones, E.W., 1977, *Substorm processes in the magnetotail (Fireballs and Boundary Layers)*, JGR, 82, 5633.

Hudson, M. and Mozer, F., 1978a, *Electrostatic shocks, double layers and anomalous resistivity in the magnetosphere*, Geophys. Res. Lett., Feb. 1978.

Hudson, M. and Mozer, F., 1978b, *Magnetic field-aligned potential drops due to electrostatic ion cyclotron turbulence*, Geophys. Res. Lett., Feb. 1978.

IIjima, T. and Potemra, T.A., 1976a, JGR, 81, 2165, 1976.

IIjima, T. and Potemra, T.A., JGR, 81, 5971, 1976.

Kamide, Y. and Akasofu, S.I., 1976, JGR, 81, 3999.

Kamide, Y. and Rostocker, G., 1977, JGR, 82, 5589.

Kamide, Y., Murphree, J.S., Anger, C.D., Berkey, F.T. and Potemra, T.A., 1978 (submitted to JGR).

Kindel and Kennel, G., 1971, *Topside current instabilities*, JGR, 76, 3055.

Landau, L.D. and Lifshitz, E.M., 1959, *Fluid Mechanics*, Pergamon Press, Oxford.

Lui, A.T.Y. et al, 1977, JGR, 82, 1235.

Mallinckroot, A.J. and Carlson, C.W., 1978, *Relations between transverse electric fields and field-aligned currents* J. Geophys. Res., 83, 1426.

Meng, C. and Anderson, K., *Energetic electrons in the plasma sheet out to 40 Re*, 1971, JGR, 76, 873.

Möbius, E., Ipavich, F.M., Scholer, M., Gloeckler, G., Hovestadt, D. and Klecker, B., 1980, *Observations of a non-thermal ion layer at the plasma sheet boundary during substorm recovery*, JGR, 85, 5143.

Mozer, F.S., Cattell, C.A., Hudson, M.K., Lysak, R.L., Temerin, M. and Torbert, R.B., 1980, *Satellite measurements and theories of low altitude auroral particle acceleration*, Preprint, but see Hudson and Mozer, 1978a,b and references therein.

Parker, E.E., *Interaction of the solar wind and the geomagnetic field*, Phys. Fluids, 1, 171, 1958.

Parks, G., Lin, C.S., Anderson, K.A., Lin, R.P. and Réme, R., *ISEE I and II particle observations of the outer plasma sheet boundary*, JGR, 84, 6471, 1979.

Petschek, H.E., 1964, AAS-NASA Symp. on the Physics of Solar Flares (ed. W.N. Hess, NASA SP-50, 425).

Potemra, T.A. and Saflekos, N.A., 1978, Preprint. Also Proc. of the Int. Symp. on Solar-Terrestrial Physics, Innsbrück, Austria, 1978.

Russell, C.T., *The ISEE 1 and 2 fluxgate magnetometers*, IEEE Trans. Geosci. Elec., 16, 239, 1978.

Sagdeev, R.Z., 1962, Soviet Phys. Tech. Phys., 6, 867, 1962.

Southwood, D.J., 1974, Planet. Space Sci., 22, 483.

Southwood, D.J., 1978, *Plasma waves in the magnetosphere*, Reprint from Nature, vol.271, No.5643, pp.309-316.

Speiser, T.W., 1965, JGR, 70, 4219, 1978.

Spjeldvik, W.N., Fritz, T.A., *Energetic ion and electron observations of the geomagnetic plasma sheet boundary layer : 3-D results from ISEE 1*, June 1980, in press.

Schindler, K. 1974, *A Theory of the substorm mechanism*, JGR, 79, 2803.

Swift, D., 1976, *Formation of auroral arcs and acceleration of auroral electrons*, JGR, 81, 3935.

Thomas, B.T. and Hedgecock, P.C., 1975, *Substorm effects on the neutral sheet inside 10 Earth radii*, published in *The Magnetospheres of the Earth and Jupiter*, D. Reidel Publishing Company, Vol.52, 1975.

Tidman, D.A. and Krall, N.A., 1971, *Shock waves in collisionless plasmas*, Wiley Interscience.

Zmuda, A.J. and Armstrong, J.C., 1974a, *The diurnal variation of the region with vector magnetic field changes associated with field-aligned currents*, JGR, 79, 2501.

Zmuda, A.J. and Armstrong, J.C., 1974b, *The diurnal flow pattern of field-aligned currents*, JGR, 79, 4611.

Dixon, V.A. and Woods, L.C., *Structure of oblique hydromagnetic shock waves*, Plasma Physics, 18, 627, 1975.

Cordey, J.G. and Saffman, P.G., *The structure of quasi shocks in a magnetised collison-free plasma*, J. Plasma Physics, 1, 129, 1966

Saffman, P.G., *On hydromagnetic waves of finite amplitude in a cold plasma*, J. Fluid Mech., 11, 552, 1961.

Kellogg, P.J., *Solitary waves in a collisionless plasma*, Physics of Fluids, 7, 1555, 1964.

LIST OF ESSENTIAL NOMENCLATURE

Chapter 1

j	Current density
$j_{\parallel}$	Parallel current density
$\underset{\sim}{B} = (\underset{\sim}{B}_x, \underset{\sim}{B}_y, \underset{\sim}{B}_z)$	Magnetic field components
λ_p	The proton wavelength
n	Particle number density
$\underset{\sim}{E} = (\underset{\sim}{E}_x, \underset{\sim}{E}_y, \underset{\sim}{E}_z)$	Electric field components
V_A	The Alfven speed
M_A	The Alfven Mach number
Ω_p	Proton gyrofrequency
Ω_e	Electron gyrofrequency
ω	Angular frequency
k	Wave number
$w = \omega/k$	Phase velocity

Chapter 2

a_i	Hydromagnetic state vector
P	Particle pressure
ε	$\pm$, depending on particle species
υ, υ_m	Hydromagnetic and magnetic viscosities
ΔP etc.	Change in parameter across a discontinuity

Chapter 3

m_p, m_e	Proton and electron masses
σ	Temporal growth rate
K	Spatial growth rate
$V_{\parallel}$	Parallel, (field-aligned) velocity
$V_{\perp}$	Perpendicular velocity

Chapter 4

f	Particle distribution function
L	Liouville operator
$\gamma = m_p/m_e$	Mass ratio
$\tau = x\ \omega_{pe}/c$	De-dimensionalising parameter
ω_{pe}	Electron plasma frequency

Chapter 5

R_e	Earth radii
BPS	Boundary of the plasma sheet
CPS	Central plasma sheet
γ(nt)	Equivalent to nano teslas (nt) - unit of magnetic field measurement

Chapter 6

$I_{\parallel}$	Parallel component of current
$\Sigma_m(\lambda_o)$	Mapped flux tube conductivity
Σ_p	Height integrated Pedersen conductivity

APPENDIX A

ERROR ANALYSIS FOR THE EULER ALGORITHM

The Euler algorithm was discussed briefly in the first section of Chapter 5, together with a somewhat arbitrary mention of possible sources of error which may occur during the course of a computation which is based on this particular algorithm. The purpose of this appendix is to quantify the errors which are usually involved.

In its most general form the one-step method may be written as follows :

$$y_{i+1} = y_i + h\,\phi\,(x_i, y_i; h), \quad i = 0, 1, \ldots, n-1 \qquad \text{A.1}$$

Equation A.1 is well known, and here we take $\phi(x_i, y_i; h)$ to be the function of interest. This equation can be used to estimate the solution of the initial-value problem, $y' = f(x,y)$, subject to the condition, $y(x_o) = y_o$, and providing $a \leq x \leq b$.

Our goal is to estimate the error bound, thus we may define a local truncation error, τ_i, according to the following equation :

$$y(x_{i+1}) = y(x_i) + h\,\phi[x_i, y(x_i); h] + h\,\tau_i \qquad \text{A.2}$$

where $y(x)$ is a solution to the initial value problem.

The virtue of τ_i is that it tells us by how much y_{i+1} would miss $y(x_{i+1})$ if the computation were started at x_i with the exact answer, i.e. if $y_i = y(x_i)$.

In the case of Euler, we have from A.2 with $\phi(x,y;h) = f(x,y)$

$$y(x_{i+1}) = y(x_i) + h\,f(x_i, y(x_i)) + h\,\tau_i \qquad \text{A.3}$$

Using a Taylor expansion on A.3 we have to second order in h

$$y(x_{i+1}) = y(x_i) + h\, y'(x_i) + \frac{h^2}{2!} y''(\theta_i) \qquad A.4$$

where $x_i < \theta_i < x_{i+1}$. However, because $y'(x_i) = f[x_i, y(x_i)]$ we therefore find that for the Euler method the truncation error is expressed by the following equation :

$$\tau_i = \frac{h}{2} y''(\theta_i) \qquad A.5$$

for some θ_i within the range of $x_i \rightarrow x_{i+1}$. The absolute truncation error is therefore given by :

$$y_{i+1} - y(x_{i+1}) \qquad A.6$$

and is seen to consist of two parts :

a) the accumulated error that is made in passing from x_o to x_i and using y_i in place of $y(x_i)$ in eqn.A.1

b) the local truncation error, $h\tau_i$, that is made at x_i in going from y_i to y_{i+1} if y_i were numerically equal to $y(x_i)$.

On substituting A.1 and A.4 in A.6 we obtain for the absolute truncation error ε_i, the following formula

$$\varepsilon_{i+1} = y_i - y(x_i) + h[\phi(x_i,y_i;h) - \phi(x_i,y(x_i);h)] - h\tau_i$$

or

$$\varepsilon_{i+1} = \varepsilon_i + h[\phi(x_i,y_i;h) - \phi(x_i,y(x_i);h)] - h\tau_i \qquad A.7$$

Computationally we assume that ϕ satisfies a Lipshitz condition, viz. that there is a constant L, such that

$$|\phi(x,u;h) - \phi(x,v;h)| \leq L|u-v|$$

hence, the Lipshitz condition requires that

$$|\varepsilon_i| \leq \tau(e^{L(x_i-x_o)} - 1)/L$$

where τ is the local truncation error. Hence for the Euler algorithm we have :

$$|\varepsilon_i| \leq \frac{h\,M}{2\,L}(e^{L(x_i-x_o)} - 1) \qquad \text{A.8}$$

where $M = \max. |y''(x)|$.

In practice it is often found that the Lipshitz constant, L, is ≈ 1, and that $x_o = 0$; in this case the absolute truncation error is just

$$|\varepsilon_i| \leq \frac{h\,M}{2}(e^{x_i} - 1)$$

Rounding Errors

Errors such as these can often be partially overcome by using double precision arithmetic, and as such errors can often severely limit the accuracy that can be obtained. We will only be concerned here with their effects upon the Euler algorithm.

From the Euler method :

$$y_{i+1} = y_i + hf(x_i,y_i), \quad i = 0, 1, 2..., \qquad \text{A.9}$$

we see that there are two places in which rounding errors may occur, viz. in the evaluation of $f(x_i,y_i)$ and in the formation of $y_i + hf(x_i,y_i)$ and while double precision arithmetic helps in the latter case, it is difficult to avoid errors when evaluating $f(x_i,y_i)$.

In theory the Euler method calculates the left hand side of

eqn.A.9, although in practice the computer actually calculates the numbers

$$u_{i+1} = u_i + hf(x_i,u_i) + \delta_i \qquad A.10$$

where δ_i is the local rounding error, which occurs as the machine goes from u_i to u_{i+1}. Subtracting A.10 from A.9 produces :

$$y_{i+1} - u_{i+1} = y_i + hf(x_i,y_i) - u_i - hf(x_i,u_i) - \delta_i$$

Defining $\Delta_i = y_i - u_i$, which is just the difference between what the machine calculates and what Euler's method would produce if no errors were present, we obtain :

$$\Delta_{i+1} = \Delta_i + h[f(x_i,y_i) - f(x_i,u_i)] - \delta_i$$

However, recalling eqn.A.7, and again making use of $\varepsilon_i = y(x_i) - u_i$ we obtain

$$\varepsilon_{i+1} = \varepsilon_i + h[f\{x_i,y(x_i)\} - f(x_i,y_i)] - h\tau_i$$

Therefore the error between the true solution at x_i and the computer approximation u_i can be denoted by E_i, given by

$$E_i = \varepsilon_i + \Delta_i$$

hence using the expressions for ε_i and Δ_i gives :

$$E_{i+1} = E_i + h[f\{x_i,y(x_i)\} - f(x_i,u_i)] - h\tau_i - \delta_i$$

again assuming a Lipshitz condition for $f(x_i,y_i)$, i.e. $|f(x,v) - f(x,w)| \leq K|v - w|$ for all v, w where K is a constant. We find that for the absolute rounding error the Lipshitz condition requires

$$|E_{i+1}| \leq (h\tau - \delta)\left\{\frac{(1 + hK)^{i+1} - 1}{hK}\right\}$$

whereupon using the bound $(1 + hK)^{i+1} \leq e^{(i+1)hK}$ we obtain finally for the absolute rounding error :

$$|y(x_{i+1}) - u_{i+1}| \leq \frac{e^{K(e_{i+1} - x_o)} - 1}{K} (\tau - \frac{\delta}{h}) \qquad \text{A.11}$$

Again in practice K is often unity and $x_o = 0$ whereupon we have :

$$|y(x_{i+1}) - u_{i+1}| \leq e^{x_{i+1}} - 1 \ (\tau - \frac{\delta}{h}) \qquad \text{A.12}$$

It is convenient at this point to restate eqn.A.5 for the truncation error :

$$\tau_i = \frac{h}{2} y'' (\theta_i)$$

If this, and eqn.A.12 are considered together we find that the term $(\tau - \frac{\delta}{h})$ is the significant one, as for the truncation error we see that τ decreases as h decreases, but eqn.A.12 tells us that the term δ/h increases with decreasing h, also the smaller h becomes the greater the number of steps required to obtain solutions, therefore the greater the influence of rounding errors.

In conclusion, for most problems which are suitable for solution using one step algorithms such as the Euler method, there is clearly an optimum value of h for which the quantity $(\tau - \frac{\delta}{h})$ is a minimum, while this depends on the nature of the problem, it is often best to attempt an educated guess at what this optimum value might be.

References

La Fara, R.L., *Computer Methods for Science and Engineering*, Intertext Books Ltd., 1973.

Potter, D., *Computational Physics*, Wiley Interscience, 1977.

McCormick, J.M. and Salvadori, M.G., *Numerical Methods in Fortran*, Prentice-Hall Inc., 1964.

Whittaker, E.T. and Watson, G.N., *A Course of Modern Analysis*, (4th Edition), Cambridge University Press, London, 1969.